Technical Report

TR-10-21

Full perimeter intersection criteria

Definitions and implementations in SR-Site

Raymond Munier
Svensk Kärnbränslehantering AB

March 2010

Svensk Kärnbränslehantering AB
Swedish Nuclear Fuel
and Waste Management Co

Box 250, SE-101 24 Stockholm
Phone +46 8 459 84 00

ISSN 1404-0344
SKB TR-10-21
ID 1233496
Updated 2013-02

Full perimeter intersection criteria

Definitions and implementations in SR-Site

Raymond Munier
Svensk Kärnbränslehantering AB

March 2010

Update notice

The original report, dated March 2010, was found to contain both factual and editorial errors which have been corrected in this updated version. The corrected factual errors are presented below.

Updated 2013-02

Location	Original text	Corrected text
Page 7, paragraph 3, line 9	/Hedin and Andersson 2009/.	/SKB 2009c/.
Page 29, fifth bullet point from the end	/Hedin and Andersson 2009/.	/SKB 2009c/.
Page 87, reference “Hedin A, 2008”	...DOI 10: pp 008–9175.	…doi: 10.1007/s11004-008-9175-3.
Page 88, reference SKB 2009a	TR-08-05	TR-09-01
References	Hedin A, J Andersson, 2009. Design premises for a KBS-3V repository based on results from the safety assessment SR-Can and some subsequent analyses. TR-09-22, Svensk Kärnbränslehantering AB.	SKB 2009c. Design premises for a KBS-3V repository based on results from the safety assessment SR-Can and some subsequent analyses. TR-09-22, Svensk Kärnbränslehantering AB.

Contents

1 Preface

Large fractures intersecting canisters have potential to reactivate due to nearby earthquakes and thereby jeopardising the canister/buffer integrity. The use of full perimeter intersection (FPI) as a proxy for fracture size has been explored within SKB since late 2004. A methodology to use FPI as a deposition hole rejection criterion was first reported in /Munier 2006/ and the concept has successively matured ever since. As a response to feedback obtained from various instances of our organisation and external reviewers, additional analyses and benchmarks were reported in /Munier 2007/. An analytical solution to the canister/fracture intersection probability was introduced by /Hedin 2008/ which enabled us to benchmark various aspects of the FPI simulations.

The methodology was first applied within the framework of SR-CAN /SKB 2006/ to compute the number of potentially critical canister positions and soon after, based on preliminary DFN models /Fox et al. 2007/, as one of many prerequisites for repository design.

The methodology and simulation logic has evolved substantially ever since it was originally reported in /Munier 2006/ and the present report is intended to entirely replace previous reports on this subject, to thereby provide the interested reader with an description of the modelling procedure, pre-requisites and limitations. As a consequence thereof, major portions of previous reports are repeated herein, though we occasionally refer to these reports for comparative purposes. Furthermore, as the final versions of the site descriptive models have been reported /e.g. SKB 2008, SKB 2009a/ we find it convenient to, within this report, also apply the methodology using the most actual site specific fracture data /Fox et al. 2007, La Pointe et al. 2008/.

This report is organised as follows:

In Chapter 2, we introduce the reader to the issue and present the main argumentation for the full perimeter intersection criteria. In Chapter 3 we define terms and key parameters specific to this work. The simulation procedure is presented in Chapter 4 which covers generation of fractures, tunnel geometries and collision tests. This fairly technical chapter can be passed over by readers familiar with the work presented in /Munier 2006/. Benchmarking of the codes is presented in Chapter 5 which also includes tests originally presented in /Munier 2007/ and may be passed over by readers less interested in the simulation aspect of this work. The effect of tuning the criteria using various options and/or assumptions is explored in Chapter 6. It provides input to the discussion (Chapter 8). The methodology is applied to the Forsmark and Laxemar sites in Chapter 7 which ought to provide input to the safety assessment SR-SITE and to the site selection. In Chapter 8 we discuss the conservatism of the method and its consequences on safety assessment and repository layout. The work is briefly concluded in Chapter 9.

2 Introduction

The integrity of the canister/buffer system can be jeopardised by large earthquakes that occur in the vicinity of the repository. To avoid mechanical damage due to earthquakes, SKB has adopted the notion of "*respect distance*" which, according to /Munier and Hökmark 2004/ is defined as follows:

"The respect distance is the perpendicular distance from a deformation zone that defines the volume within which deposition of canisters is prohibited, due to anticipated seismic effects on canister integrity".

The notion of respect distance reflects the basic idea that the damaging effect of earthquakes in solid rock decreases with distance as the seismic energy attenuates. However, the use of respect distances alone cannot guarantee the integrity of the canisters. If the canister position is intersected by a large fracture, the earthquake can trigger the fracture to reactivate in such a way that the canister is damaged. Thus, there is a relation between the respect distance and the size and geometry of fractures that can be allowed to intersect the deposition holes /Fälth et al. 2010/. If a fracture is too large it might, when triggered by a nearby earthquake, host a slip exceeding the canister failure criterion, originally set to 10 cm /Börgesson et al. 2003/ but later reduced to 5 cm with the most current canister design /SKB 2009c/. Empirical and numerical studies reported in /Munier and Hökmark 2004/ indicated that a fracture must have a radius exceeding 50 m to be able to host a maximum slip of 10 cm, using a respect distance of 100 m to the boundary of the deformation zone. The numerical methods developed to include fracture friction in /Fälth and Hökmark 2006/ who concluded that the size of acceptable fractures intersecting deposition holes can be increased to r = 75 m (100 m respect distance) and r = 150 m (200 m respect distance) respectively. Additional efforts by /Fälth and Hökmark 2006, Fälth et al. 2007, 2008/ have shown, by analogy to large, instrumented earthquakes /e.g. Ma et al. 2003/, that previous models were highly conservative; earthquakes previously modelled as having magnitude ≥ 6 were suggested to be more representative of magnitude 7–7.5 events. As a consequence thereof, and of additional analyses, the relation between critical fracture sizes, distances to deformation zones and the geometries of the deformation zones have been updated in /Fälth et al. 2010/.

However, regardless of which fracture size one should consider discriminating, the main issue remains; the size of a fracture can rarely, if ever, be measured. It is therefore essential to make use of various proxies for fracture size. Additionally, some fractures are essentially blind to present-day instruments. Unfortunately, as shown by /Cosgrove et al. 2006/, there is no single parameter or property that can be used to uniquely identify a fracture as being large. Rather, an array of parameters is needed, and there will still be a small, but un-quantified, number of large fractures that will escape detection. SKB is currently (2009–2010) outlining the methodology for underground mapping. Meanwhile, we need a robust and simple method to identify potentially discriminating fractures (i.e. fractures large enough to permit movement in excess of the 5 cm to occur) for the estimation of the degree-of-utilisation of the repository and estimation of the number of remaining critical deposition holes.

A simple indicator for a fracture being large is if its intersection with a tunnel can be traced around the full perimeter of the tunnel face (Figure 2-1). Such fracture intersections are easy to observe and require no additional efforts than traditional fracture mapping in tunnels. FPI mapped at the Onkalo and Äspö tunnels, shown on Figure 2-2, amount to about 13/100 m and 17/100 m on average, at Onkalo /Nordbäck et al. 2008/ and Äspö respectively, which indicates the expected amount of FPIs at the SKB repositories.

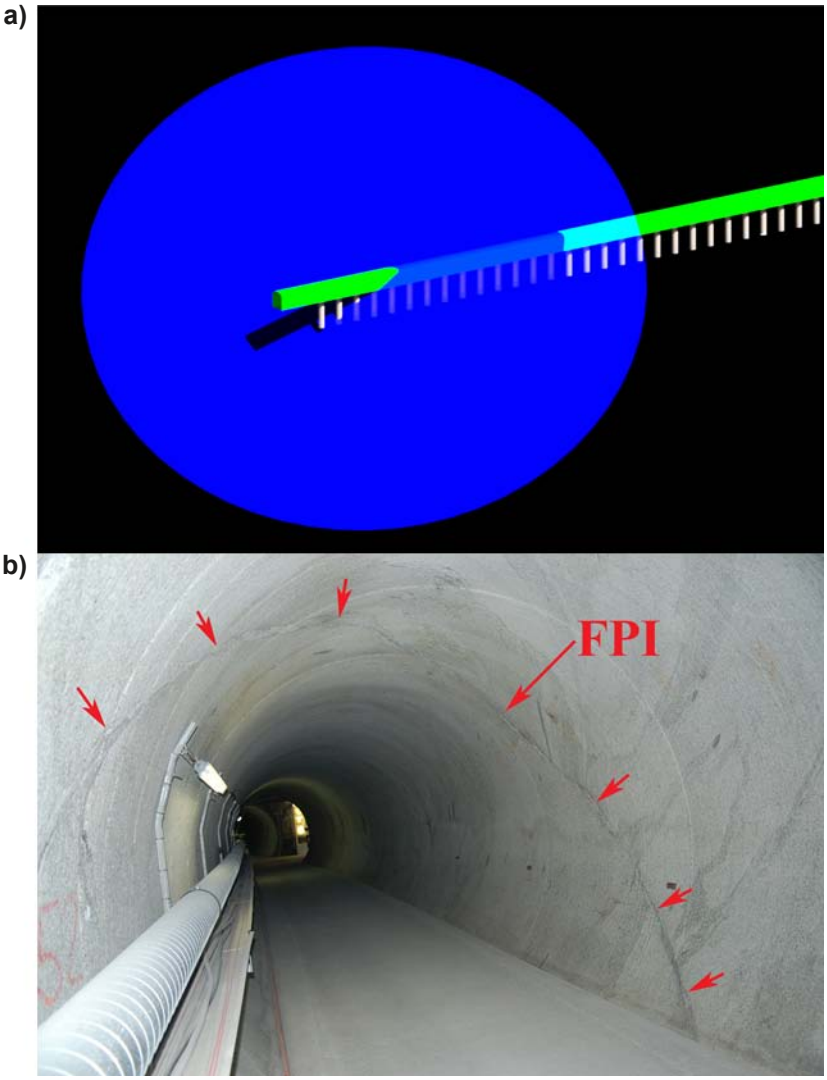

Figure 2-1. *Schematic cartoon illustrating the concept of FPI (a) and an example of a full perimeter intersection, Grimsel test site, Switzerland (b).*

This report has two goals:

1. To compute the number of critical deposition holes.
2. To compute the degree-of-utilisation.

This is achieved by means of stochastic fracture simulation consisting of three steps: The first consists of computing intersection statistics between the tunnel and the fracture network. The second step consists of locating deposition holes according to discrimination criteria followed by a computation of the degree-of-utilisation. The last step consists of computing the number of deposition holes that escaped all criteria.

We base our simulations upon the DFN models produced for the Laxemar[1] /La Pointe et al. 2008/ and Forsmark[2] /Fox et al. 2007/ study sites.

[1] /Modelldatabasen 2008/. Model: DFN LAX v2.3 (site).xls. Version 0.5. Approved 2008-08-19, Modeller: A. Fox. Simon ID: GEO_HXXZNQSH. https://service.projectplace.com/pp/pp.cgi/r241528007 (access might be given on request).

[2] /Modelldatabasen 2007/. Model: PFM DFN 2.2.xls. Version 0.6. Approved 2007-11-29, Modeller: A. Fox. Simon ID: GEO_WTAGLLAA. https://service.projectplace.com/pp/pp.cgi/r232241793 (access might be given on request).

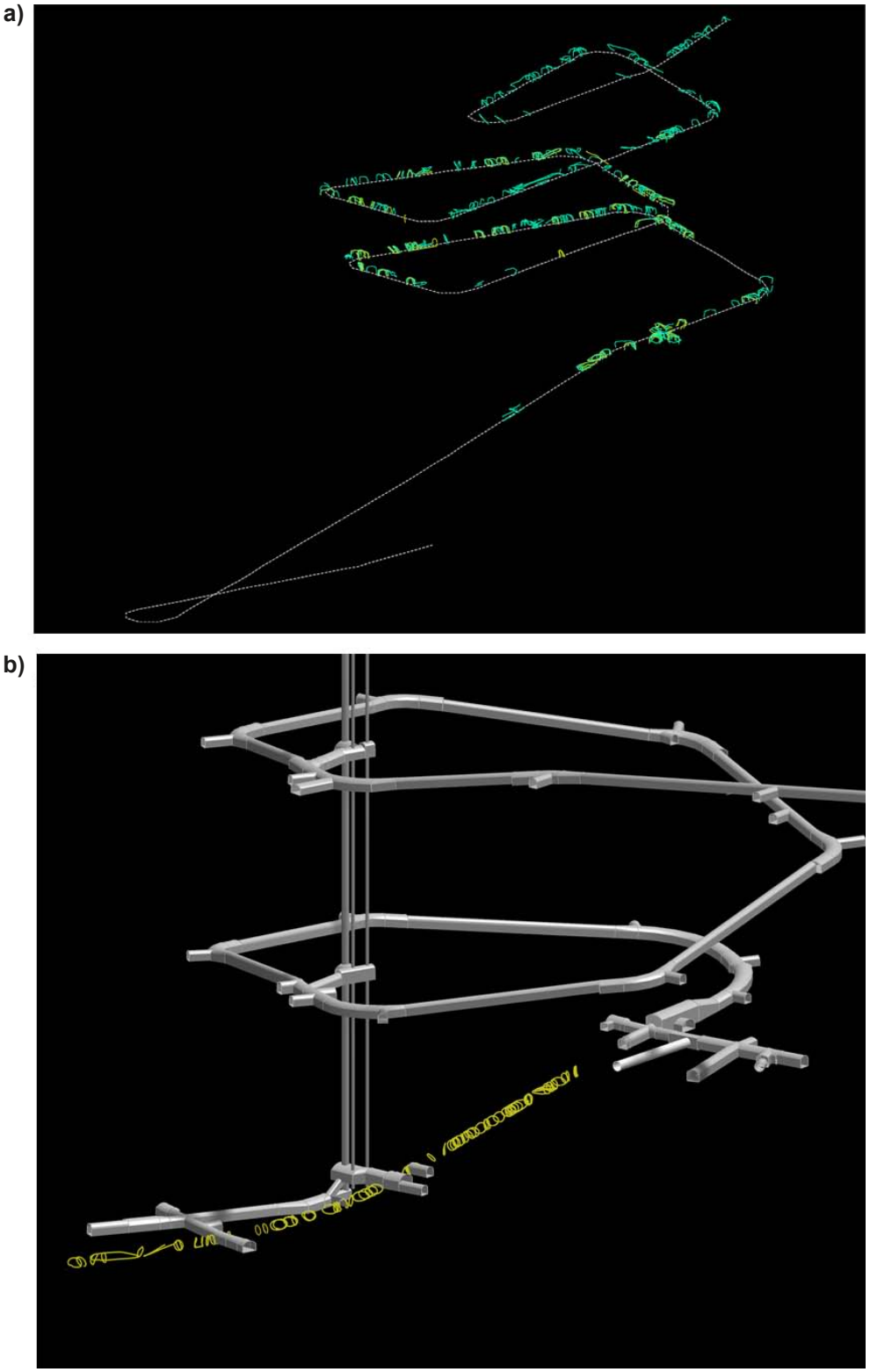

Figure 2-2. *Full perimeter intersections mapped at Onkalo (a) and Äspö (b).*

3 Definitions

3.1 Critical canister position

The shear induced on fractures, as a consequence of nearby earthquakes, is a combined effect of the earthquake magnitude, the distance to the earthquake generating fault and the size of the target fracture as argued in /Fälth et al. 2010/ (see also Table 7-2).

A canister position that is intersected by a fracture able to host a slip exceeding the canister failure criterion, is here defined as being a "critical position". The fracture, consequently, is denoted "critical fracture". Should the position be detected by the FPI rejection criteria (see Section 3.2 to 3.3 below), the intersecting fracture may instead be denoted "discriminating fracture" if appropriate. Critical positions that remain undetected despite application of FPI rejection criteria are simply denoted "remaining critical positions".

3.2 Definition of FPC

The main objective of this work is to present an easily identifiable characteristic of fractures, the Full Perimeter Intersection (FPI), to identify traces of large fractures in a *tunnel*. The ultimate goal is, however, to use FPIs to identify *deposition holes* intersected by fractures large enough to constitute a (seismic) hazard and adjust the deposition hole location to avoid intersection.

We choose to do so by introducing the full perimeter criterion, FPC. Applying the FPC means that the (infinite) extrapolation of the FPI-generating fracture (Figure 3-1) is used to represent a fracture of unknown size. Any deposition hole intersected by such extrapolation will be considered for rejection regardless of the true fracture size. In /Munier 2006/, a position was regarded potentially critical if the extrapolation of the FPI fracture intersected any part of the planned deposition hole (Figure 3-1a). This criterion has since been judged overly conservative and therefore slightly modified to the following: A position is regarded as potentially critical if the extrapolation of the FPI fracture intersects any portion of planned canister position (Figure 3-1b). The difference in the resulting degree-of-utilisation for these two criteria is evaluated in Section 6.1.

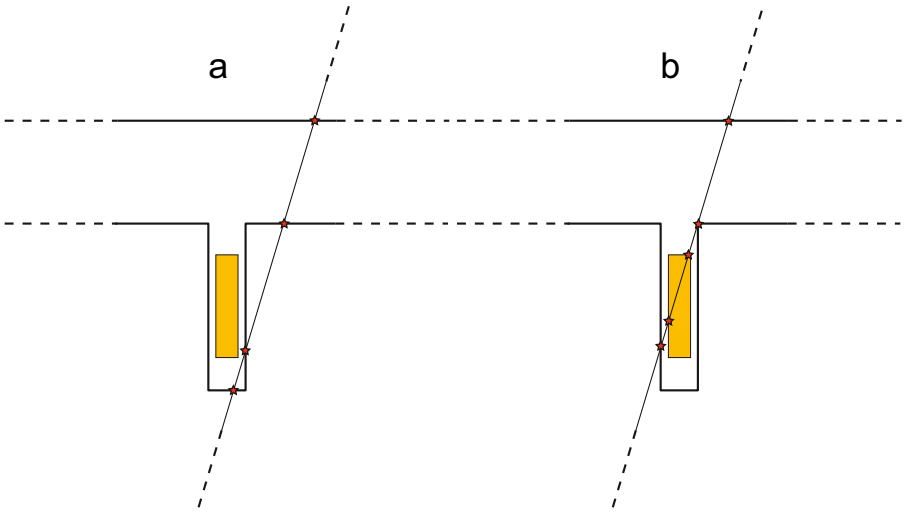

Figure 3-1. *In "a" we display the criterion as previously applied in /Munier 2006/. In "b" we display the modified FPC criterion: The FPI mapped in the tunnel is judged to represent the trace of a discriminating fracture if its projection intersects the planned canister position (b).*

3.3 Definition of EFPC

There is a complication, though, in that the FPC fails to detect all discriminating fractures. For instance, it is likely that large fractures that do not intersect the deposition tunnel but are sufficiently close, have the potential to intersect a relatively large number of canisters (Figure 3-2). Typically, such fractures have strikes parallel to the tunnel trend, mostly belonging to the sub-horizontal set of any fracture network.

By analogy with the rationale for using the FPC, the size of these fractures will be unknown and we would need a similar criterion.

One criterion that could be used is the number of deposition holes across which the fracture can be traced. Figure 3-3 shows a plan view of a deposition tunnel, and a sub-horizontal fracture of size (radius) "r" cutting through n' deposition holes (note that "r" can be much larger still producing the same number of deposition hole intersections). The radius of a fracture that encircles exactly n' deposition holes is denoted "r'". If we denote the standard distance between canisters as "D" then:

$$r' = \frac{1}{2} D\left(n' - 1\right) \qquad \text{Eq. (1)}$$

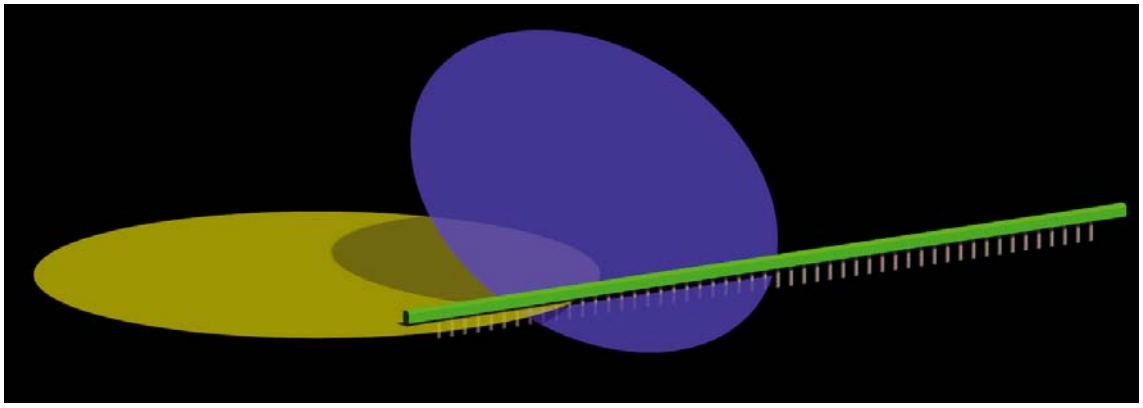

Figure 3-2. *Potentially discriminating fractures can remain undetected despite the use of the full perimeter criterion in the deposition tunnel. An additional criterion, EFPC, was therefore defined.*

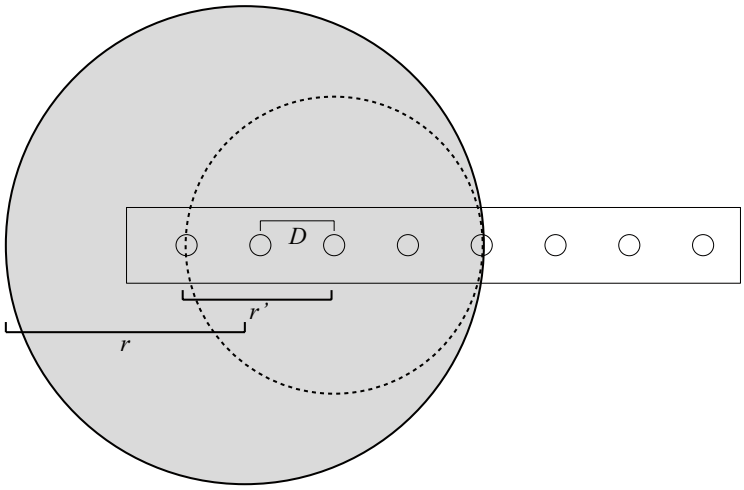

Figure 3-3. *Extended full perimeter criterion, EFPC.*

This means that if we arbitrarily set n' to 5, the EFPC criterion will, theoretically, detect fractures with radii exceeding 12 m (using a 6 m canister spacing), which appears conservative as it is much smaller that the critical radius (Section 6.3 and Table 7-2).

Nevertheless, a few fractures will escape detection despite this criterion. It is, for instance, possible for a discriminating fracture to intersect fewer than n' deposition holes if it is located near the edge of the tunnel (e.g. Figure 3-4). It is also possible, though less likely, that deposition holes are intersected close to the fracture tip. Both these effects can be taken into account by using a stricter criterion, e.g. using two intersections or more (rather than 5 or more as was arbitrarily set by /Munier 2006/) as the criterion, at the expense of the degree-of-utilisation (see Section 6.1). The expanded FPC will hereafter be referred to as "EFPC" and, if not stated differently, the degree-of-utilisation will be computed using both FPC and EFPC.

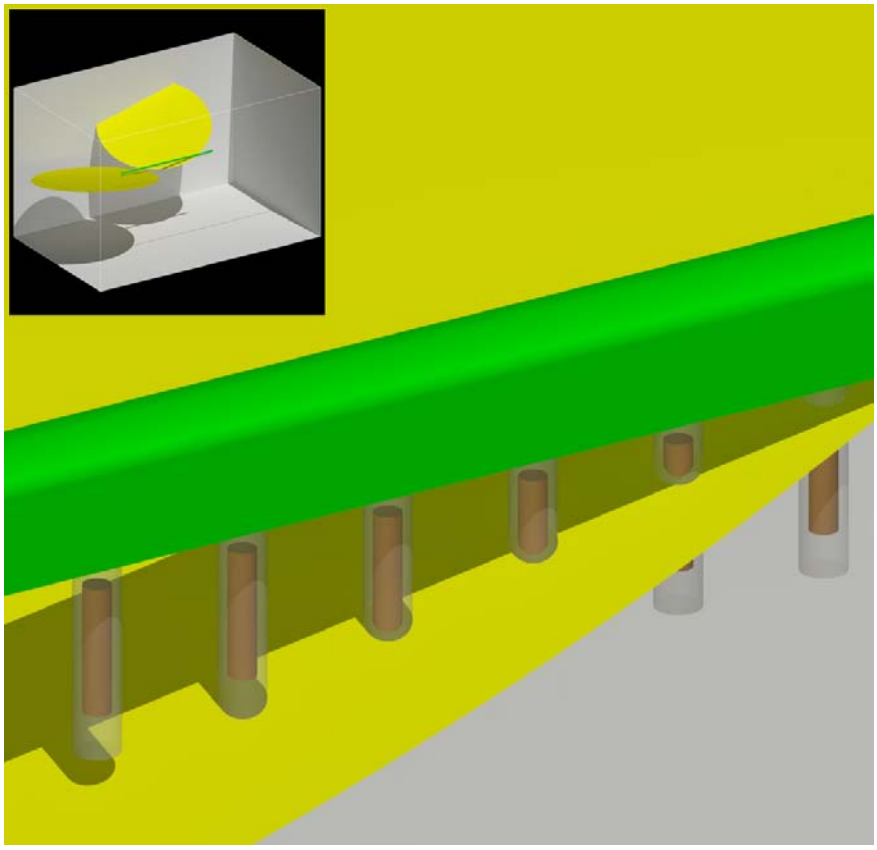

Figure 3-4. *The figure illustrates a case for which the expanded FPC (EFPC) fails to detect discriminating fractures.*

3.4 Efficiency of the criteria

To evaluate the efficiency of the proposed criteria in finding discriminating fractures, we make use of the method proposed by /Hedin 2008/ which, in short, is a semi-analytical method to compute the probability of intersection between a cylinder (deposition hole, TBM-tunnel or canister) and a circular disk (representation of a fracture) using DFN models. The measure "epsilon" (ε) is the probability of a canister being intersected by a fracture exceeding a certain size using blind deposition, i.e. not applying any rejection criteria whatsoever. This enables us to compute the number of canisters in a repository that are, theoretically, anticipated to be intersected by discriminating fractures with critical sizes according to /Fälth et al. 2010/ and to compare this number with the number of canisters remaining after having applied the FPI criteria. We define the efficiency, E, as:

$$E = \frac{\varepsilon N - n}{\varepsilon N} \qquad \text{Eq. (2)}$$

were n is the number of intersected deposition holes that escaped the FPI criteria (obtained by simulation) and N the total number of deposition holes in the model (6,000 in the base case).

The method of /Hedin 2008/ was, additionally, with minor modifications used to construct a number of semi-analytical benchmarks of the codes presented herein (see Chapter 4).

3.5 Degree-of-utilisation

We define a "degree-of-utilisation", to express the efficiency of the rock in hosting canisters should the FPI criteria be utilised. This entity, expressed in %, is defined as follows:

$$DoU = 100 \cdot \frac{\text{Number of accepted positions}}{\text{Planned number of positions}} \ \% \qquad \text{Eq. (3)}$$

As the number of canisters to emplace is fixed, any degree-of-utilisation less than 100% must be compensated for by increasing the length of the deposition tunnel or adding more tunnels. In other words, the degree-of-utilisation is a measure of the required space for the repository.

4 Simulation procedure

4.1 Computation of intersections

In this study, we idealise a fracture as an infinitely thin, circular disc. The problem studied here, is thus essentially one of finding the intersection between a finite plane and a finite cylinder representing the deposition hole, canister or, in some special benchmark cases, the deposition tunnel. This section is essentially a repetition of the description in /Munier 2006/ and might be skipped by readers familiar to previous work.

There are many possible intersection geometries (Figure 4-1), all of which are discussed briefly below:

Intersection “b” is by far the most common and occurs when the plane intersects the cylinder at an oblique angle. Intersections “a” and “c” constitute special cases of “b” and occur when the plane is perpendicular or parallel to the cylinder respectively.

Intersection “d” requires the plane to be oriented exactly parallel to the tunnel, and located exactly at its tangent, which is unlikely both in simulations and in a real tunnel system. The FPI criterion requires the fracture to be detectable by the naked eye and thus “d” type intersection will therefore not be included in the analyses. Intersections “f” and “g” are special cases of “d”.

Intersection “e” occurs if the fracture intersects the end-cap of the tunnel.

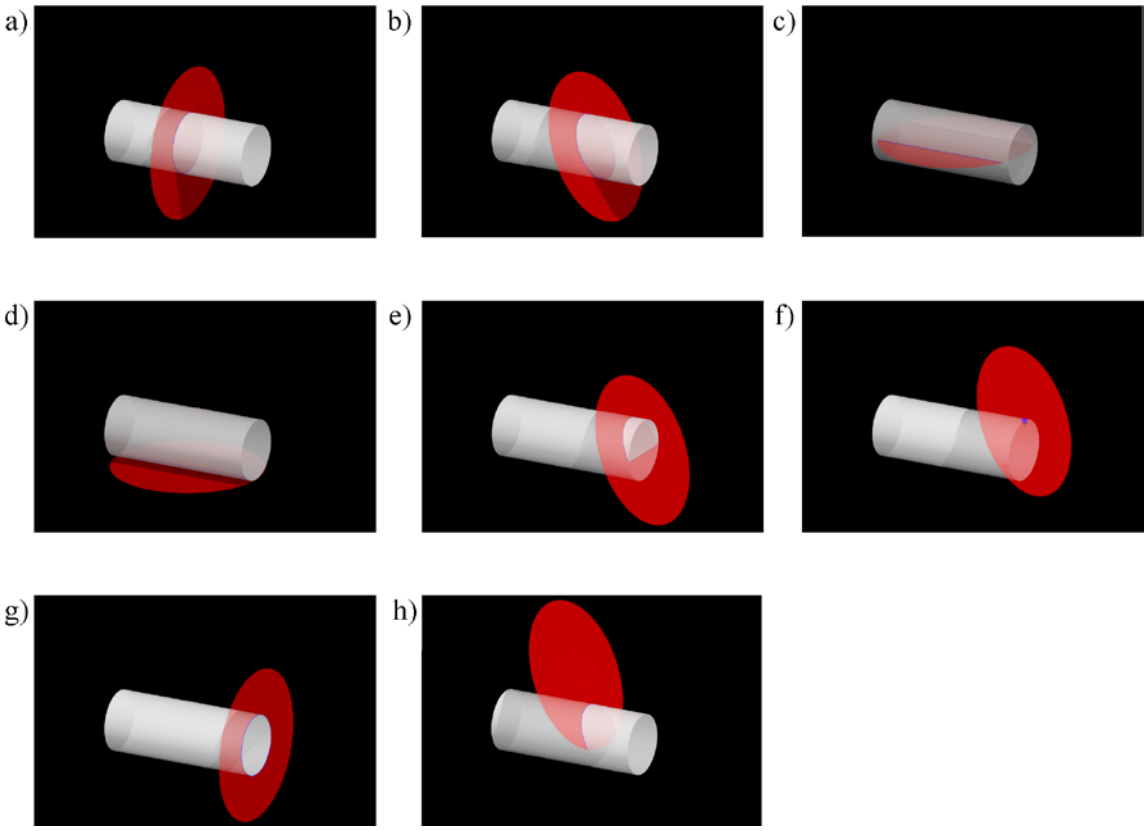

Figure 4-1. *Possible intersection geometries between a plane and a finite cylinder. Cases “c” and “h” can only occur for finite discs (assumed for EFPC) whereas the remaining cases can also occur for infinite planes (assumed for FPC).*

In addition to the intersections above, we can envisage intersections as parts of ellipses (intersection "h"), which would occur if the planes were not large enough to cut through the entire tunnel diameter or located such that only the tip of the plane intersects. Thus, for the purpose of evaluating a FPI criterion, only intersections of type "a", "b", "c" and "e" are considered.

We define a plane P (Figure 4-2) in terms of its centre point, P_c, its unit vector, $\hat{n}$ and its radius r_p. A cylinder is defined in terms of its centre point C, its axis orientation, represented by the unit vector $\hat{c}$, its radius r_c and its half-length (or half-height) h.

If the plane is perpendicular to the cylinder, then the absolute value of the dot product equals one, i.e.:

$$\left|\hat{c}\cdot\hat{n}\right| = 1 \qquad \text{Eq. (4)}$$

and we will, for an *infinite* plane, have an intersection if the distance between P and C is less than or equal to h, producing an intersection of type "a" or "g" respectively.

If the plane is parallel to the cylinder, the dot product is zero, i.e.:

$$\hat{c}\cdot\hat{n} = 0 \qquad \text{Eq. (5)}$$

and we will have an intersection if the distance between P and C is less than or equal to r_c producing type "c" or type "d" intersections, respectively.

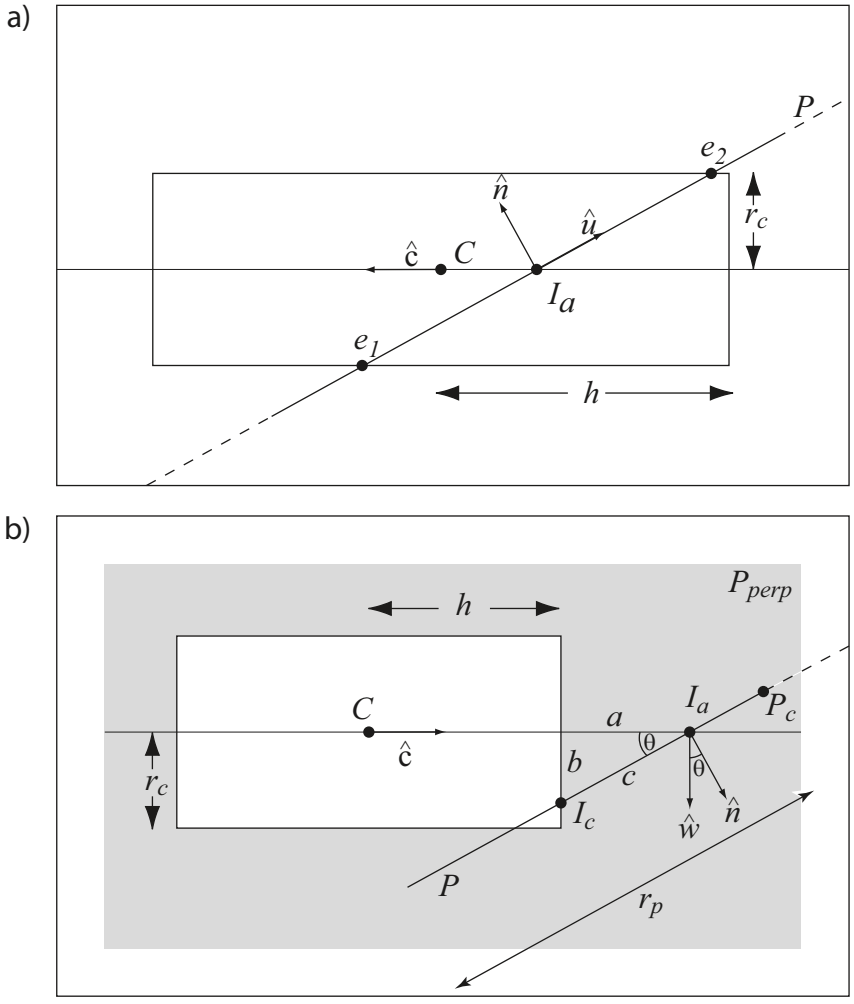

Figure 4-2. *a) Criteria for elliptical intersections. b) Criteria for end-cap intersections /redrawn from Schneider and Eberly 2003/.*

If the plane is neither parallel nor perpendicular to the cylinder we have an intersection if the intersection point, I_a, between the plane and the cylinder axis is closer to C than the half length, h, which produces an intersection of type *"b"* or *"e" (or "h")*. However, the plane might intersect the axis beyond the end caps and there might be an intersection depending on the relative location and orientation of the objects. The intersection, if it does occur, will be of the types *"e"* or *"f"*.

To check for an intersections of type "*b*" we compute the intersection between the plane, the cylinder axis and the cylinder which produces an intersection point I_a and an ellipse (Figure 4-2a). Using the major axis of the ellipse, parallel to $\hat{u}$, we check if the ellipse, represented by the points e_1 and e_2, lie entirely within the end caps of the tunnel. If so, we have an intersection of type "b". If not, we may have an intersection of type "f" or "e". The latter, end-cap intersection, is computed as follows:

Following the reasoning in /Schneider and Eberly 2003, Section 11.7.3, pages 553–555/, for the case I_a lies beyond the end-caps (Figure 4-2b), we define a vector $\hat{w}$ such that:

$\hat{w} = \hat{c}\times(\hat{n}\times\hat{c})$, is a vector perpendicular to $\hat{c}$ that lies in the plane, P_{perp}, containing both $\hat{n}$ and $\hat{c}$ (see Figure 4-2b). That is, we can always compute intersections in a coordinate system perpendicular to the fracture plane because of the rotational symmetry of the cylinder.

The angle θ between $\hat{n}$ and $\hat{w}$ is:

$$\cos(\theta) = \hat{n} \cdot \hat{w} \qquad \text{Eq. (6)}$$

The distance a is known:

$$a = \| I_a - C \| - h \qquad \text{Eq. (7)}$$

and by definition we know that:

$$\cos(\theta) = \frac{a}{c} \qquad \text{Eq. (8)}$$

Substituting, we get:

$$\hat{n} \cdot \hat{w} = \frac{\left\| I_a - C \right\| - h}{c} \qquad \text{Eq. (9)}$$

and so

$$c = \frac{\left\| I_a - C \right\| - h}{\hat{n} \cdot \hat{w}} \qquad \text{Eq. (10)}$$

Since $a^2 + b^2 = c^2$, then

$$b^2 = \left(\frac{\left\| I_a - C \right\| - h}{\hat{n} \cdot \hat{w}} \right)^2 - \left(\left\| I_a - C \right\| - h \right)^2 \qquad \text{Eq. (11)}$$

If $b^2 \le r_c^2$ and $\| P_c - I_c \| \le r_p$ we have an intersection of type *"e"* (or *"f"*); otherwise, no intersection occurs.

The advantage of the procedure outlined above is that the collision test is very fast. However, as discovered by /Stigsson 2008/ the collision test described in /Munier 2006, Section 2.2, test "e"/, would, under certain circumstances, erroneously mark fractures as FPI, thereby overestimating their number. The procedure outlined in /Stigsson 2008/ results in a quartic equation for which a robust Matlab solution, able to handle complex numbers, was provided in /Ayjara 2007/. As the solving of quartic equations is slow compared to the solution of /Schneider and Eberly 2003/, we have chosen to run the collision test using the Stigsson method only on fractures marked FPI, to identify the few that were erroneously marked by the Schneider and Eberly procedure outlined above, in order to save computation time.

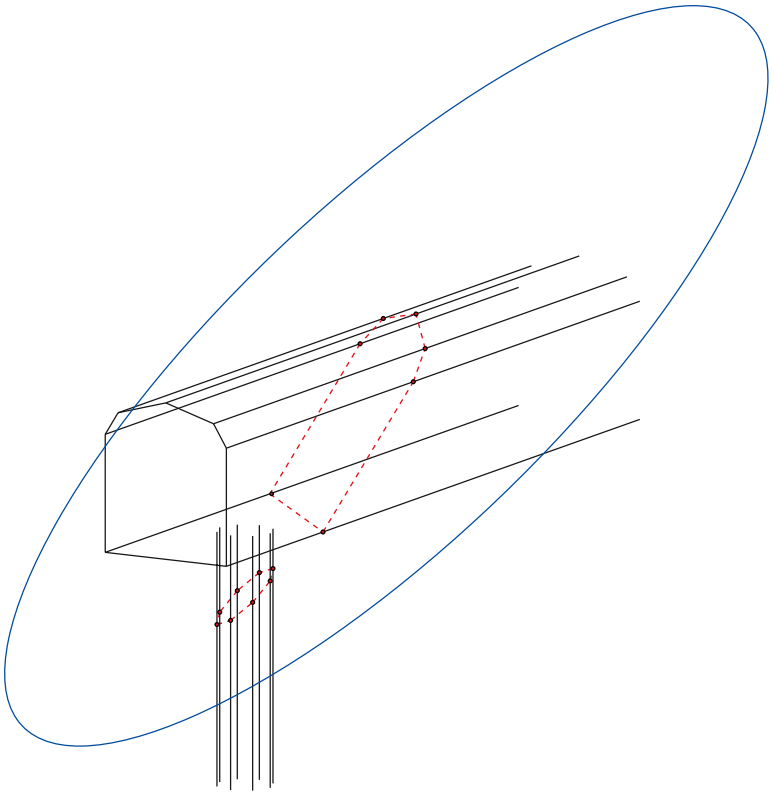

Figure 4-3. *Tunnel and deposition hole and canister geometries are simplified to line strings in most analyses of this study, thereby simplifying the collision tests to line/plane intersections.*

Additionally, as discussed in Section 5.4.8 the introduction of drill and blast shaped tunnels (and polygon shaped deposition holes) into the simulation have made the exact cylinder/plane collision test obsolete for most but a few important benchmark cases. In essence, therefore, most collision tests are simplified to address the intersection between a line and a disk, for which the solution is fairly trivial: The algorithm is simply to intersect the line with the plane in which the disk resides and to compute the distance between the intersection point and the disk centroids. The type of intersection (a–h, Figure 4-1) is obtained by counting the number of intersection points. Though this solution is less exact than the methods described above, it is very much faster and therefore favoured in this study.

4.2 Simulation of fracture network

The fractures in the DFN models are assumed to possess a Poissonian spatial arrangement (i.e. non-correlated positions), and a lack of correlation between size, position and orientation within each defined fracture set. Simulation of a fracture population therefore constitutes no further complication than random sampling from the given distributions for each fracture set and joining all sets into a fracture population.

We made use of the inversion method /e.g. Devroye 1986/ to produce random numbers either using built-in routines in Matlab (applies to rectangular, exponential and lognormal distributions) or by the expressions below. We hereafter denote a sample [0, 1] from a uniform distribution as U.

4.2.1 Fracture sizes

The site investigations have reported powerlaw distributions of fracture radii as main alternatives /Fox et al. 2007, La Pointe et al. 2008/. Though we implemented algorithms for other distributions (exponential, lognormal) we here only describe the simulation of the powerlaw.

We express the probability density function of a powerlaw distribution as /Evans et al. 2000, Munier 2004/:

$$f(r) = \frac{k_r \cdot r_{\min}^{k_r}}{r^{k_r+1}}, \quad r_{\min} \le x < \infty \qquad \text{Eq. (12)}$$

where $r_{\min}$ is the location parameter (smallest value of *r)*, and k_r the shape parameter.

Applying the inversion method, we obtain random numbers from a power-law distribution, r_{PL}, from:

$$r_{PL} = r_{min}\left[U\left(\left(\frac{r_{min}}{r_{max}}\right)^{k_r} - 1\right) + 1\right]^{-1/k_r} \qquad \text{Eq. (13)}$$

4.2.2 Fracture orientations

Random numbers from the univariate Fisher distribution can be obtained by three separate steps. We first sample the angular deviation from the mean poles, θ, using:

$$\theta = \arccos\left[\frac{1}{\kappa}\ln\left(e^{\kappa} - U\left(e^{\kappa} - e^{-\kappa}\right)\right)\right] \qquad \text{Eq. (14)}$$

were κ is the measure of concentration. The angles obtained can be regarded as the deviations from a vertical plunge (horizontal plane), i.e.

$$plunge = \frac{\pi}{2} - \theta$$

As the trend for a vertical plunge is uniform in [0, 2π], we obtain the trend from:

$$trend = 2\pi U$$

The set of vertical fracture normals produced is then rotated to the mean direction of the fracture set by first tilting the array to the mean plunge (i.e. rotation about a horizontal axis) and then adding the mean trend (i.e. rotation about a vertical axis).

4.2.3 Fracture intensity

In this report, we make use of the notation[3] by /Dershowitz 1985/.The number of fractures *N* to be simulated is governed by the fracture intensity, P_{32}, provided by the DFN model. The intensity is defined as the fracture area per unit volume, and is expressed in the unit m^2/m^3.

Following the reasoning in /Hedin 2005/, the number of fractures per unit volume, P_{30}, can be obtained from the relation:

$$P_{30} = n_0 f(\mathrm{r}) \qquad \text{Eq. (15)}$$

where *f(r)* is the probability density distribution of fracture sizes for a particular fracture set. Unlike /Hedin 2005/, we use a *finite* model volume which tends to underestimate P_{32} because some portion of the simulated fracture will lie outside the finite model volume. This effect becomes smaller the larger the model volume. The factor n_0 is obtained from P_{32} through:

$$P_{32} = n_0 \pi \int_0^{\infty} r^2 f(r)\, dr \qquad \text{Eq. (16)}$$

[3] The intensity, *P*, is expressed with subscripts to indicate dimensionality. For instance, P_{10} denotes the number of fractures (0D) per unit length (1D) whereas P_{21} denotes the trace length (1D) per unit area (2D). P_{32} denotes the fracture area (2D) per unit volume (3D). Other constructs are possible, for instance P_{30} which denotes the number of fractures (0D) per unit volume (3D).

Since we only simulate a portion of the population, *f(r)* in equation (15) must be integrated over the range [r_{min}, r_{max}]. The number of fractures needed to simulate for each fracture set in a model volume, V, is then obtained by combining equation (15) and equation (16) into:

$$N = V \frac{P_{32}}{\pi \int_0^{\infty} r^2 f(r)\, dr} \int_{r_{\min}}^{r_{\max}} f(r)\, dr \qquad \text{Eq. (17)}$$

To ensure homogeneous P_{32} throughout the model volume, in particular in the vicinity of the model boundaries, we implemented, as a simulation option, the fracture positions by sampling points randomly on the fracture surfaces (Figure 4-4), constraining the points to lie within the model volume. The procedure is described below.

A random point, P_r, is chosen from within the model volume as:

$P_{rx} = Udx$, $P_{ry} = U_{dy}$, $P_{rz} = Udz$

where dx, dy and dz are the dimensions of the model volume in each principal direction respectively, and U is, again, a uniform random number in [0, 1]. The unit vectors parallel to the strike and dip directions, $\hat{s}$ and $\hat{d}$, respectively, are known. We rotate $\hat{s}$ randomly about P_r in the plane containing $\hat{s}$ and $\hat{d}$ using an angle:

$\omega = 2\pi U$

The distance between P_r and P_c, $\| P_r - P_c \|$, is obtained from:

$\| P_r - P_c \| = rU$

By trigonometry the centroid, P_c, can be obtained from:

$P_c = P_r + \| P_r - P_c \| (\hat{s} \cos \omega + \hat{d} \sin \omega)$

This implementation of fracture centroids had very little effect on the simulation results. As it imposes an additional computational burden upon the simulation, we choose not to implement this option except on a few benchmark cases, and most analyses were instead based on a fixed simulation volume as described in Section 4.3.

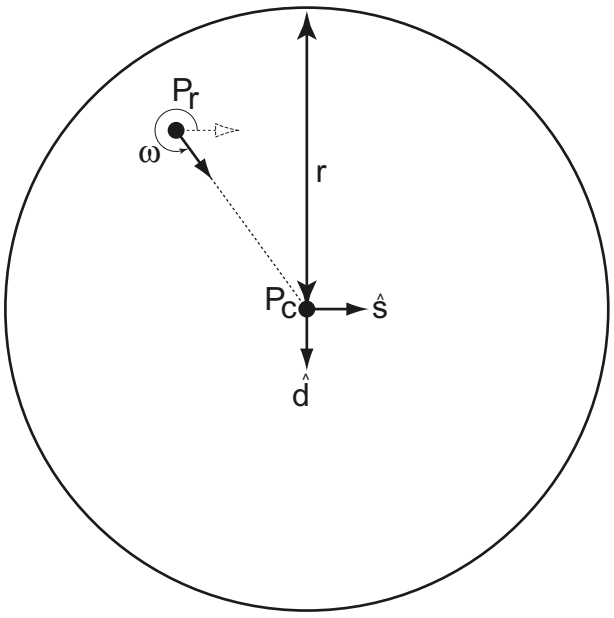

Figure 4-4. *Illustration showing the principle of deducing the fracture centroid from a randomly chosen point on the fracture surface.*

4.3 Simulation volume

Simulation of fractures honouring a specific intensity, P_{32}, requires the computation of fracture truncations against the boundaries of the model volume. This produces fractures of different shapes, each of which requires special handling, and is computationally expensive. To speed up simulations our procedures use P_{30}, the number of fractures per unit volume, to obtain required fracture intensity according to the input DFN model.

We do so by using equation (17) to transform P_{32} into P_{30}. This enables us to maintain the circular shape of the fractures and spares the codes from the burden of boundary intersection computations. The equations are, however, only valid for infinite volumes. There will always be a part of the fractures outside the finite model volume which do not contribute to P_{32}.

As the model volume increases, the fracture area outside the model volume will be increasingly smaller compared to the fracture area within the model volume. For a sufficiently large model volume, the difference can be regarded as negligible.

We defined a simulation base case (see Section 5.1) from which various variants are defined depending on the purpose of the simulation. To ensure maximum flexibility of the codes, we implemented most prerequisites such as tunnel length, orientation, cross-sectional area, etc as variables.

As only fractures of radii up to a certain value, $r_{max,}$ are of interest to this study, the simple and absolute upper bound on the required model volume is:

$dz = dy = 2(r_{max} + r_{Tunnel})$, and

$dx = 2r_{max} + L_{Tunnel}$

where r_{Tunnel} and L_{Tunnel} are the tunnel radius and tunnel length respectively. Thus, using a tunnel length of 300 m, the model volume is approximately 800×500×500 m. An example simulation volume is displayed in Figure 4-5.

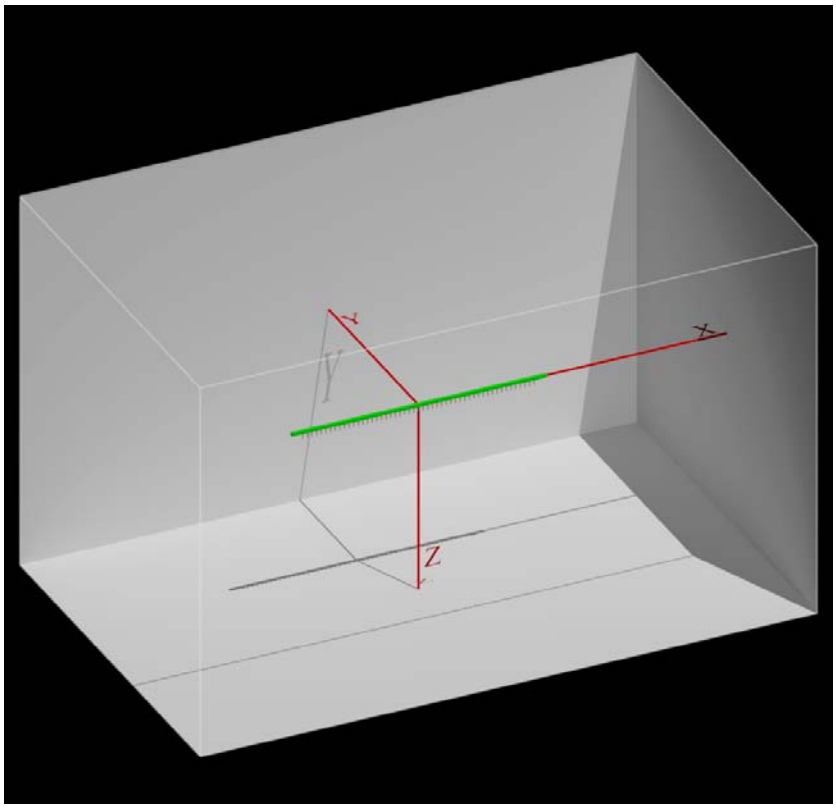

Figure 4-5. *Simulation volume, tunnels and coordinate system.*

4.4 Geometries

4.4.1 Tunnel geometry

The tunnel cross-section planned for the repository is displayed in Figure 4-6 /from SKB 2009b/. The cross-sectional profile was simplified to allow for line string representation (see Section 4.1 and Figure 4-3) which rendered a slightly smaller cross-sectional area shown as the red outline in Figure 4-6. As will be demonstrated later, this has no practical effect on the simulation results.

Some of the benchmarks require a circular cross-sectional profile. There are two cases to consider:

- A circle having the same area as the drill and blast profile (Figure 4-7a).
- A circle circumscribing the drill and blast profile (Figure 4-7b).

These will yield slightly different areas and therefore, slightly different simulation results.

The tunnels are, in all simulations and benchmarks, aligned in E-W direction (X-axis of the model coordinate system, Figure 4-5) and centred at the model origin. To implement tunnels of other orientations, we rotate the fracture network, rather than the tunnels, for computation efficiency.

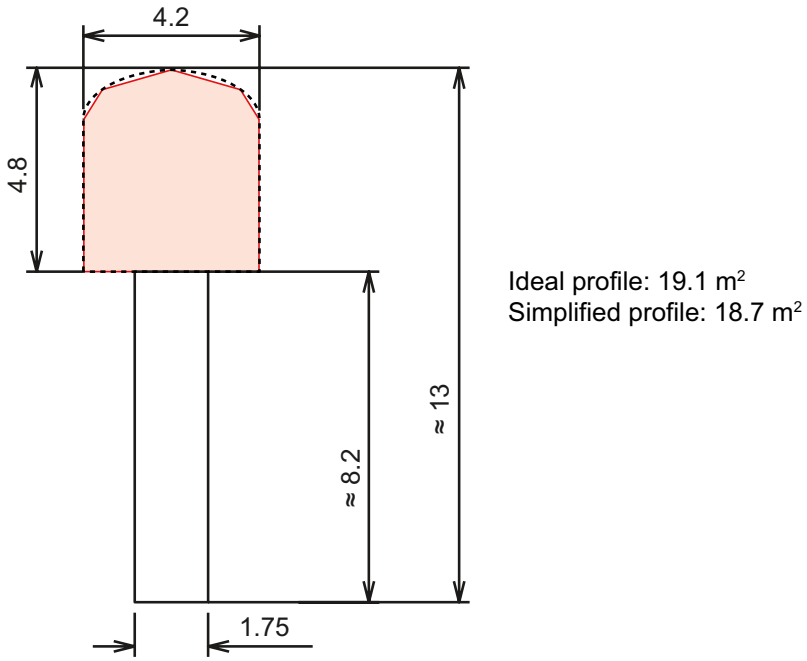

Figure 4-6. *Theoretical cross-sections according to underground design premises /SKB 2009b/. The simplified cross-section (red) has a slightly smaller cross-sectional area.*

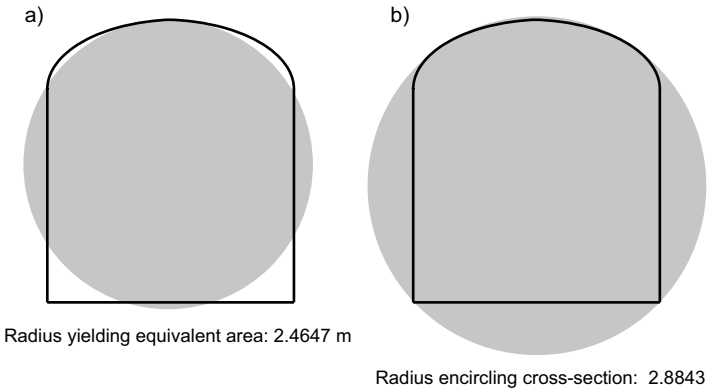

Figure 4-7. *Alternative definitions of equivalent radii to a drill and blast tunnel profile.*

4.4.2 Canister geometry

Like tunnels, deposition holes and canisters were simplified to line strings (Figure 4-8). The number of sides defined by these line strings was implemented as a variable. The endcap of the cylinders was implemented as horizontal line strings, trending NS and EW respectively, at the top and bottom of the cylinders. Benchmarks showed that 8 sides were sufficient to obtain reliable results.

4.4.3 Canister location

The spacing of deposition holes was implemented as a variable, using 6 m as the base case (see Section 5.1). According to Underground Design Premises /SKB 2009b/, positioning of deposition holes starts about 17 m from the transportation tunnel and ends about 10 m from the end of the deposition tunnel. As these numbers were preliminary set at the time of writing, we simplified the geometry in the simulations by using two 15 m long sections at the beginning and end of the deposition tunnels as illustrated in Figure 4-9.

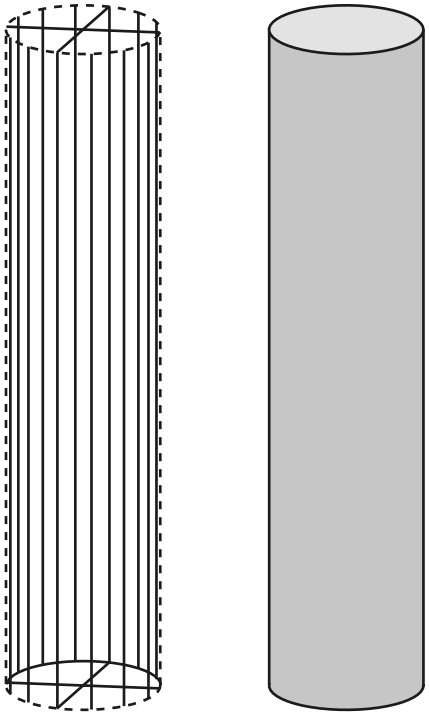

Figure 4-8. *Deposition holes and canisters are simplified to line strings.*

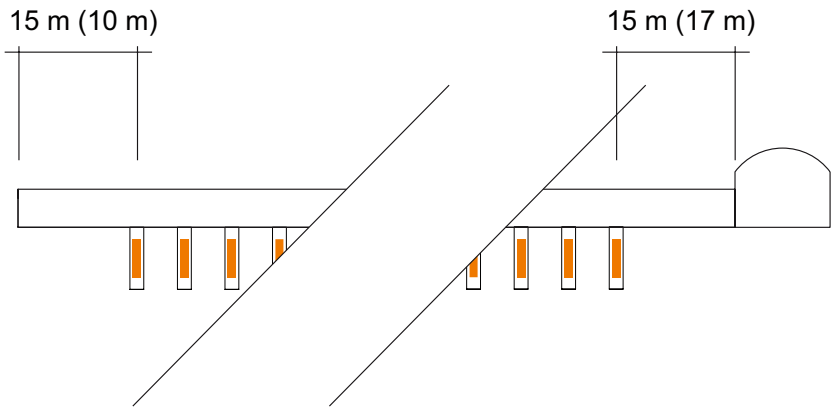

Figure 4-9. *Implementation of tunnel ends in the simulation as compared to Underground Design Premises (in parentheses, from /SKB 2009b/).*

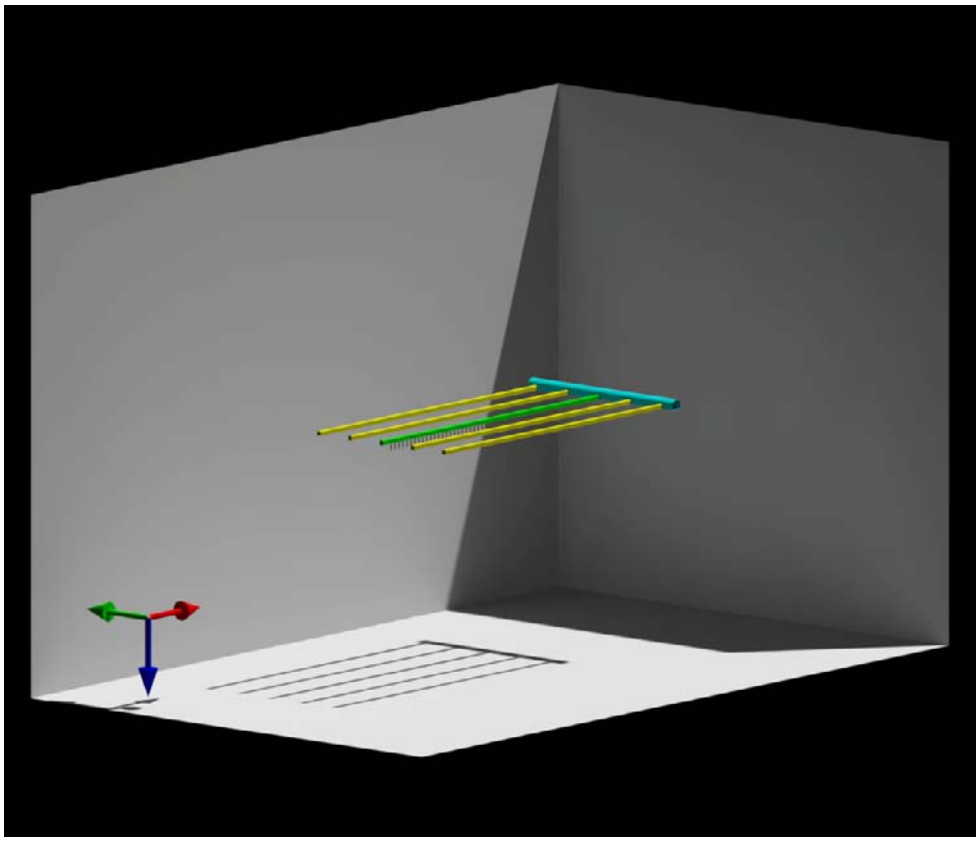

Figure 4-10. *Tunnels used in the simulations.*

4.4.4 Neighbouring tunnels

In a few test cases, we explored the possibility to utilise fracture intersections in other tunnels of the repository. For this implementation, we used dimensions of the transportation tunnel as provided in Underground Design Premises /SKB 2009b/. The spacing of deposition tunnels was implemented as a variable, but never set to any other value than 40 m in any simulation. A total of 5 deposition tunnels and one transportation tunnel was implemented, as illustrated in Figure 4-10.

4.5 Reducing the number of fractures

The model volume of the base case (see Section 5.1) is roughly 500×500×800 m (See Section 4.3). The base DFN would in such a volume yield approximately 10^6 fractures in each realisation. It is desirable, from a simulation time perspective, to reduce the number of fractures, naturally without any loss of simulation quality. We do so by filtering out all fractures that are located such that they cannot intersect any part of the tunnel/canister system. The principle is illustrated in Figure 4-11. We construct an imaginary envelope around the tunnel/deposition hole system as in Figure 4-11b. The radius of such an envelope is computed from the dimensions of the tunnels and deposition holes, which are treated as variables. In the base case, the radius of the envelope is roughly 9.86 m. We then assume all fractures are perpendicular to the tunnel. This ensures a minimum distance from the fracture centre to the boundary of the enveloping cylinder. Finally, we compute the distance from the fracture centre to the x-axis of the coordinate system (Figure 4-11). If it is larger than the fracture radius, the fracture is excluded from further analysis. A more sophisticated filter could have been designed by using half spheres at both ends of the tunnel, but the small gain in memory and speed was not considered worth the effort in terms of additional benchmarks and complexity of the codes.

The effect of the filtering is dramatic, the number of fractures is reduced by three orders of magnitude (Figure 4-12), yielding roughly 1,000 fractures to consider in each realisation.

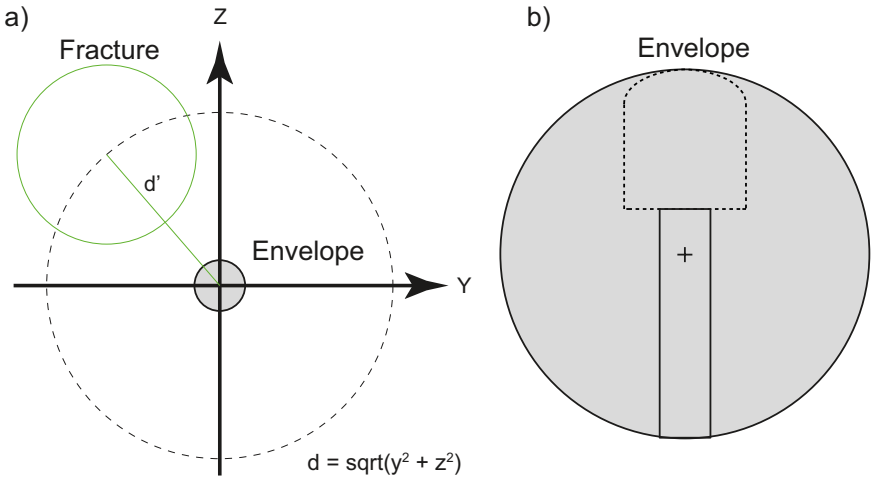

Figure 4-11. *Method for filtering fractures unable to intersect the tunnel/canister system.*

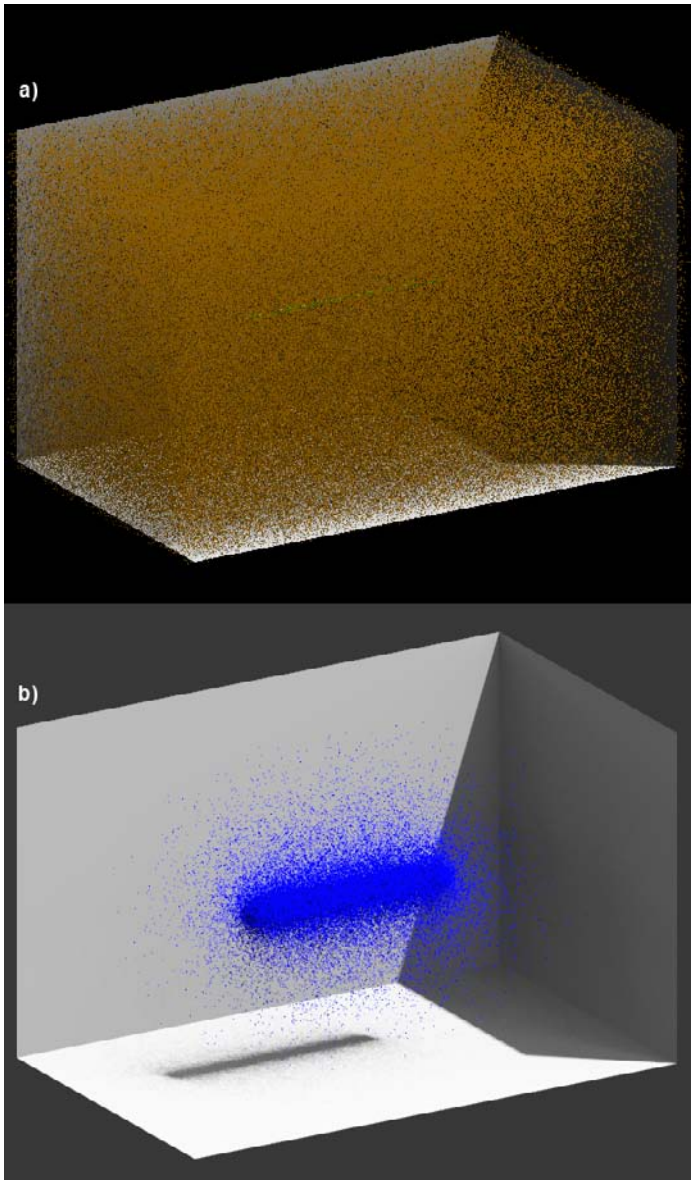

Figure 4-12. *a) Fracture centroids for a sample realisation of the base model (only 10% of the centroids are shown for clarity). b) The number of fractures is reduced by filtering (only centroids of FPI fractures shown).*

4.6 Simulation flow

The first step in the simulations is to generate a fracture array according to a given DFN model. The DFN model steers the orientations, sizes, intensities and spatial arrangement of the fractures within the model volume. Next, the fracture network is tested for FPI with the tunnel; fractures that make FPI's with the tunnel are tagged as such and saved to file (optional). Starting from the position of the first deposition hole, we then try all FPI fractures for potential intersection with canisters. If none intersects, the position is accepted and a new position is tested a standard-distance D away (6 m in the base case, see Section 5.1). If, however, the position is intersected, we move the position until the extrapolation of the fracture no longer intersects (Figure 4-13). For computational convenience, we implement this reasoning in the codes by moving a small distance d and test all fractures again. The latter step is repeated until either the position is accepted or the end of the tunnel is reached. The effect of using different step-lengths, d, is explored in Section 5.10.

The standard-distance, D, is governed by, among other factors, the thermal properties of the rock /SKB 2004/. The distance "d" should be as small as possible but there will be a trade off between optimisation and computation speed. We found d = 1 m appropriate for the purpose of the simulations presented here.

Fractures that do not make any FPI with the deposition tunnel are thereafter tested according to the EFPC criterion, and deposition holes fulfilling the criteria are deleted from the deposition hole array. Remaining deposition holes that are intersected by fractures larger than the prescribed critical radius are identified and tagged as potentially critical. Depending on "decaying slip" option (see Section 6.2) an additional test might be performed to check if the canister lies within the critical portion of the fracture. Finally, the degree-of-utilisation and number of critical positions is computed for each realisation. Results of all realisations are concatenated and saved to file together with the position arrays and the network of fractures intersecting any part of the tunnel-canister system.

The flow of the simulations is outlined in Figure 4-14 and has been designed to, as realistically as possible, mimic the procedure anticipated during the construction of the repository.

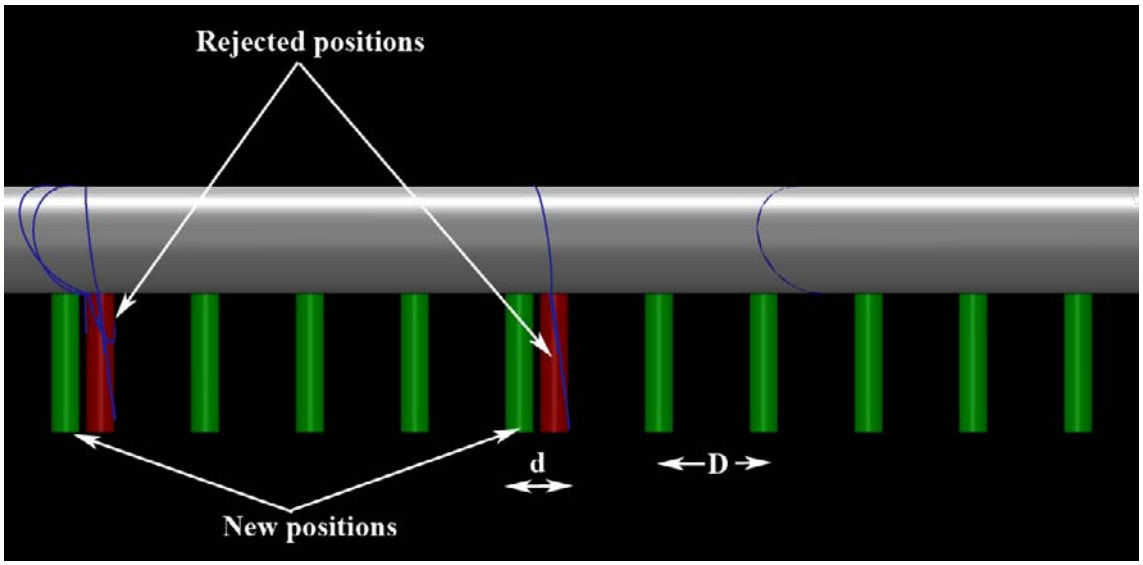

Figure 4-13. *Principles for simulating the application of the FPC criterion and its consequence in terms of degree-of-utilisation.*

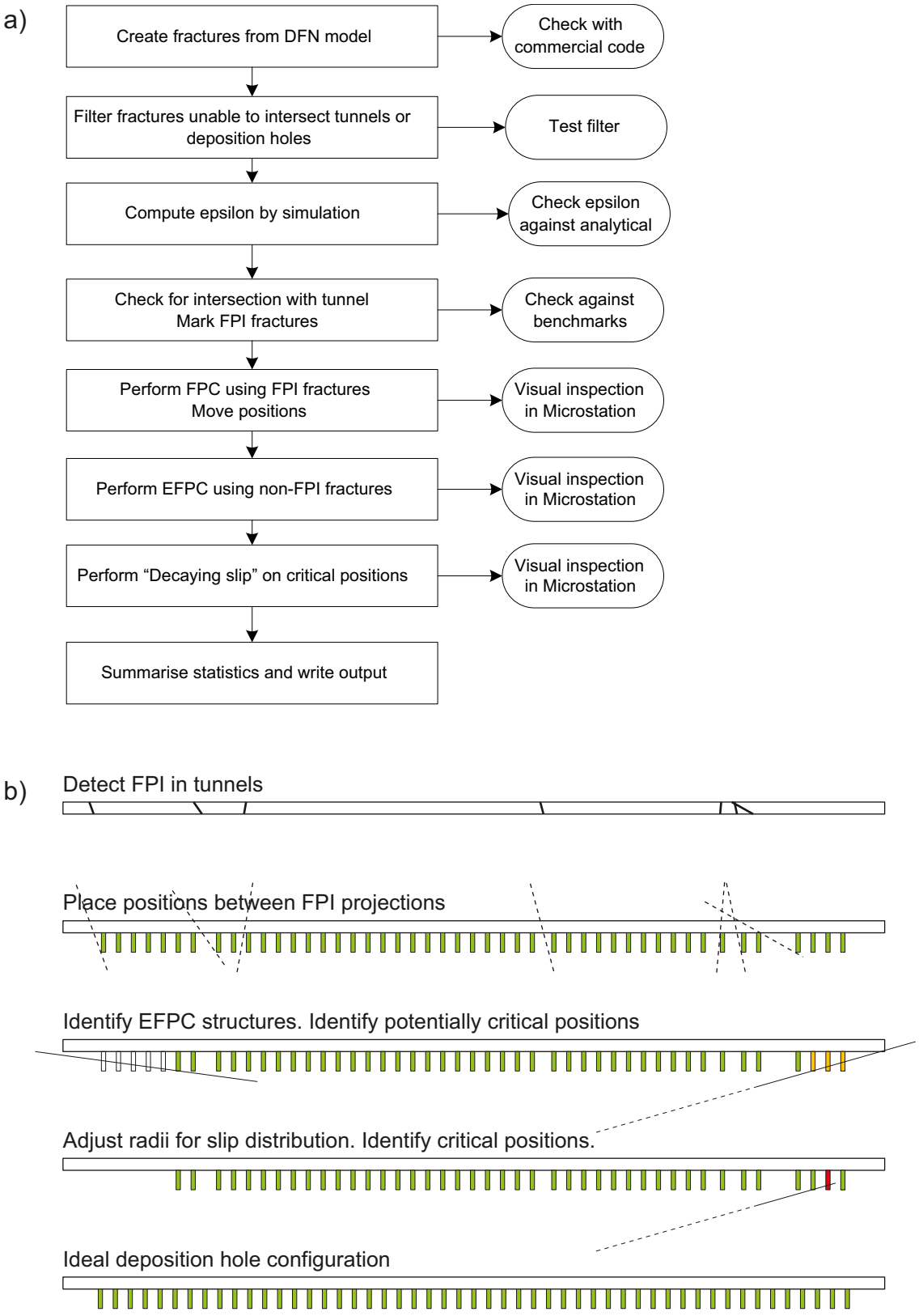

Figure 4-14. *a) Simulation flow and tests performed to check each step. b) visualisation of selected steps in the flowchart.*

4.7 Quality assurance

We have implemented all codes as /Matlab 2008/ m-scripts. Computationally demanding subroutines were compiled from C++ versions of the m-scripts. However, the use of these MEX-routines was made optional and is steered by toggles, thereby making review of the uncompiled algorithm amenable.

The simulation input simply consists of ASCII files containing DFN models. Simulation prerequisites such as tunnel dimensions, FPI criteria, etc are declared in a special "setup" m-script.

The output consists of a number of ASCII files, the essence of which is the following:

- All fractures intersecting any part of the tunnel system. The file contains coordinates of the centroids, orientation, radius, intersection type with tunnel, intersection type with neighbouring tunnel, flag for intersection with canister and realisation number. As the file can grow beyond what is practical, this output is optional (steered by setup-script)
- Canister positions. The file contains coordinates, realisation number, Model ID (identifier to input DFN model) and various intersection flags.
- The main simulation output containing realisation number, number of FPI/100 m, degree-of-utilisation using FPC, degree-of-utilisation both FPC and EFPC, number of critical positions, Model-ID, simulated P_{32} and Simulated ε.
- Postscript graphs displaying FPI/100 m and degree-of-utilisation as function of realisation number.

The analyses of the simulation output, in terms of graphs, tables and statistics have been performed with /Statistica 2009/. Two Statistica workbooks contain all the results of this study. One workbook contains only benchmark and test results whereas the other workbook contains site-specific results.

We have chosen to use /Subversion 2009/ as the version control system with /TortoiseSVN 2009/ as the shell to Windows Explorer. The version control system allows us to reconstruct all codes to a state of a given date. TortoiseSVN also handles all simulation input, output and Statistica workbooks.

5 Benchmarking and testing the codes

In this section, we present the results of various benchmarks and tests, the purpose of which is to make credible that the codes work as intended. As the aspects of stochastic geometry, as explored within this work, is an intricate interplay between various parameters of the DFN model, tunnel-geometries, FPI criteria and various assumptions, it has been necessary to explore various aspects of the simulations in a multitude of separate tests.

Additionally, we have during the course of work made misjudgements, mistakes and erroneous assumptions (partly due to the notoriously slippery nature of the powerlaw distribution), which necessitated special tests for debugging purposes; some routes of reasoning led to cul-de-sac, others tests were redundant. Yet, though not strictly necessary for the work herein, we choose to provide the results of these tests for documentation purposes and to potentially aid an interested reader to not repeat some of our mistakes.

5.1 Benchmark input

For the benchmarks we found it practical to define a "base case", from which variants can be created thereby enabling the impact of specific parameters to be determined holding all other aspects constant. For the base case DFN, we have chosen to use the so called "r_0-fixed-alternative model" of the Forsmark Site[4]. This model consists of 4 "global" fracture sets and 5 "local" sets /see Fox et al. 2007 for details/. The global sets are thought of as being uniformly present within the model volume whereas local sets only occur in sub volumes with specified densities and probabilities. For the purposes of benchmarking the codes, we did not find it necessary to implement the local fracture sets; the base case is presented in Table 5-1.

Additionally, the following prerequisites were chosen for the base case:

- The deposition tunnel was oriented in 123°. This coincides with the orientation of most tunnels at Forsmark /SKB 2009b/.
- Only one tunnel was used.
- Drill and blast tunnel profiles were used as the base case. For benchmark cases when cylindrical tunnels were simulated, the tunnel radius was set to either 2.4647 or 2.8843 m depending on the specific aspect to highlight.
- The tunnel length was set to 330 m, which includes two 15 m empty sections at each tunnel end (see Section 4.4.3).
- The "deterministic" decaying slip option (see Section 6.3) was enabled.
- The minimum fracture radius was set to the tunnel radius, or to 2.8843 m if drill and blast profile was used. The maximum fracture radius to consider was set to 250 m.
- The canister failure criterion was set to 5 cm /SKB 2009c/.
- The canister spacing was set to 6 m which, for the base case using 300 + 30 m tunnels, would yield 51 canister positions in each tunnel realisation.
- The EFPC criterion was set to 5 or more intersections (based on sensitivity analyses, Section 6.2). Additionally, to count as an intersection, full perimeter intersections were required in the intersected *deposition holes*.
- Any intersection (a-h, Figure 4-1) of the canister (criterion "b" in Figure 3-1) counts for FPC to be fulfilled.
- The critical radius was set to $r = 75$ m.

[4] /Modelldatabasen 2007/. Model: PFM DFN 2.2.xls. Version 0.6. Approved 2007-11-29, Modeller: A. Fox. Simon ID: GEO_WTAGLLAA. https://service.projectplace.com/pp/pp.cgi/r232241793 (access might be given on request).

Table 5-1. DFN model used as base-case. It is identical to the Forsmark "r_0-fixed" alternative for fracture domain FFM01 with the local fracture sets omitted[5]. Note that the trend and plunge refers to the pole of the fracture.

Set	Type	Trend	Plunge	Kappa	r_0 (m)	kr	–	Global P_{32}	Distrib.	rmax (m)
NE	Global	314.90	1.30	20.94	0.039	2.718	0.000	1.733	1.000	564.200
NS	Global	270.10	5.30	21.34	0.039	2.745	0.000	1.292	1.000	564.200
NW	Global	230.10	4.60	15.70	0.039	2.607	0.000	0.948	1.000	564.200
SH	Global	0.80	87.30	17.42	0.039	2.579	0.000	0.624	1.000	564.200

5.2 Check of the generated fracture network

5.2.1 Check of orientation

In this section, we test that the fracture orientations are correctly simulated. We do so by halting the FPC simulation just after the generation of the fracture network and plot the fracture orientations in a commercial code /StereoStat 2007/ in which the orientations are analyzed.

The results are displayed in Figure 5-1 and Table 5-2. Please note that the number of digits in Table 5-2 are given from the DFN model and Stereostat. Regardless, the simulated fracture orientations are essentially identical to the ones dictated by the DFN model and we therefore conclude that the codes correctly simulate fracture orientations according to the DFN model.

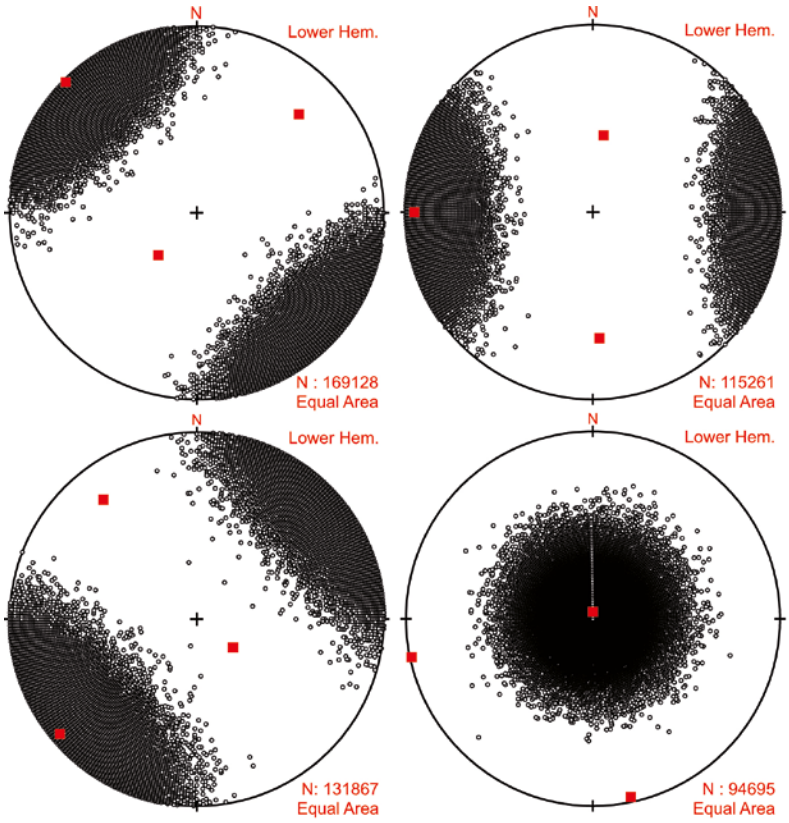

Figure 5-1. *Sample realisation of the base case, separated by sets. The red squares represents the eigenvectors, used to determine the mean pole direction.*

[5] /Modelldatabasen 2007/. Model: PFM DFN 2.2.xls. Version 0.6. Approved 2007-11-29, Modeller: A. Fox. Simon ID: GEO_WTAGLLAA. https://service.projectplace.com/pp/pp.cgi/r232241793 (access might be given on request).

Table 5-2. The table shows simulated orientation statistics (given as trend and plunge of the fracture pole) compared to the orientations obtained used in the DFN model.

DFN model			Simulation		
Trend	Plunge	Kappa	Trend	Plunge	Kappa
314.9	1.3	20.943	315	1	20.99
270.1	5.3	21.33938	270	5	21.42
230.1	4.6	15.70056	230	5	15.7
0.8	87.3	17.4185	0	87	17.41

5.2.2 Check of size distribution

Here, we test to ensure that the size distribution is generated as intended, before any filter is applied to the fracture network.

The test was performed as follows: 50 realisations were made on each fracture set of the base case, using a lower truncation level (r_0) of 2.8843 m (see Section 5.1). The intensity, P_{32}, was rescaled using equation 3-17 of /Hermanson et al. 2005/, here slightly revised in terms of variable names for clarity:

$$P_{32,[r_{\min,new}-r_{\max,new}]} = P_{32,[r_{\min,old}-r_{\max,old}]} \frac{r_{\max,new}^{2-k_r} - r_{\min,new}^{2-k_r}}{r_{\max,old}^{2-k_r} - r_{\min,old}^{2-k_r}} \qquad \text{Eq. (18)}$$

The equation simply states that if the fracture population of the model is truncated at a new lower (and/or upper) level(s), the intensity must be adjusted for accordingly. In other words, the consequence of increasing r_0 is a decrease of the number of fractures and hence a decrease of the total fracture area in the model volume.

Estimation of the parameter r_0 is trivial, it is simply the minimum value of fracture radius for each set:

$\hat{r}_0 = \min(r)$

The maximum likelihood estimator of k_r is /Evans et al. 2000/:

$$\frac{1}{k_r} = \left(\frac{1}{n}\right)\sum_{i=1}^{n} \log\left(\frac{r_i}{\hat{r}_0}\right)$$

The average of these 50 realisations was computed for each DFN parameter. The intensity was kept constant for all the sets, using 10^6 fractures per realisation and set. Additionally, we computed the number of large fractures, the limit arbitrarily set to r = 150 m, to check against the analytical solution provided by equation (17) as the larger fractures are particularly important to our work. The result of this test, provided in Table 5-3, indicate an almost perfect match between simulated and analytical size parameters.

In this test, we also included a test of the mean orientation of the same fractures, as it imposed insignificant additional programming efforts. The mean orientation was obtained by computing the largest eigenvector of the array of fracture normals /Davis 1986/. This test confirms the results of the test in Section 5.2.1 but also confirms that the results are stable over many realisations.

In summary therefore, we conclude that both the orientations and the sizes are correctly simulated, and that these are stable over many realisations.

Table 5-3. Difference between simulated and analytical DFN parameters.

50 realisations of the base case, local sets	Set #1	Set #2	Set #3	Set #4
r_0	2.8843	2.8843	2.8843	2.88430
kr	2.7193	2.7469	2.6088	2.58059
N > 150	16.0000	13.9600	24.4800	26.50000
Mean trend	314.9000	270.1008	230.1005	0.76832
Mean plunge	1.3011	5.3001	4.6019	87.30244
Kappa	20.9457	21.3399	15.7007	17.41780
Difference (simulated-analytical)				
r_0	0.0000	0.0000	0.0000	0.0000
kr	0.0014	0.0021	0.0015	0.0016
N > 150	–0.2687	–0.7300	–0.2181	–0.9772
Mean trend	0.0000	0.0008	0.0005	–0.0317
Mean plunge	0.0011	0.0001	0.0019	0.0024
Kappa	0.0027	0.0005	0.0001	–0.0007

5.3 Check of P_{32}

The intensity of fractures is defined by the DFN model in terms of fracture area per unit volume (m^2/m^3) commonly denoted P_{32}. Ideally, fractures should be generated until the intensity is saturated, taking truncation effects with the model boundaries into account. The simulations, however, are implemented to honour the number of fractures per unit volume, P_{30}, according to transformation provided by equation (17), which is a fundamentally faster method. Though this should render equal results for infinite model volumes, truncation effects at the model boundaries will tend to overestimate the P_{32} intensity, as the area summation includes portions of the fractures lying outside the model volume. This effect becomes more accentuated the smaller the model volume. However, as the results of this test show (Table 5-4), the model volume is sufficiently large as to render truncation effects insignificant to our simulations. We may therefore, which is also supported by the test in Section 5.2.2, conclude that fracture intensities are correctly implemented in our codes.

5.4 Test of intensity (P_{10})

The purpose with these tests was to systematically alter, one at a time, key parameters of the simulation environment and test against a known solution to track programming errors. The tests of this section are based on idealised cases for which there exist analytical or semi analytical solutions to compute P_{10} from P_{32} and other parameters, e.g. /Wang 2005/. Allan Hedin /Hedin 2011/ independently developed semi analytical solutions similar to those of /Wang 2005/, and implemented the algorithms as excel-sheets which, with minor modifications, were used to compute the semi-analytical solutions.

Table 5-4. Difference between simulated and theoretical P_{32}.

Set	Rescaled P_{32}	Simulated P_{32}	Sim/Theor
NE	0.0750889	0.0755509	100.62%
NS	0.0500507	0.0503585	100.62%
NW	0.0645195	0.0650042	100.75%
SH	0.0475728	0.0479718	100.84%

Some of the theoretical solutions provided below assumes $\kappa = \infty$ or 0, and tunnel radius exactly = 0. It was possible to implement collision tests in the Matlab codes in which these prerequisites are fulfilled. However, we found it more useful to make use of the sharp versions of the codes and mimic as far as possible the prerequisites for the tests. More precisely, tunnels were not simulated as infinitely thin lines, but as cylinders with very small radii. This enabled us to track down errors in the cylinder/plane collision tests. Similarly, rather than forcing all simulated planes to have exactly the same orientations, we randomly picked fractures from a Fisher distribution with a very high value of κ, which enabled us to test the routines handling fracture orientations. The largest value of κ that could be handled was 500, after which we encountered numerical problems.

The simulation input and outcomes of the tests are commented on briefly in subsections below and are summarised in Table 5-5, and in Figure 5-2.

Table 5-5. Summary of test results for the different benchmark cases "A"-"I".

Properties	A	B	C	D	E	F	G	H	I
Tunnel trend	90	90	90	0	25	90	90	10	50
Tunnel radius	0	0	0	0	0	0	2.8843	2.8843	2.8843
Max fracture radius	50	50	50	50	50	50	50	50	50
Fracture mean pole Trend	90	90	90	25	0	90	90	50	10
Fracture mean pole Plunge	0	0	25	0	0	0	0	30	30
k	inf	0	500	500	500	1	500	500	500
r_0	2.5	2.5	2.5	2.5	2.5	2.5	2.5	2.5	2.5
k_r	3	3	3	3	3	3	3	3	3
P_{32}	2	2	2	2	2	2	2	2	2
Expected FPI/m (closed form solution)	2	1	1.813	1.813	1.813	1.076	0.483	0.235	0.235
Expected FPI/m (numerical integration)	1.899	0.951	1.722	1.721	1.721	1.023	0.482	0.235	0.235
Simulated FPI/m	1.975	0.988	1.791	1.791	1.789	1.062	0.503	0.234	0.234

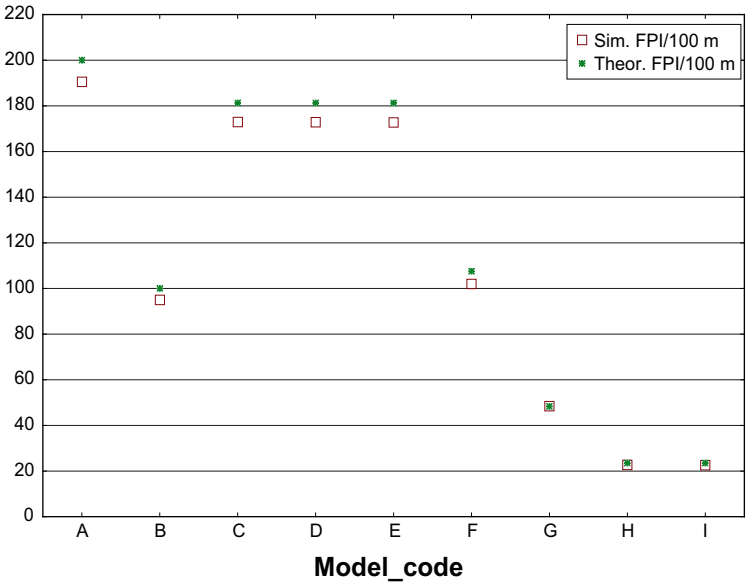

FPI_benchmarks in Benchmark analyses.stw
2010-03-10 10:31:38

Figure 5-2. *Comparison of simulated number of FPI with those predicted by a semi-analytical solution (values from Table 5-5).*

5.4.1 Test A

The simplest test assumes a uniform orientation of the fractures, i.e. all fractures are exactly parallel. If the fractures are perfectly perpendicular to the tunnel axis, the number of FPI per unit length (i.e. the P_{10} for an infinitely thin cylinder) should equal the fracture intensity, i.e:

$$P_{10} = P_{32} \qquad \text{Eq. (19)}$$

A uniform orientation distribution was mimicked by setting the Fisher κ to 500 in the simulations ("A" in Table 5-5) and tunnel radius set to 0.01 m. We were, unfortunately, not able to simulate tunnel radii with smaller values (in Matlab) without encountering numerical oddities. Nevertheless, the simulated value of P_{10} agrees well with the expected theoretical value. The small deviation is attributed to the finite radius of the tunnel and, more importantly, finite length (See Section 5.6).

5.4.2 Test B

Another simple test assumes completely random orientations of the fractures. The predicted number of FPI per unit length (P_{10} for an infinitely thin cylinder) is:

$$P_{10} = \frac{1}{2} P_{32} \qquad \text{Eq. (20)}$$

In the simulations ("B" in Table 5-5), a random orientation distribution was mimicked by setting the Fisher κ to 0.0001 (it was not possible to simulate using a κ of exactly zero as assumed by the analytical solution). The simulated value of P_{10} agrees well with the expected theoretical value (Table 5-5, Figure 5-2).

5.4.3 Tests C to E

In these tests we alter either the orientation of the tunnel or the mean pole trend of the fractures by the same amount. Therefore the results are expected to be equal. The theoretical P_{10} for cases C, D and E are:

$$P_{32} \,|\cos\,(plunge)| \qquad \text{Eq. (21)}$$

$$P_{32} \,|\cos\,(trend)| \qquad \text{Eq. (22)}$$

and

$$P_{32} \,|\cos\,(tunneltrend)| \qquad \text{Eq. (23)}$$

respectively, were *plunge* and *trend* are the orientations of the mean fracture pole in radians. The simulated value of P_{10} agrees well with the expected theoretical value (Table 5-5, Figure 5-2)

5.4.4 Test F

This test differs from the tests in 5.4.3 only in that the parameter κ differs from (theoretically) 0 or infinity. The theoretical P_{10} is given by:

$$P_{10} = P_{32}\left(1 + \frac{1}{\kappa \sinh \kappa} - \frac{1}{\kappa \tanh \kappa}\right) \qquad \text{Eq. (24)}$$

The simulated value of P_{10} agrees well with the expected theoretical value (Table 5-5, Figure 5-2)

5.4.5 Test G

This test introduces finite tunnel radii to the tests while using perfectly parallel fractures perpendicular to the tunnel. For this test, we compute the theoretical P_{10} as /Hedin 2011/:

$$\overline{FPI} = P_{32}\left[\left(\frac{r_0}{r_T}\right)^{k_r-2} \frac{1}{k_r - 1}\frac{2}{k_r} + \left(\frac{r_0}{r_{Max}}\right)^{k_r-2}\left(2\frac{(k_r-2)}{(k_r-1)}\frac{r_T}{r_{Max}} - \frac{(k_r-2)}{k_r}\left(\frac{r_T}{r_{Max}}\right)^2 - 1\right)\right] \qquad \text{Eq. (25)}$$

The simulated value of P_{10} agrees extremely well with the expected theoretical value (Table 5-5, Figure 5-2).

5.4.6 Test H and I

The last two of the idealised test cases use oblique fractures and finite tunnel radii which renders the theoretical solution to solve for P_{10} more complex:

$$\overline{FPI} = P_{32}\left[\left(\frac{r_0}{r_T}\right)^{k_r-2}\frac{1}{k_r-1}\left(\left|\cos(\Delta)\right|^{k_r-1}-\frac{k_r-2}{k_r}\left|\cos(\Delta)\right|^{k_r}\right)+\left(\frac{r_0}{r_{Max}}\right)^{k_r-2}\left(\left|\cos\Delta\right|\left(\frac{(k_r-2)}{(k_r-1)}\frac{r_T}{r_{Max}}-1\right)+\frac{(k_r-2)}{(k_r-1)}\frac{r_T}{r_{Max}}-\frac{(k_r-2)}{k_r}\left(\frac{r_T}{r_{Max}}\right)^2\right)\right] \quad \text{Eq. (26)}$$

The simulated value of P_{10} agrees very well with the expected theoretical value (Table 5-5, Figure 5-2).

5.4.7 Base case per set

An overestimation of the number of FPI for one fracture set can be counteracted by an equally large underestimation for another set due to programming or input errors. In this test, we analyse the fracture sets of the base case separately to exclude the possibility of errors being neutralised due to e.g. differences in orientation. Simultaneously, we compare the simulated number of FPI using a drill-and-blast tunnel geometry to the expected values using circular cross-sections (equivalent radius or envelope, Figure 4-7).

Figure 5-3 confirms that all simulated sets produce FPI/100 m in accordance with the expected values and, equally important, that the implementation of the drill-and-blast geometry produces a number of FPI lying between the theoretical values using envelope (r = 2.8843) and equivalent radius (r = 2.4647) as expected.

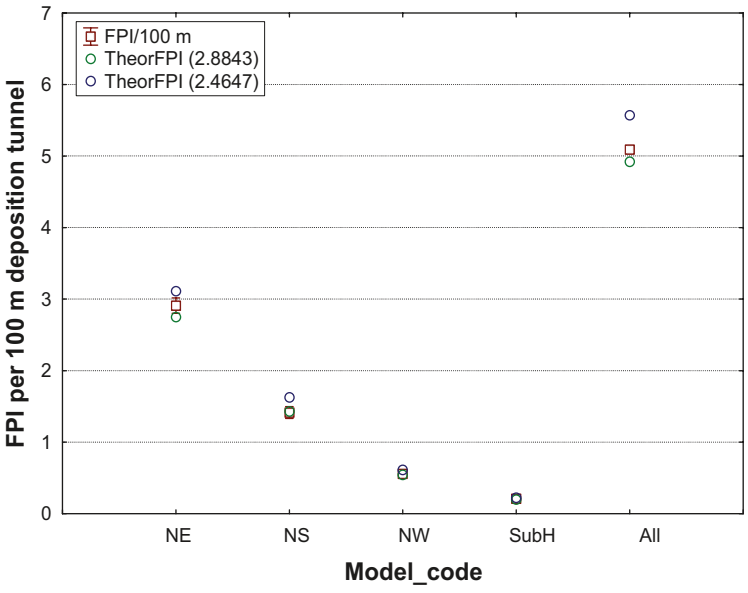

Base case per fracture set in Benchmark analyses.stw
2009-08-21 12:17:08

Figure 5-3. *Comparison of theoretical and simulated number of FPI/100 m for tunnel orientation = 123° (base case).*

5.4.8 Base case using tunnel rotation

As mentioned briefly in Section 4.4.1, the tunnel orientations are constant in all simulations, aligned parallel to the X-axis of the coordinate system. To simulate tunnels of other orientations than EW (X-axis), we rotate the fracture network rather than the tunnel, to avoid the burden of rotating coordinate systems; it is, simply, far easier to implement and control a rotating fracture network than an entire tunnel system.

Having confirmed an acceptable agreement between theoretical and simulated P_{10} along the tunnels aligned EW, for various tunnel radii, fracture orientations, etc (Sections 5.4.1 to 5.4.7), this test checks whether the implementation of rotation performs as expected and whether the agreement is equally acceptable for all tunnel orientations, using a full DFN model (base case). We make use of the same theoretical solution as for e.g. test "I" with the difference that we compute FPI/m for each set and sum all sets for each tunnel orientation.

Figure 5-4 shows the result using two different tunnel radii. A slight underestimation of the number of FPI as compared to the theoretical solution can be seen on the figure, despite the variability of the simulations. Yet, the theoretical solution lies within the 95% confidence interval of most simulations and we therefore nevertheless conclude that the codes are reliable in this context.

Finally, we checked the drill-and-blast cross-section /SKB 2009b/, the results of which are displayed on Figure 5-5. We note, as expected, that the simulations results lie between the two bounding, theoretical (circular) cases, and we may hence conclude that the logic for computing FPI works as intended for all tunnel rotations and for both cylindrical and drill-and-blast cross-sections.

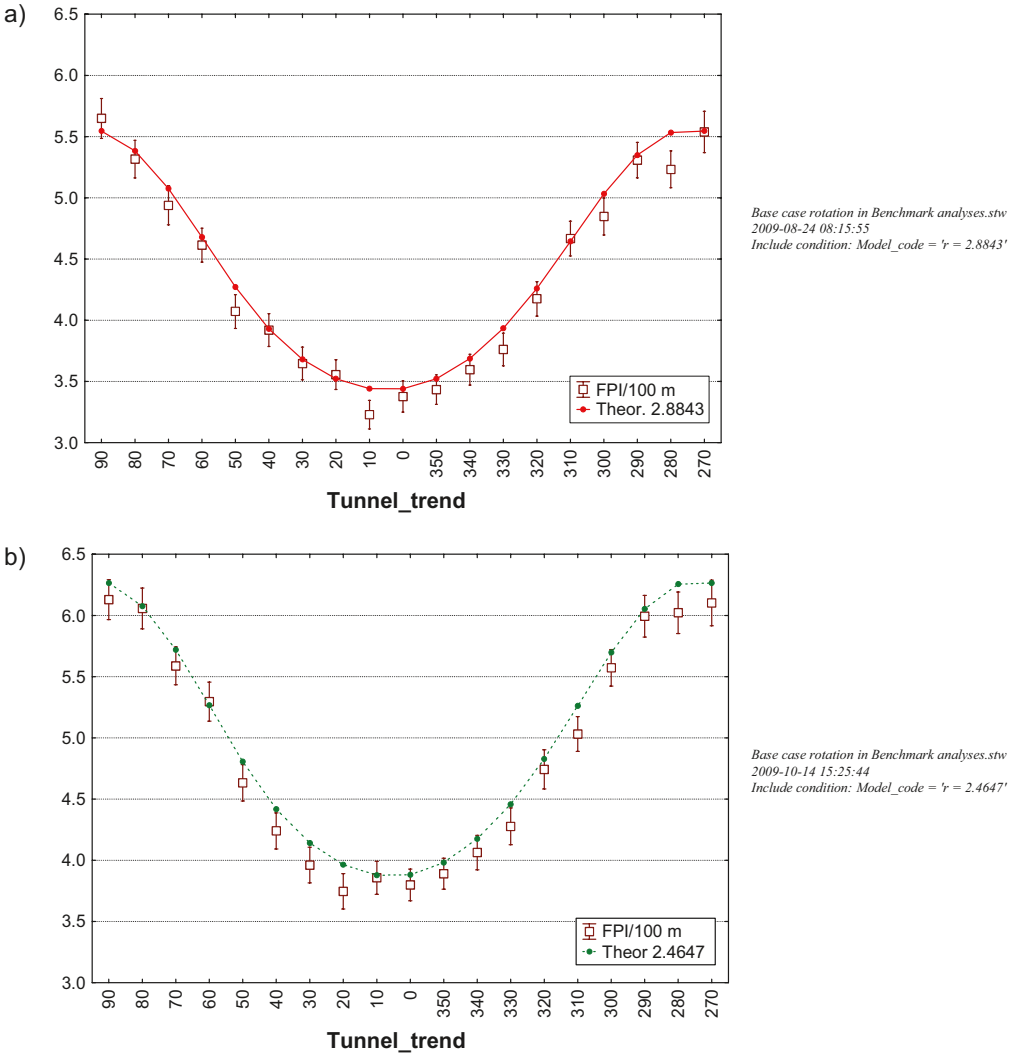

Figure 5-4. *Comparison of analytical and simulated number of FPI/100 m tunnel, using circular tunnel cross-sections of 2.8843 m (a) and 2.4647 m (b) respectively.*

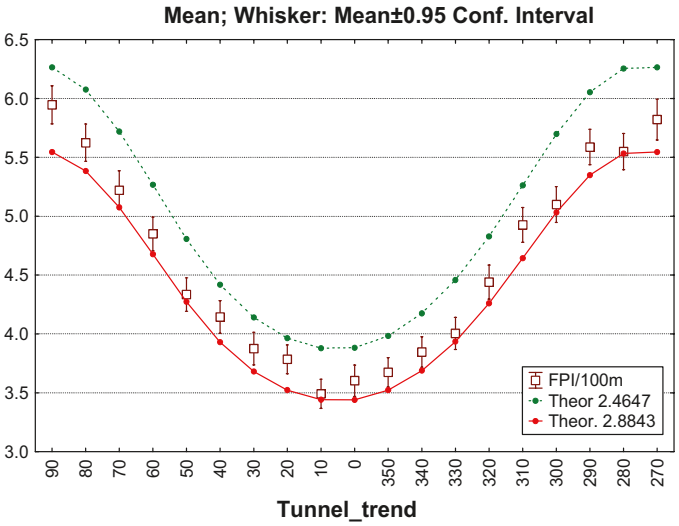

Figure 5-5. *Comparison of theoretical and simulated (base case) number of FPI/100 m for all tunnel orientations in steps of 10°.*

5.4.9 Comments on the test results

As is fairly clear on Figure 5-2 and Figure 5-5, the simulations slightly underestimate the number of FPI (or P_{10} if tunnel radius ≈ 0) for test cases A–E using circular tunnels. We attribute this "discrepancy" mainly to the finite dimensions of the simulated tunnel. In Figure 5-6 we display the ratio simulated/theoretical FPI/100 m which accentuates the difference shown on Figure 5-5.

The analytical solutions assumes infinite cylinders ("tunnels") whereas the simulated tunnels are indeed finite. In an infinite tunnel, there is no endcaps and intersections of the type "e", "f" and "g" (Figure 4-1) cannot occur. The shorter the simulated tunnel the higher the proportion of endcap intersections. At its extreme, if the tunnel is very (infinitely) short, there will not be any FPIs and only various endcap intersections are possible. This effect is explored further in Section 5.6.

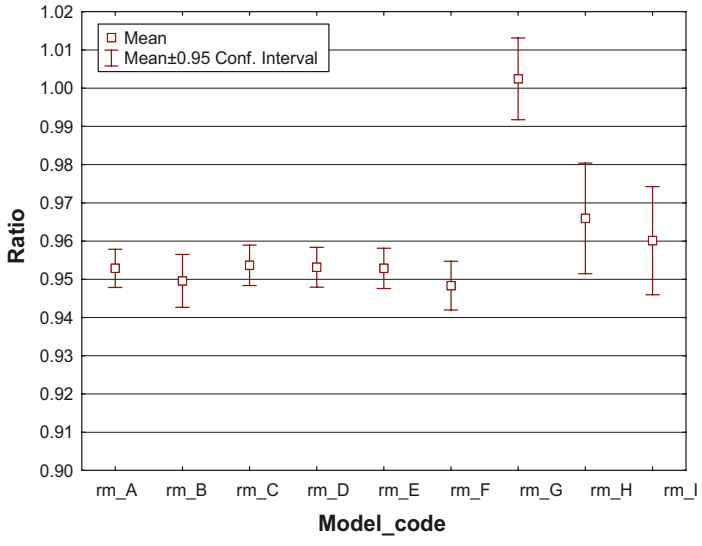

Figure 5-6. *The ratio of simulated/theoretical FPI/100 m accentuates that simulations generally yield fewer FPIs than predicted by analytical solutions.*

The careful reader would perhaps object that this effect ought not affect test cases A and C because the "fractures" are perpendicular to the tunnel, and that endcap intersections should therefore not occur by definition. However, we recall that a uniform distribution of fracture orientation was *mimicked* in the simulations by setting the Fisher κ to 500. Though this is indeed a very large value ensuring an extremely tight fracture cluster, there will still be a small number of fractures which deviate sufficiently from the mean orientation as to create endcap intersections. As these are not counted as FPI (by definition), the number of intersections per unit length, P_{10} or FPI depending on tunnel radius, will never fully reach the number expected from the analytical solution. The effect of kappa is discussed further in Section 5.7.

5.5 Format of results

Most of the tests, benchmarks and site-specific simulations consist of comparisons of cases with different parameters. We found it practical, therefore, to present results mainly in terms of mean values with whiskers representing some measure of spread /Tukey 1977/. In order to check whether differences in means are statistically significant, confidence intervals are appropriate as whiskers. However, this essentially requires the sample to be Gaussian. Though this was found to be the case for small samples (< 5,000 realisations) of the number of FPI/100 m, large samples of FPI/100 m

a)

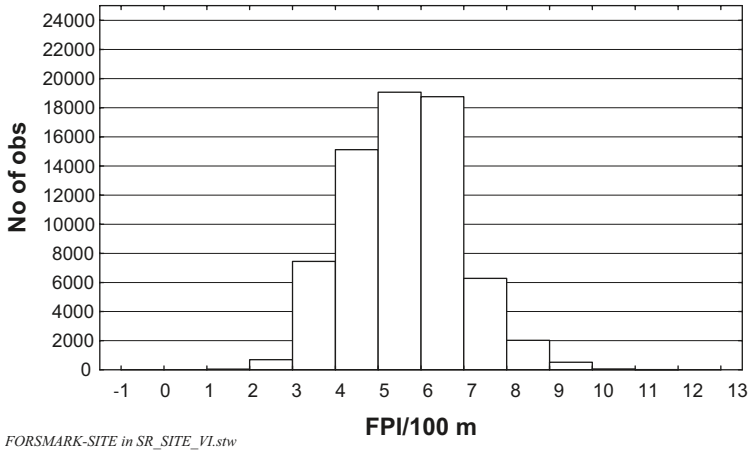

FORSMARK-SITE in SR_SITE_VI.stw
2010-01-12 14:58:39
Include condition: ModelID = 'r0_fix, FFM01'

b)

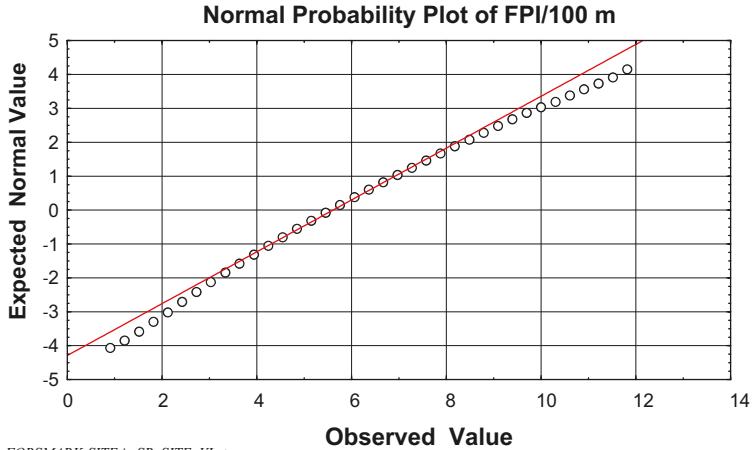

FORSMARK-SITE in SR_SITE_VI.stw
2010-01-12 15:51:00
Include condition: ModelID = 'r0_fix, FFM01'

Figure 5-7. *The statistical distribution of the output differs with studied metric. For example, the histogram of the number of FPI/100 m appears to display a familiar bell shape (a). However, when examined on a normal probability plot it displays a clear deviation from this assumed Gaussian distribution.*

(Figure 5-7) and other metrics of interest displayed Lognormal or Pareto distributions for which such a box-plot construct would obscure the skewness of the distribution. Yet, the shape of the distribution is of minor importance for this study which has focused on the differences between various cases. For practical purposes therefore, we chose to present results in terms of sample means and standard errors, which are directly comparable regardless of underlying distribution. For cases with Gaussian distribution, i.e. most of the benchmark cases, we made use of sample means and confidence intervals ($\alpha = 0.05$).

5.6 Effect of finite tunnel length

The length of the tunnels to be simulated impacts the outcome of the simulations. Short tunnels yield more endcap intersections per unit length than long tunnels. As the theoretical solution assumes infinite tunnel lengths, the simulation results can only asymptotically approach (a limit near) the theoretical results with increasing tunnel length as shown in Figure 5-8.

In this test, we used the benchmark case "I" (Section 5.4.6) to explore this effect by gradually increasing the simulated tunnel length. The simulations reach a plateau at about 200–300 m tunnel length after which longer tunnels do not produce more FPI/100 m. This test show that though the tunnel length indeed has a dramatic effect upon the computed number of FPI/100 m for shorter tunnel length, it is not the only explanation for the discrepancy with the analytical solution. We explore another factor in Section 5.7.

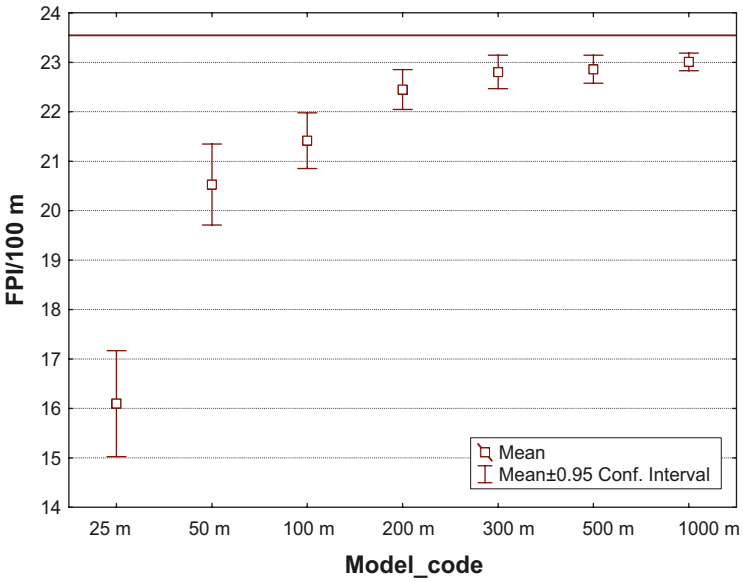

Figure 5-8. *The graph shows that the number of FPI/100 m approaches the theoretical value as the tunnel length increases.*

5.7 Effect of kappa

The deviation (underestimation) from the theoretical value of FPI/100 m can also be explained by the finite size of the κ value, i.e. the measure of concentration around fracture normals. The theoretical solution assumes an infinite κ value, meaning that all fractures are perfectly parallel. A practical upper limit of the κ value in the simulation codes is 500. Though this might be perceived as a very large value of κ, half of the fracture normals still deviate more than 3° from the mean pole (Figure 5-9), which is enough to produce a certain number of endcap intersections rather than FPIs, leading to an underestimating of the latter. This is however a subordinate effect. The impact of κ on the FPI/100 m value is shown in Figure 5-10.

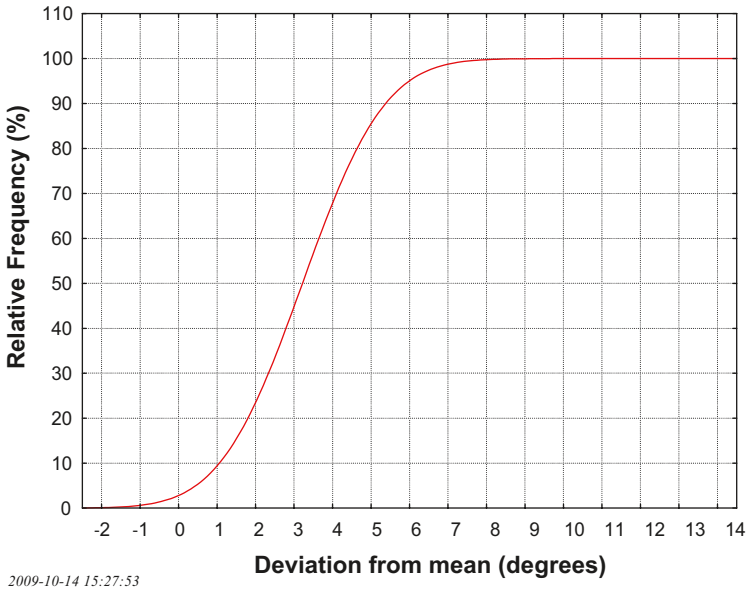

Figure 5-9. *The cumulative density function shows that 50% of the poles deviate more than 3° from the mean pole, using κ = 500.*

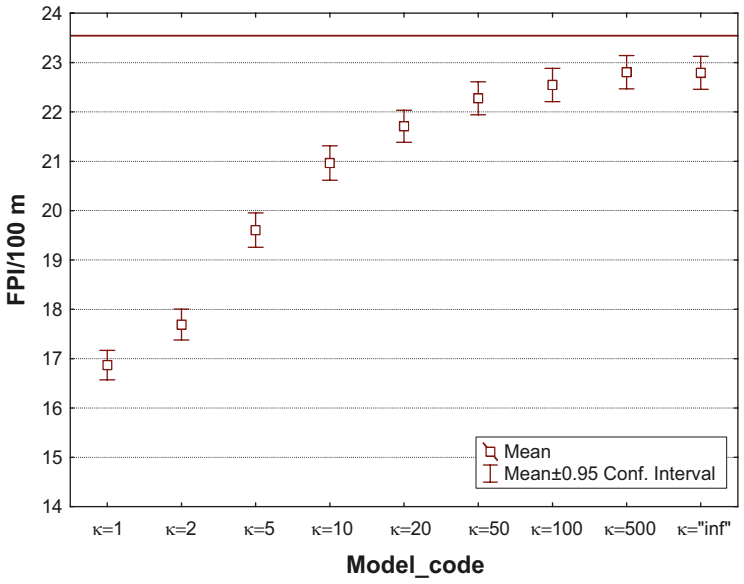

Figure 5-10. *Effect of number of FPI/100 m as a function of Fisher κ (bench case "I").*

5.8 Test of varying random seed

One of the first actions of this work was to find an optimal number of realisations for the metric of interest to obtain a stable mean value. Of the numerous outputs from the simulations, we elected to focus on the number of FPI/100 m. Having convinced ourselves that the collision tests worked as intended by benchmarking against analytical solutions (see previous sections), we ran the benchmark case until two consecutive values of FPI/100 m differed less than a certain prescribed value (with an upper limit of 2,500 realisation). We found such a limit at roughly 200 realisations (Figure 5-11), and decided that 250 realisations ought to be adequate for the our purposes.

Though this does not in any way deviate from good simulation practice, this was a major mistake because it turned out that, which is obvious in retrospect, the number of necessary realisations for a metric to stabilise varies with the metric itself. While 250 realisations was indeed sufficient for computation of FPI, it was far from sufficient for obtaining a stable mean number of critical positions (i.e. positions that escaped detection criteria, FPC and EFPC).

In most realisations there are no large fractures escaping detection; critical positions are so called *rare events*. This means that we need many realisations before any critical fracture escapes detection. However, this will depend on the random seed. It is theoretically possible, though unlikely, that we get the rare events in the beginning of the simulation sequence by chance. While the effect of the choice of random seed does not significantly affect the number of FPI (Figure 5-12a and Figure 5-12b) it does very much indeed affect the fraction of critical positions per repository, as shown in Figure 5-13.

Before we realised that the number of realisations was insufficient, we suspected that there could be some logical error in the way the pseudorandom numbers were generated. We first tested a number of random seeds and algorithms for FPI (Figure 5-12). Though there are minor differences in the mean values, the spreads overlap and we therefore concluded that the random seed and/or algorithm for producing random numbers do not affect the simulation results in any significant way. Though the mean number of remaining critical positions differ substantially with random seed (Figure 5-13) the very large spread led us to suspect that the cause of discrepancy between consecutive simulations was an insufficient amount of realisations rather than the random seed.

To find the number of realisations sufficient for obtaining a stable mean number of critical positions, we increased the number of realisation in steps of 2,000 and halted at 10,000 realisations which we subjectively judged sufficient to obtain stable mean values (Figure 5-14). This, however, required ridiculously long simulation times (> 48 hrs/model) which was the main motif for rewriting portions of the codes in C++ (see Section 4.7). Note, however, that though 10,000 realisations were sufficient for the deterministically decaying slip it turned out insufficient for the probabilistic case (see Section 6.2).

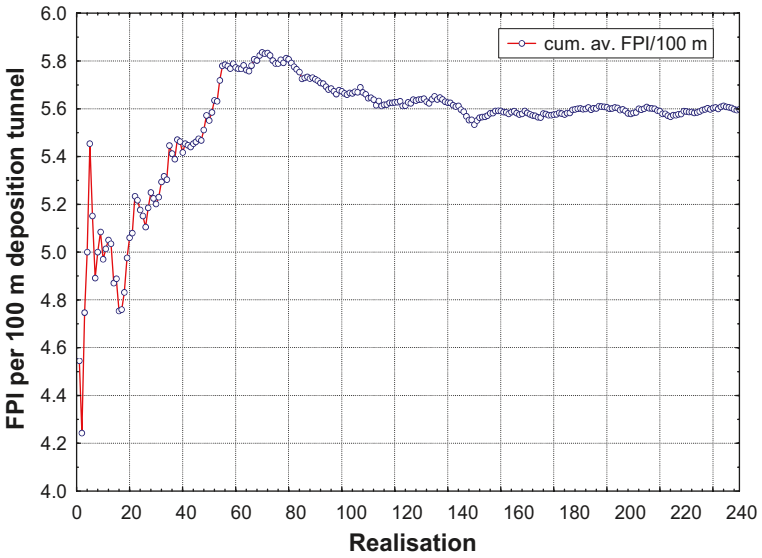

Convergence of simulations in Benchmark analyses.stw
2009-10-13 17:06:09
Include condition: 'Realisation' < 1000

Figure 5-11. *Cumulative average of FPI/100 m for a particular random seed.*

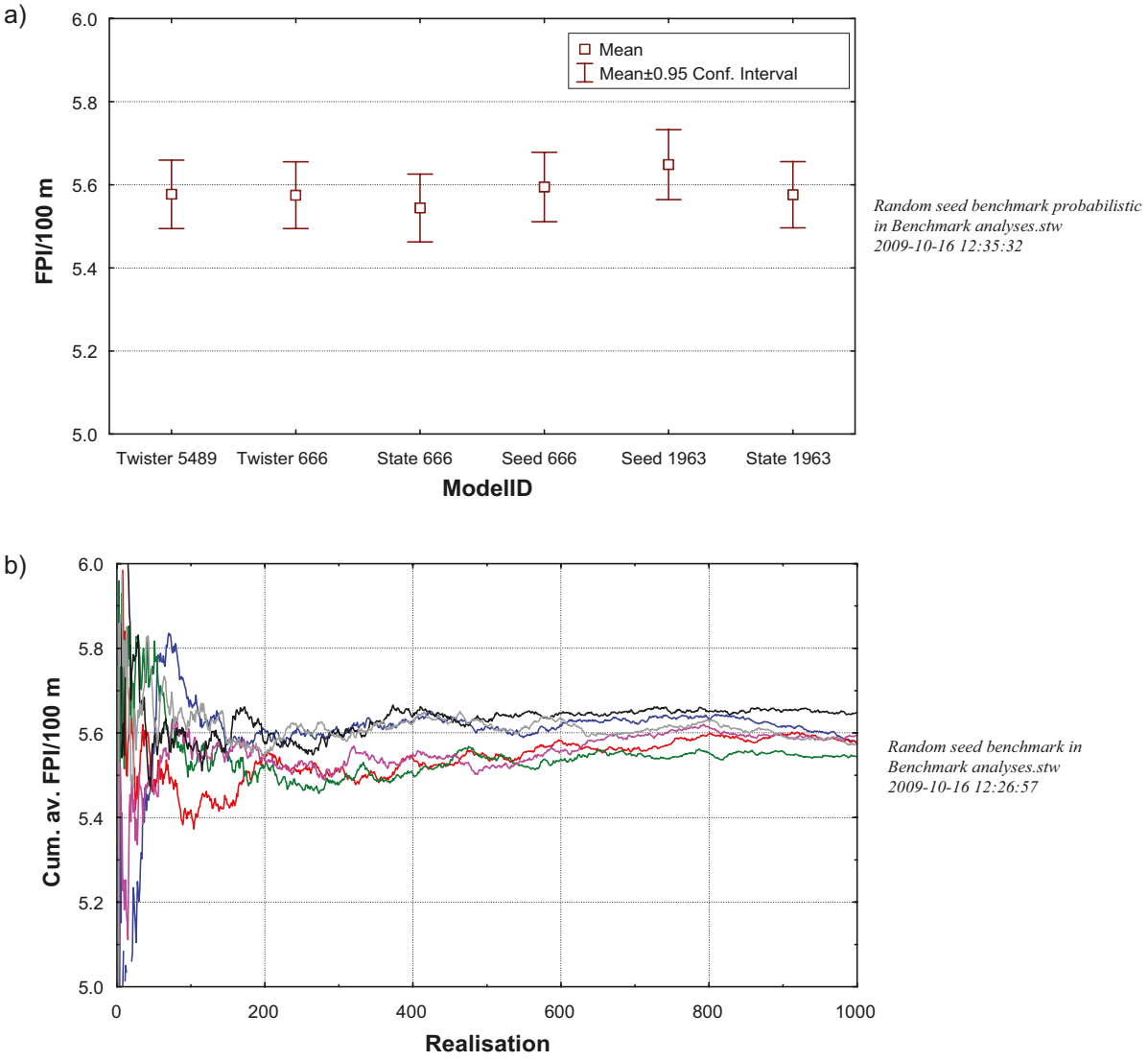

Random seed benchmark probabilistic in Benchmark analyses.stw 2009-10-16 12:35:32

Random seed benchmark in Benchmark analyses.stw 2009-10-16 12:26:57

Figure 5-12. *Effect of assigning different random seeds. In "a" we display mean values with confidence intervals, in "b" we display the cumulative average.*

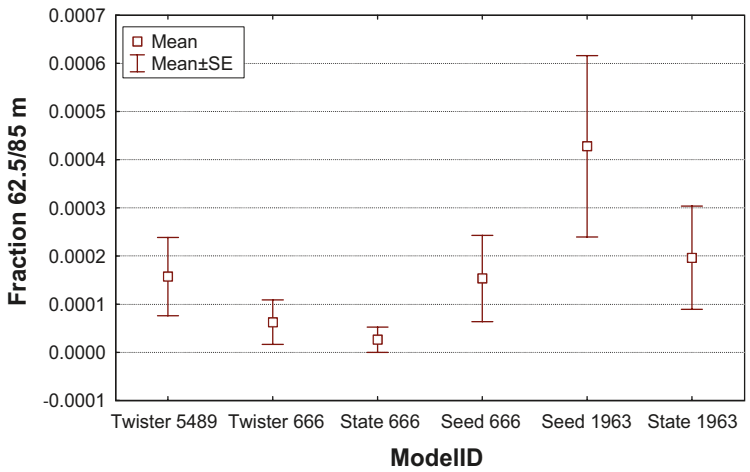

Random seed benchmark probabilistic in Benchmark analyses.stw 2010-01-13 14:27:47

Figure 5-13. *Number of critical positions per repository as a function of random seed.*

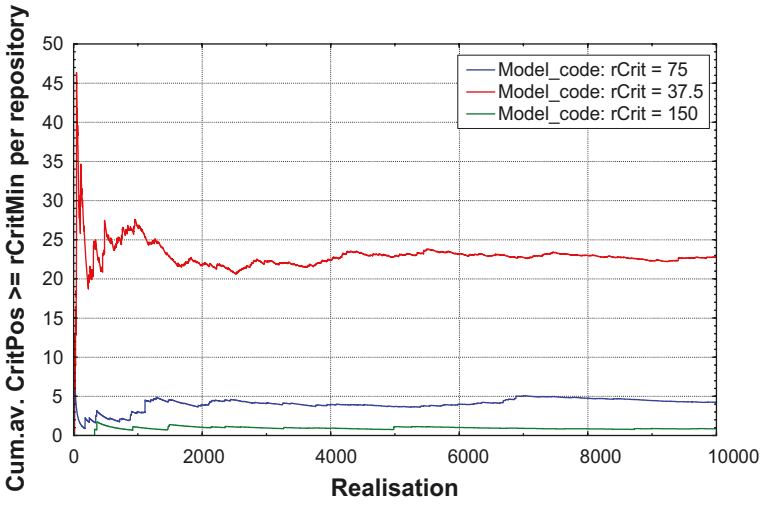

Figure 5-14. *Cumulative average of number of critical positions versus realisation number for different critical fracture radii.*

5.9 Deposition holes and canisters simplified to n-sided prisms

Previous benchmarks have focussed on various aspects of the tunnel/fracture intersections. This benchmark essentially checks if the implementation of deposition holes as n-sided prisms (polyhedra) and deposition hole/fracture collision algorithms are correct (cf Section 4.4.2).

For comparison, we make use of the analytical method by /Hedin 2008/ to compute *"ε"*, which, in short, is the probability of a deposition hole (or canister depending on dimension) being intersected by a fracture exceeding a specified radius.

In the codes, the simulated ε is computed before any other actions are taken, with the exception of filtering (see Section 4.6). That is, neither the fracture network nor the canister positions are affected which enables a direct comparison to the analytical ε. The results of this benchmark are displayed in Figure 5-15 which shows a very good agreement between the simulated epsilon for three different critical fracture radii and of those predicted from the analytical solution. From this we conclude that the implementation of deposition holes as a number of line strings performs as expected and confirm, again, that the fracture array is properly generated.

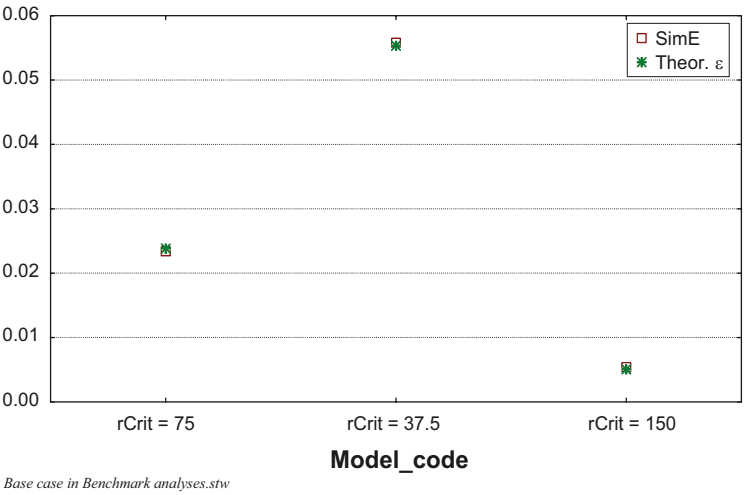

Figure 5-15. *Comparison of simulated and analytical epsilon, base case, 10,000 realisations using different critical radii.*

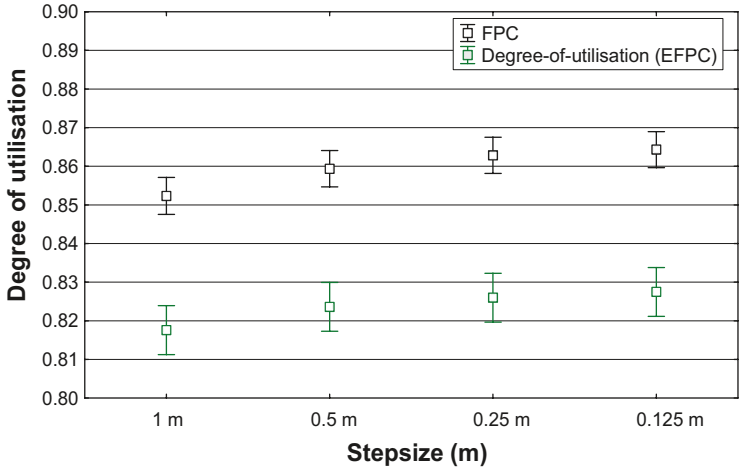

Figure 5-16. *Effect of different step sizes in the FPC criterion upon the degree-of-utilisation.*

5.10 Effect of step-size in FPC

Here, we explore the effect of moving the deposition hole in steps, to avoid fracture intersection, rather than smoothly moving until the fracture no longer intersects (see Section 3.1). The metric that is most obviously affected from this perspective is the degree-of-utilisation (cf Section 3.5). The results (Figure 5-16) show that a decrease in step-size from 1 m to 0.125 m alters the degree of utilisation by roughly 1% in the base case. Yet, in the light of a considerable gain in simulation time, we judge that a step size of 1 m is still adequate for the purpose of our simulations, though we acknowledge it produces a slight underestimation.

5.11 Sensitivity to DFN parameters

In this section, we address the sensitivity of the EFPC method to variations in the properties of the fracture network (DFN model). Though differences in DFN models are handled in the site-specific applications (Chapter 6), we here explore a controlled variation of key DFN parameter to gain further understanding of the intricate interplay between various factors governing the end results.

/Hedin 2005, 2008/ showed, using an analytical solution, that the orientation of the fracture sets had negligible impact on the canister/fracture intersection statistics. Orientation of fracture sets do, however, impact the intersection probabilities with deposition *tunnels*. As the orientation effect is addressed elsewhere in this report, we here neglect the orientation aspects and focus on the size/intensity properties.

Though other size distributions have been reported, such as lognormal, exponential and Gamma, the Powerlaw (Pareto) distribution has been the most successful in describing fracture sizes at the SKB study sites /Darcel et al. 2006, Fox et al. 2007, La Pointe et al. 2008/ which motivated us to restrict the span of the analysis to the Powerlaw. The DFN parameters of concern to this study are thus:

k_r, the shape parameter (slope) of the Powerlaw distribution,

r_0, [m] the location parameter (minimum fracture radius consistent with the DFN model), and

P_{32}, [m^2/m^3] the fracture intensity.

However, it should be noted that r_0 is an unknown quantity which, from all practical purposes, can be regarded as a model parameter. In fact, the choice of location parameter directly steers the fracture intensity, P_{32}, according to equation (18), repeated here for simplicity:

$$P_{32,[r_{\min,new}-r_{\max,new}]} = P_{32,[r_{\min,old}-r_{\max,old}]} \frac{r_{\max,new}^{2-k_r} - r_{\min,new}^{2-k_r}}{r_{\max,old}^{2-k_r} - r_{\min,old}^{2-k_r}}$$

The consequence of decreasing r_0 is an increase of the number of fractures and hence an increase of the total fracture area in the model volume. The consequence of decreasing k_r, the slope of the Powerlaw distribution as plotted on doubly logarithmic scales (Figure 5-17a), is to increase the relative amount of large fractures. The consequence of increasing P_{32} is, by definition, to increase the total fracture area per unit volume (Figure 5-17b).

The parameters of the Site-specific DFN models were computed to simultaneously honour data in boreholes, outcrops and geophysical surveys /see e.g. Fox et al. 2007, La Pointe et al. 2008 for details/. The interdependency of the parameters is, naturally, fairly intricate. The immediate consequence is that, in the strictest sense, it is not possible to e.g. Monte-Carlo sample from ranges of the parameters r_0, k_r and P_{32}, for the purpose of site specific uncertainty/variability assessment, *as they do not constitute truly independent entities.*

Nevertheless, we here judge it feasible to treat the parameters as if they were independent for the purpose of this sensitivity study. It should thus be understood that we use the base case model as a template to construct a set of hypothetical DFN models, judged to encompass a broad range of sizes and intensities combined, for the sole purpose of testing the sensitivity of the FPI criteria.

The DFN models were constructed as follows:

The parameters k_r and P_{32} of the base case (Table 5-1) were independently weighted using the weights [0.8, 0.9, 1.0, 1.1, 1.2] and [5.0, 2.5, 1.0, 0.4, 0.2] for k_r and P_{32} respectively. The lowest and highest weights of k_r were chosen to encompass, what is subjectively perceived, as rather extreme networks. The weights of P_{32} were chosen to produce approximately the same number of fractures as produced using weighted k_r. The adjusted values for k_r and P_{32} are displayed in Table 5-6 and Table 5-7 respectively, in which the weight "1.0" corresponds to the base case DFN.

From Table 5-7 and Table 5-6 it is possible to construct a large number (124) of DFN models, in addition to the base case (weight = 1) by combining k_r and P_{32} for different fracture sets. Due to the immense computation demands, roughly 3–6 hours per model, we restricted the range using weights for P_{32} and keeping k_r fixed to the base case and, similarly, using weights of k_r, using P_{32} of the base case. Additionally, we used the same weight for all fracture sets, to reduce the number of models further. This procedure resulted in 8 DFN models in addition to the base case.

We provide realisation samples of each base model variant in Figure 5-18 to Figure 5-19. The samples represent intersections of circular discs on 50×50 m, horizontal sampling surfaces. The models only included fracture radii larger than or equal to 2.8843 m. Red lines represent *traces* larger than 25 m.

The shape parameter of the power law distribution have the greatest impact upon the number of FPI encountered in a tunnel (Figure 5-20). The consequence of using a smaller k_r is that the proportion of large fractures increases, thereby increasing the intersection probability with the tunnel. This effect is larger than increasing the intensity by a factor of 5. The number of positions that escaped the FPI criteria (Figure 5-21) essentially mimics the pattern on Figure 5-20. Nevertheless, the FPI criteria as a method for detecting potentially critical positions, seems fairly robust; between 90 and 100% of the critical positions were detected, regardless of DFN model (Figure 5-22).

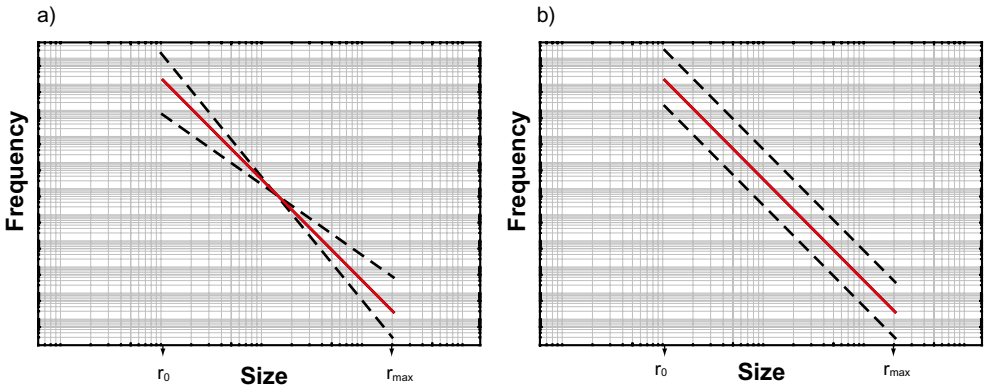

Figure 5-17. *Cartoon illustrating the results of applying weights to a) k_r and b) P_{32}. The consequence of decreasing k_r, the slope of the Powerlaw distribution as plotted on doubly logarithmic scales (a), is to increase the relative amount of large fractures. The consequence of increasing P_{32} is, by definition, to increase the total fracture area per unit volume (b).*

Table 5-6. Weighted k_r values defined by fracture set.

k_r Set#	0.8	0.9	1	1.1	1.2
1	2.174299	2.446086	2.717873	2.989661	3.261448
2	2.195884	2.470369	2.744855	3.01934	3.293826
3	2.085825	2.346554	2.607282	2.86801	3.128738
4	2.063176	2.321073	2.57897	2.836867	3.094764

Table 5-7. Weighted P_{32} values defined by fracture set.

P_{32} Set#	0.2	0.4	1	2.5	5
1	0.346645	0.693291	1.733227	4.333068	8.666136
2	0.258416	0.516832	1.29208	3.2302	6.4604
3	0.189559	0.379118	0.947794	2.369485	4.73897
4	0.124775	0.24955	0.623874	1.559686	3.119372

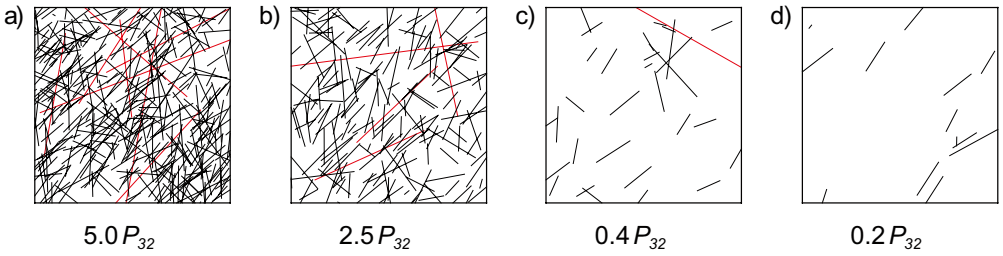

Figure 5-18. *Fracture traces using P_{32}-weighted variants of the base case.*

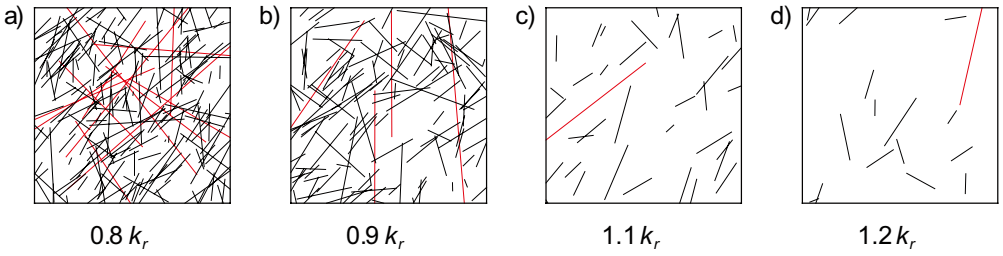

Figure 5-19. *Fracture traces using k_r-weighted variants of the base case.*

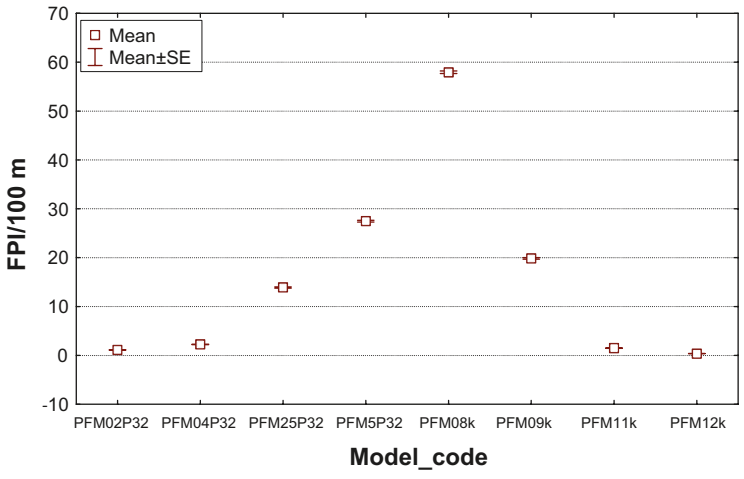

Figure 5-20. *Effect on the number of FPI of using different settings on k_r and P_{32}.*

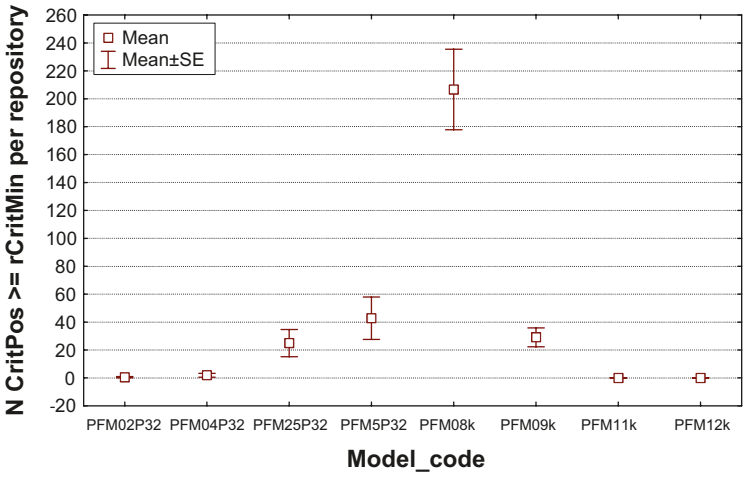

DFN_sensitivity_Large in Benchmark analyses.stw
2009-08-28 12:46:37

Figure 5-21. *Effect on number of critical positions (cut by fractures r ≥ 75 m) of using different settings of kr and P_{32}.*

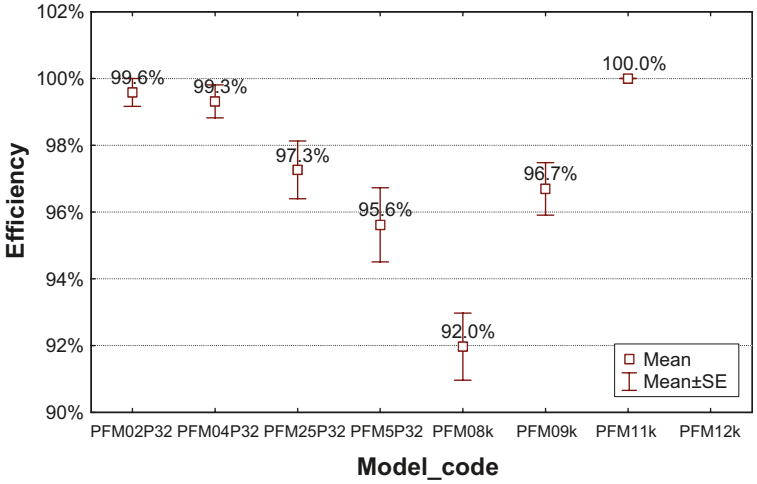

DFN sensitivity in Benchmark analyses.stw
2009-08-31 11:06:22

Figure 5-22. *Effect on efficiency of the EFPC criterion when using different settings of k_r and P_{32}.*

5.12 Effect of varying spacing between canisters

The thermal properties of the rock /e.g. Sundberg et al. 2009/ steer the spacing between canister. In this section, we explore the correlation between canister spacing and various parameters of interest.

The degree-of-utilisation increases with canister spacing as shown on Figure 5-23. The reason is that the minimum fracture radius to consider for the EFPC criterion is larger for larger spacings, according to equation (1) and, naturally, maintaining the same EFPC criterion of five or more intersections. This decreases the conservatism inherent in the EFPC criterion. However, as shown on Figure 5-24, the fraction of critical positions increases with increasing canister spacing thereby confirming, again, that a decrease in risk generally has a "cost" in terms of degree-of-utilisation.

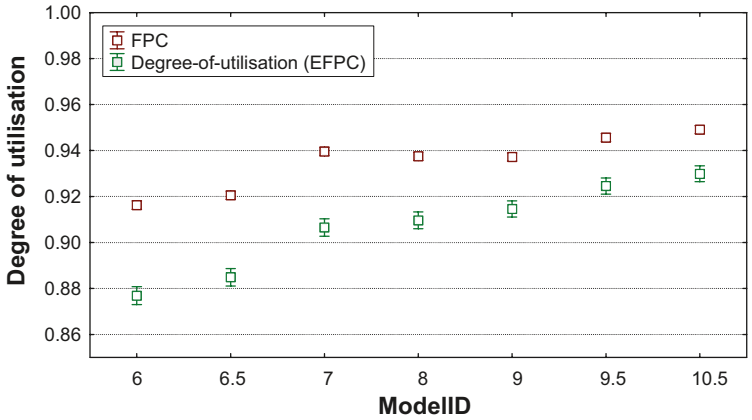

DepHole_Spacing_benchmarks_results, 2009-10-25_232610 in Benchmark analyses.stw
2009-11-05 16:50:48
Exclude condition: ModelID = 407 OR ModelID = 409 OR ModelID = 410

Figure 5-23. *The degree-of-utilisation increases with increasing canister spacing.*

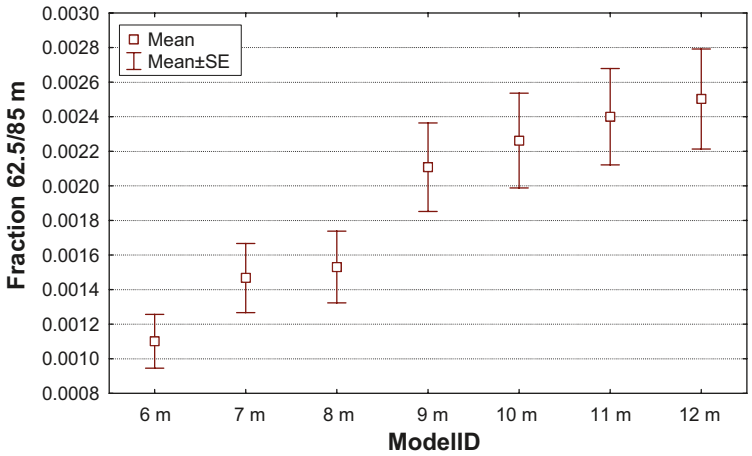

DepHole_Spacing_benchmarks_results in Benchmark analyses.stw
2009-10-21 08:58:20

Figure 5-24. *The fraction of critical canisters increases with increasing canister spacing.*

5.13 Effect of simulation sequence

The simulation logic was chosen such that the fractures (and positions) were systematically stepped through for collision tests, from the first fracture and canister to the last. That is, each canister/deposition hole only "senses" one fracture at the time. Naturally, scrambling the fracture matrix ought to yield identical results but a late discovered logical flaw in the simulation codes rendered a slight overestimation (but not the opposite) of the number of critical positions; there are situations, as illustrated in Figure 5-25, in which the fracture sequence can steer the outcome.

We analysed the simulation output and could only identify a couple of realisations (out of tens of thousands) in which this situation occurred which affected less than a handful of canisters. As the overestimation is minute, and drowned in the overall uncertainties, we regard this effect as insignificant and not worth the effort of correcting the codes accordingly.

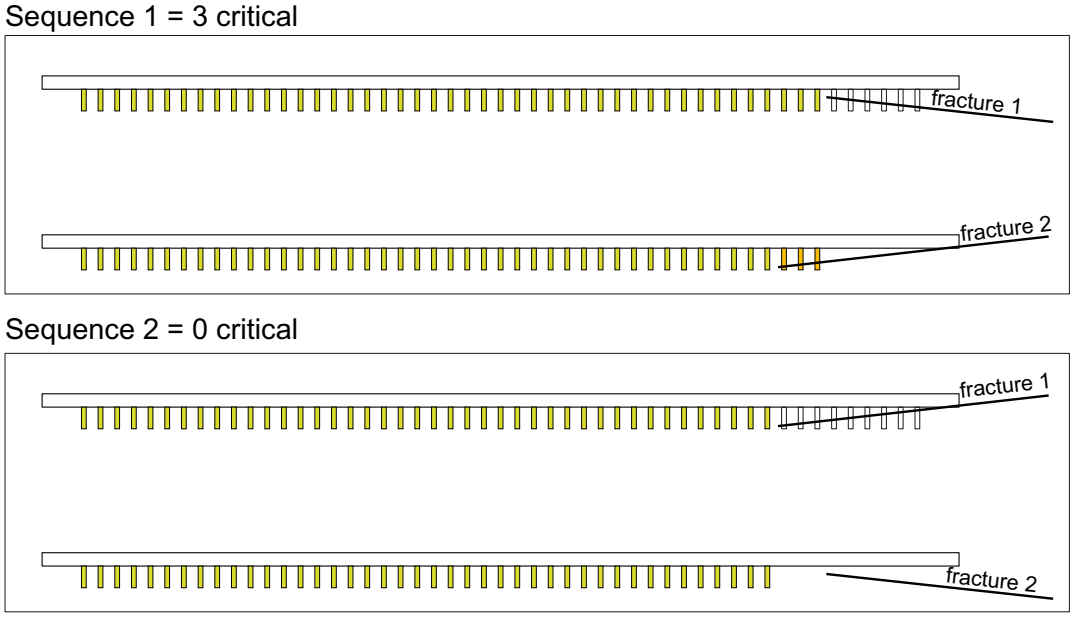

Figure 5-25. *The number of critical position might depend on the simulation sequence. The top sequence identifies three positions as critical whereas the lower sequence results in zero critical positions.*

5.14 Benchmark against independent simulations

/Hedin 2008/ developed a semi-analytic method to compute the intersection between a canister and a fracture. The same code was slightly modified to be able to perform the benchmarks in previous sections. However, the ultimate benchmark is to compute both the degree-of-utilisation and the number of critical canisters, which are, after all, the main output of the efforts of this report, using two entirely independent codes. Therefore, /Hedin 2011/ expanded the work of /Hedin 2008/ to include simulations of degree-of-utilisation and critical canisters.

The result of the comparison is displayed on Figure 5-26 and Figure 5-27 which show the degree-of-utilisation and the fraction of critical canisters for the probabilistic slip assumption. The match between the two simulation approaches is not perfect; The method of Hedin displays a somewhat larger span between FPC and EFPC than the method presented in this report. Also, the level of FPC is slightly higher and the level of EFPC is slightly lower using the method of Hedin. On the other hand, these differences seems to cancel out when it comes to the fraction of critical canisters. As shown on Figure 5-27, the differences between the Hedin approach and this work are minute.

It should be noted that the simulation procedures are not identical and these differences account for some of the differences in the results. For instance, the approach of Hedin utilises a circular tunnel section (radius = 2.8843 m) whereas the approach in this work utilises a drill-and-blast cross-section which results in slightly different number of FPI (and hence FPC, EFPC, etc, see Section 5.4.8). Also, the simulations of this report, utilises a tunnel length of, in the base case, 330 m that exactly fits 51 deposition holes. The slightest adjustment of any position, to avoid FPI fractures, would immediately result in loss of an entire position. This effect is estimated to produce about 1% lower degree-of-utilisation than the one resulting from Hedin's simulations.

Considering the overall uncertainties, we find the results sufficiently similar to conclude that codes herein behave as expected and produce results sufficiently reliable to be used in the Safety assessment SR-Site.

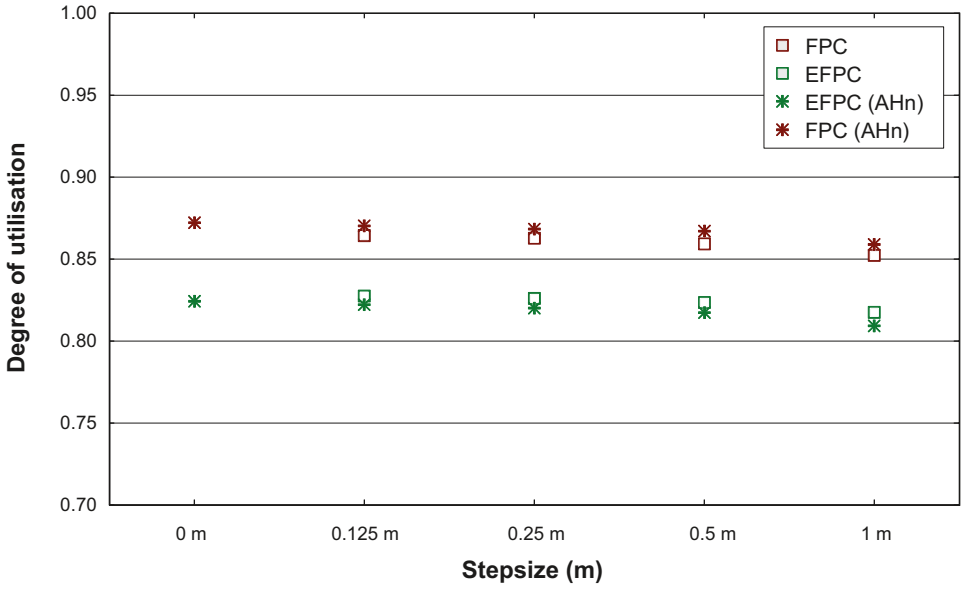

Degree-of-utilisation (Stepsize) in SR_SITE_V1.stw
2009-11-25 09:47:09

Figure 5-26. *Comparison of simulations of degree-of-utilisation by /Hedin 2011/ (stars) and this report (squares).*

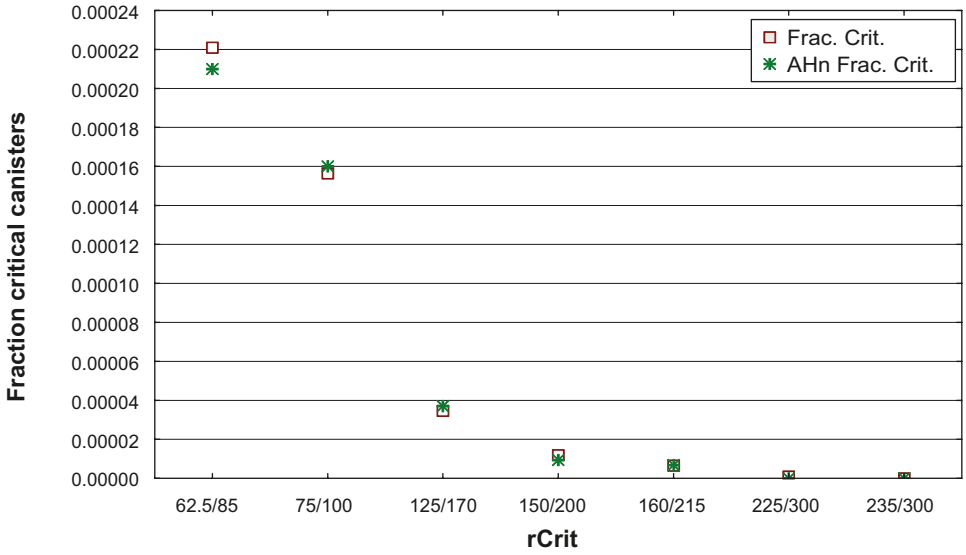

Probabilistic slip in SR_SITE_V1.stw
2009-11-23 16:58:46

Figure 5-27. *Comparison of simulations of fraction critical canisters by /Hedin 2011/ (stars) and this report (squares).*

6 Effect of varying rejection criteria

Whereas Chapter 4 focused on testing the codes from various standpoints, this chapter explores the effect of toggling various simulations options and assumptions regarding the FPI criteria.

6.1 Changing FPC criterion

During the course of work, we experimented with a variety of FPC, the results of which are presented in this section. Figure 6-1 illustrates schematically the criteria which in addition to “a” and “b” discussed in Section 3.1 include two criteria “c” and “d”. In criteria “c” the FPI generating fracture is not allowed to intersect any portion of the deposition hole. Unlike “a” which is based on the *extrapolation* of the FPI fracture, criterion “c” essentially requires drilling a deposition hole to check for an intersection. Criteria “d” is similar to “c”, with the difference that the fracture should not intersect a probe hole drilled in the centre of the planned deposition hole.

The effect upon the degree-of-utilisation is illustrated in Figure 6-2. Criteria “b” (the base case) and “d” render the highest degree of utilisation and are therefore favoured. The number of critical positions is also indicated to be lower but the 250 realisations used is, from a strictly statistical point of view, insufficient for formal comparison of critical positions.

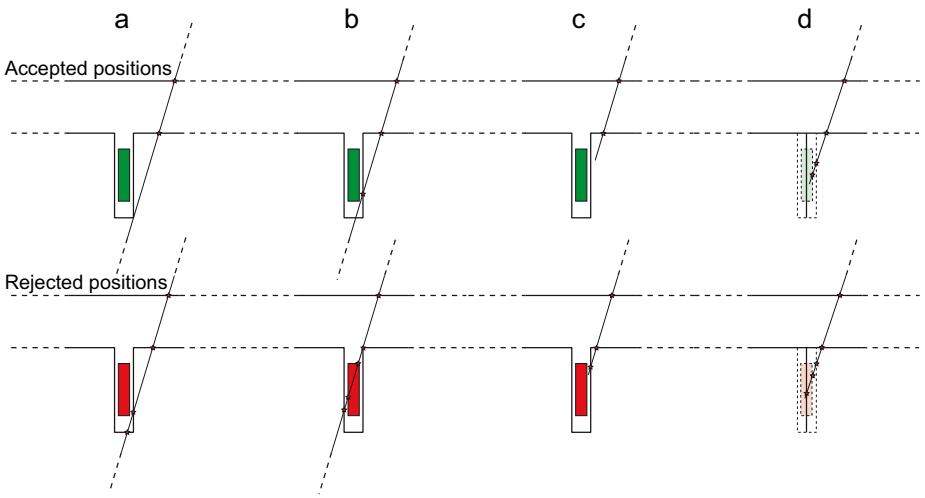

Figure 6-1. *Effect on acceptance when using different FPC a–d. Top row illustrate accepted positions whereas the bottom row illustrates positions that would be rejected under the FPC criteria.*

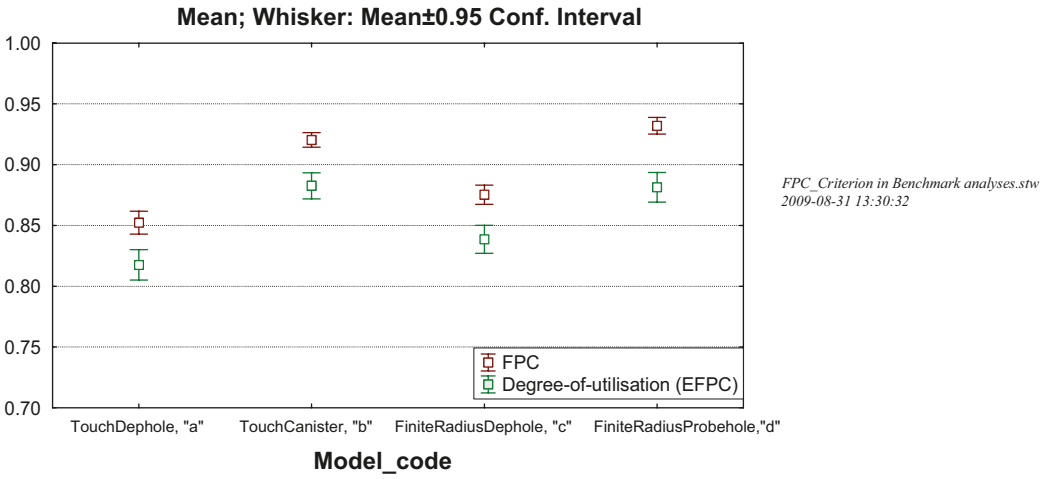

Figure 6-2. *Degree-of-utilisation using different FPC criteria.*

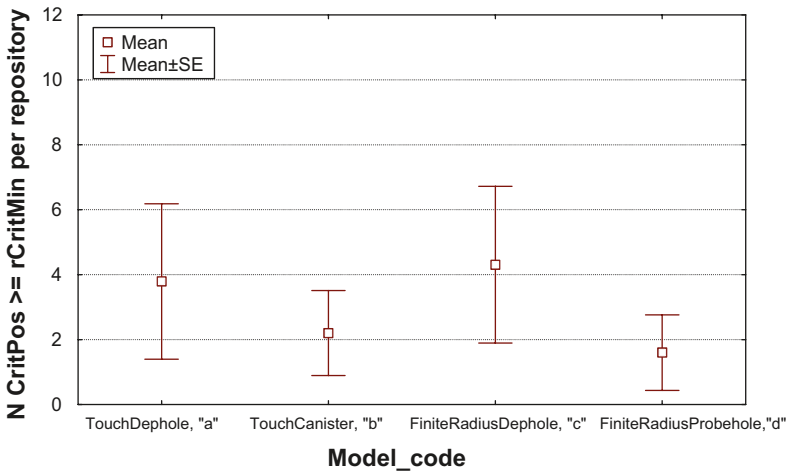

FPC_Criterion in Benchmark analyses.stw
2009-08-31 13:56:40

Figure 6-3. *Number of critical positions using different criteria.*

6.2 Number of positions used for EFPC criterion

The EFPC criterion as suggested states that if 5 or more deposition holes are fully intersected by the same fracture, the intersected positions should be rejected. A more cautious criterion, using fewer intersections, will tend to decrease the degree-of-utilisation as shown on Figure 6-4. As the number of required intersections for the criterion to be fulfilled increases, the degree-of-utilisation asymptotically approaches the one of using FPC alone because it will be increasingly harder to meet the EFPC criterion. Naturally, the more cautious the criterion, the less critical positions remains after having applied the criterion, as shown on Figure 6-5. Thus the efficiency of the EFPC criterion to detect critical fractures is balanced by the degree-of-utilisation.

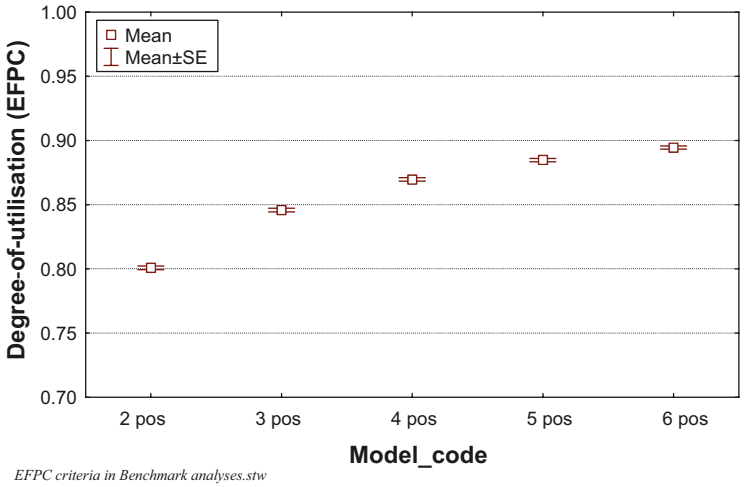

EFPC criteria in Benchmark analyses.stw
2009-08-28 09:23:26

Figure 6-4. *Effect of EFPC criterion upon the degree-of-utilisation (base case, 5,000 realisations).*

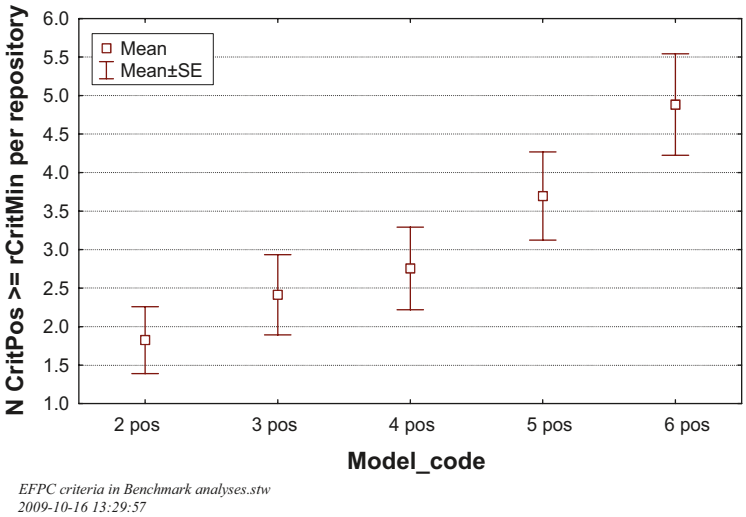

Figure 6-5. *Effect of EFPC criterion upon the number of critical positions (base case, 5,000 realisations).*

6.3 Effect of using varying slip along target fracture

For a linearly elastic medium, the displacement profile along a fracture of radius r varies from d_{max} at the center ($r' = 0$) to zero at the fracture tip ($r' = r$) according to /Eshelby 1957/:

$$\frac{d_{r'}}{d_{\max}} = \sqrt{1-\left(\frac{r'}{r}\right)^2} \qquad \text{Eq. (27)}$$

This means that d_{crit} occurs at a distance r'_{crit} given by (see Figure 6-6a for illustration):

$$r'_{crit} = r\sqrt{1-\left(\frac{d_{crit}}{d_{\max}}\right)^2} = r\sqrt{1-\left(\frac{r_{\min}}{r}\right)^2} = \sqrt{r^2 - r_{\min}^2} \quad r > r_{\min} \qquad \text{Eq. (28)}$$

In the simulations of the base case we have assumed that fractures with radii larger than rCritMin = 75 m are able to host slip exceeding the canister failure criterion. To exploit the effect of taking varying slip along a fracture into account, we rescaled all fractures ($r \geq$ rCritMin) of the

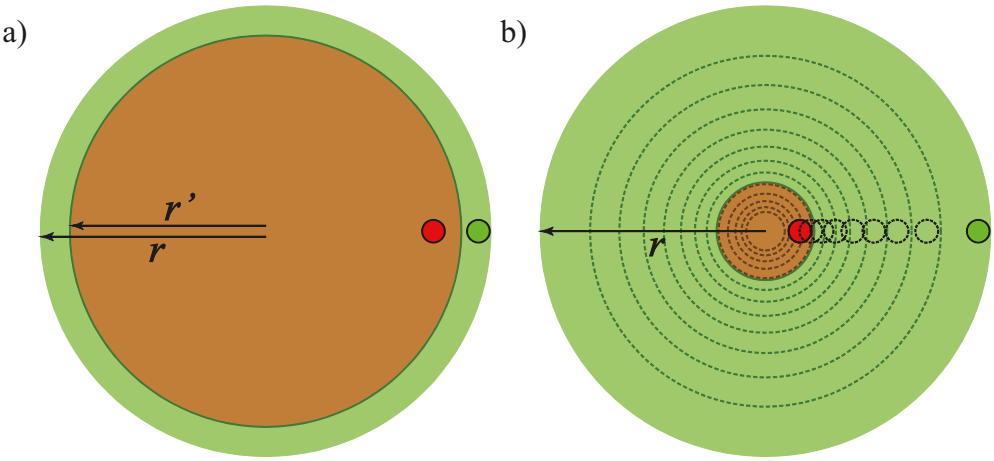

Figure 6-6. *The integrity of a canister (top view) is regarded jeopardised only if it is positioned within the critical radius of the fracture; a) = "deterministic", b) = "probabilistic".*

base case according to Eq. (28), after having applied the EFPC criterion. That is, only the part of the fracture that can host a slip exceeding the canister failure criterion is counted when summing positions that escaped the criteria. The implication is the following: Even if a deposition hole is intersected by a critical fracture, the integrity of the canister will not be jeopardised as long as the intersection point is not too close to the centre of the fracture were the slip is the largest.

The decrease in the number of critical positions escaping detection is dramatic if the decaying slip option is chosen, as shown on Figure 6-7, but less pronounced as the minimum critical radius (rCritMin) increases.

Though linear or parabolic decay of slip towards the fracture tip is supported by field observations /Muraoka and Kamata 1983, Walsh and Watterson 1989/ we acknowledge the observations that the maximum slip is rarely positioned at the centre of *earthquakes* /e.g. Kim and Sanderson 2005/ which, as far as we know, are the only equivalents to the problem at hand. Yet, with no further argument, we simply claim that the idealisation of maximum displacement at the centre of the target fractures is consistent to the idealisation of fracture as infinitely thin, perfectly circular discs and should, *on average*, be sufficiently close to what we would expect in nature as to motivate its use in these simulations.

The simulation results of /Fälth et al. 2010/ indicate that only a few fractures able to host critical slip magnitudes actually do so, due to differences in their orientation and location relative to the hypocentre and to the fault tip. If we take full account for the results and recommendations of /Fälth et al. 2010/ we may express a "probabilistic" decay of slip towards the fracture tip by (see also Figure 6-6b for illustration):

$$r'_{Crit} = \sqrt{r^2 - \frac{1}{p^2} r_{Min}^2}, \quad r > \frac{r_{Min}}{p} \qquad \text{Eq. (29)}$$

where p is a uniform distribution on [0,1].

An average value of r r'_{Crit} for a fixed fracture radius r can be derived /Hedin 2011/:

$$\overline{r'_{Crit}} = \sqrt{r^2 + r_{Min}^2 - 2 r r_{Min}} \qquad \text{Eq. (30)}$$

which, essentially, replaces Eq. (28) for simulation cases using probabilistically decaying slip.

The effect of implementing a probabilistically decaying slip is dramatic (Figure 6-8); the fraction of canisters intersected by discriminating fractures decreases by about a factor four.

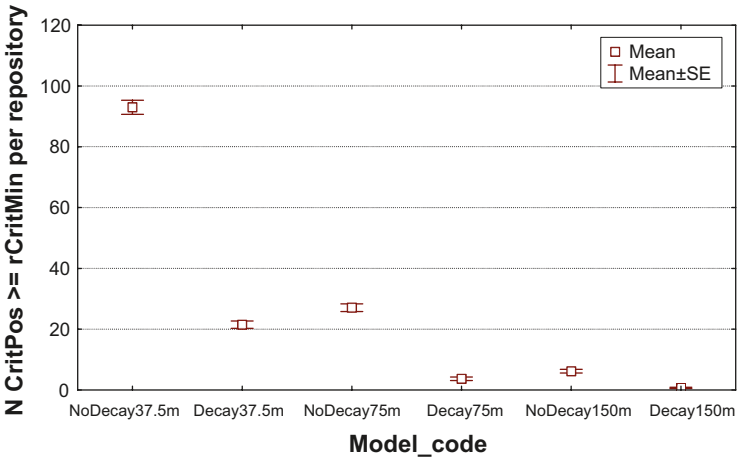

Decaying slip in Benchmark analyses.stw
2009-08-27 16:55:29
Exclude condition: Model_code = 'SkipDecaying'

Figure 6-7. *The graph shows that if account is taken for decaying slip towards the fracture tip, the number of undetected critical positions decreases dramatically.*

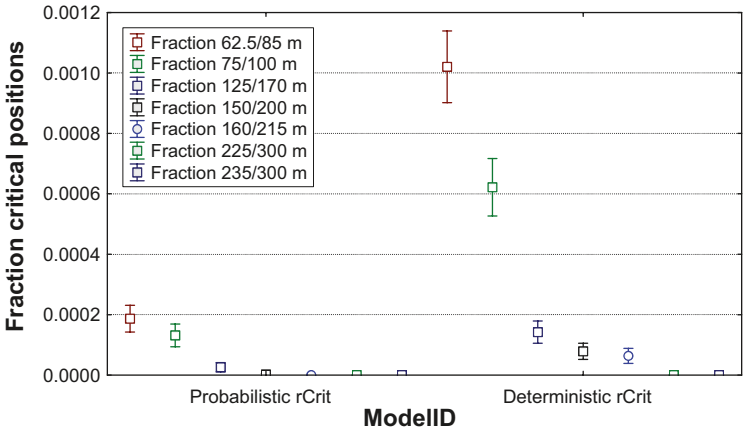

Figure 6-8. *Comparison of the fraction of canisters intersected by discriminating fractures assuming deterministic and probabilistic slip respectively, for various critical radii.*

6.4 Using neighbouring tunnels

In the base case, the simulations regard only one tunnel at the time, neglecting any other information from neighbouring tunnels. Naturally, in a repository there will be possibilities to trace a large fracture across several tunnels by either direct (e.g. mapping) or indirect (e.g. radar) methods.

In Figure 6-9 we show a realisation which rendered 2 critical positions. If this particular fracture could have been traced also in the neighbouring tunnel(s), the fracture would have been regarded discriminating and the positions would probably have been rejected. Figure 6-11 shows that, for the base case, the number of critical positions can be reduced by roughly half, if information from neighbouring tunnels can be used. Yet the consequence, in terms of degree-of-utilisation is negligible; A couple of deposition holes more or less do not in any practical way affect the degree-of-utilisation. Figure 6-10 shows all positions that remain critical after having run 25,000 realisations of the base case. Critical positions can occur anywhere in the tunnel but, as the (kernel) density contour show, most of the critical positions are located at the end of the tunnels.

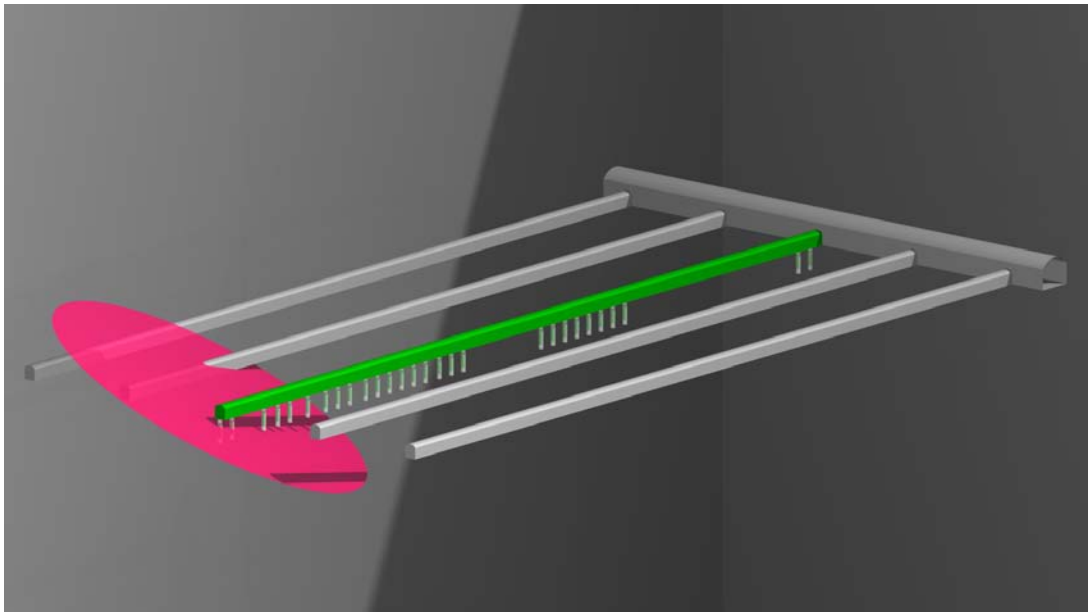

Figure 6-9. *Example of a realisation in which a large fracture escaped detection.*

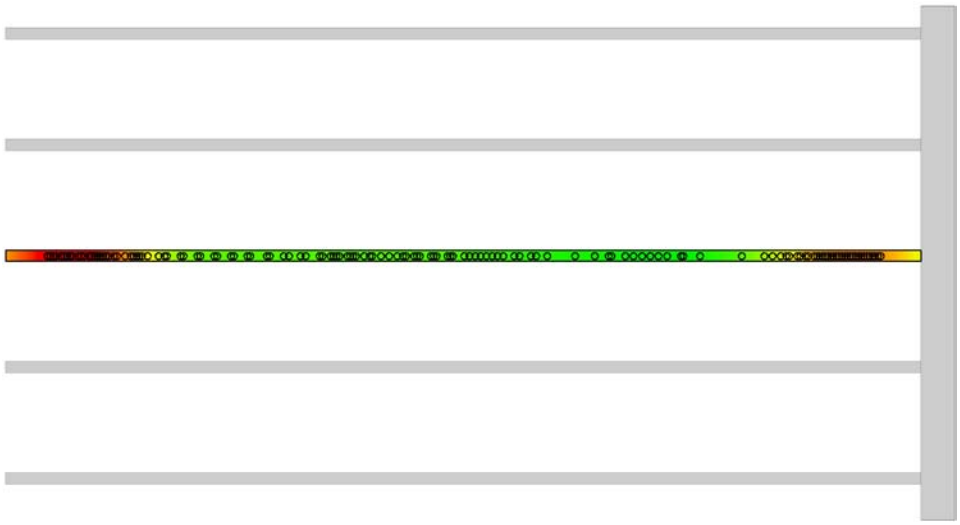

Figure 6-10. *The figure shows critical positions after having run 25,000 realisations (i.e. deposition tunnels) of the Forsmark base case, using minimum critical radii = 62.5 m. The (kernel) density shading highlights the concentration to tunnel ends.*

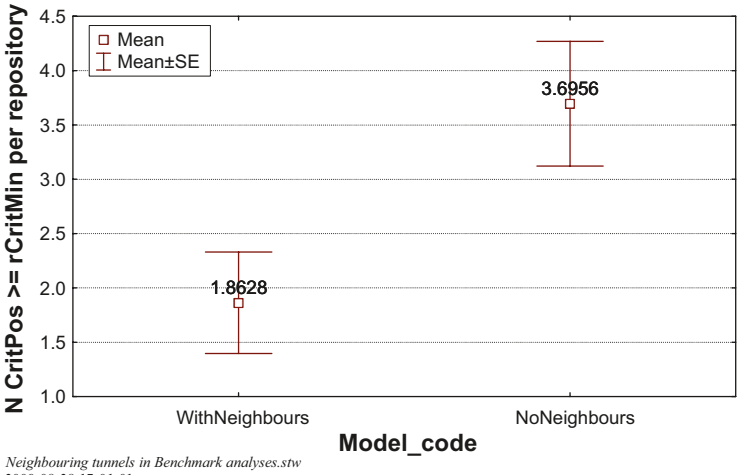

Figure 6-11. *Number of critical positions can be decreased if information from neighbouring tunnels can be used.*

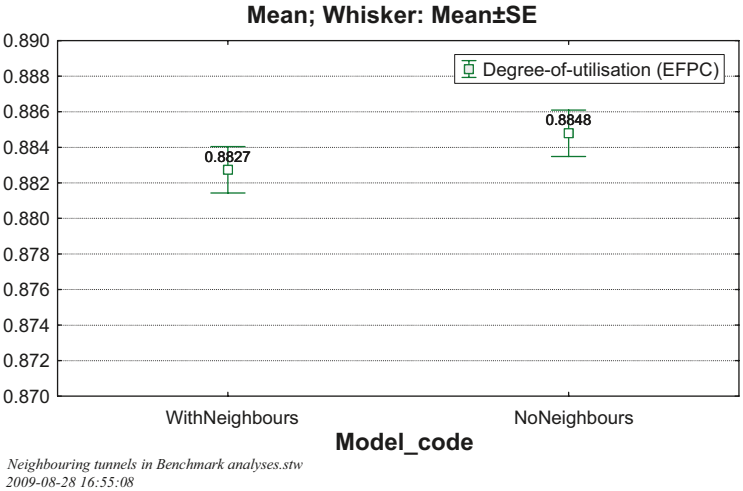

Figure 6-12. *The degree of utilisation is hardly affected by observations in neighbouring tunnels.*

6.5 Effect of requirement of FPI for EFPC

The EFPC criterion, as currently stated, requires the fracture to cut through 5 or more deposition holes to be regarded critical. In terms of simulation, this means that the fracture must create full perimeter intersections in the deposition holes.

It is hard to argue that intersections of other types than “a” or “b” (Figure 4-1) could be readily detected in the deposition holes. This would imply that we could, somehow, measure the fractures which would render the EFPC criterion obsolete (see also Section 6.6). We therefore believe it is reasonable to require FPI in the deposition holes for the EFPC criterion to be fulfilled.

However, this has a drawback. There are, very few, “pathological” realisations that marked positions as critical whereas such position would most certainly be detected in a live situation. We show such an example in Figure 6-13. In this particular realisation, 9 consecutive positions were marked critical. The reason is that only two of these produced FPI when intersecting the critical fracture and, accordingly, the EFPC criterion requiring 5 (FPI) intersections or more was not fulfilled.

It is difficult to implement a simulation logic that would, somehow, detect a situation like this and we doubt it would be worth the effort invested. These are indeed rare events and we simply acknowledge that, though on the cautious side, this effect has no practical significance whatsoever.

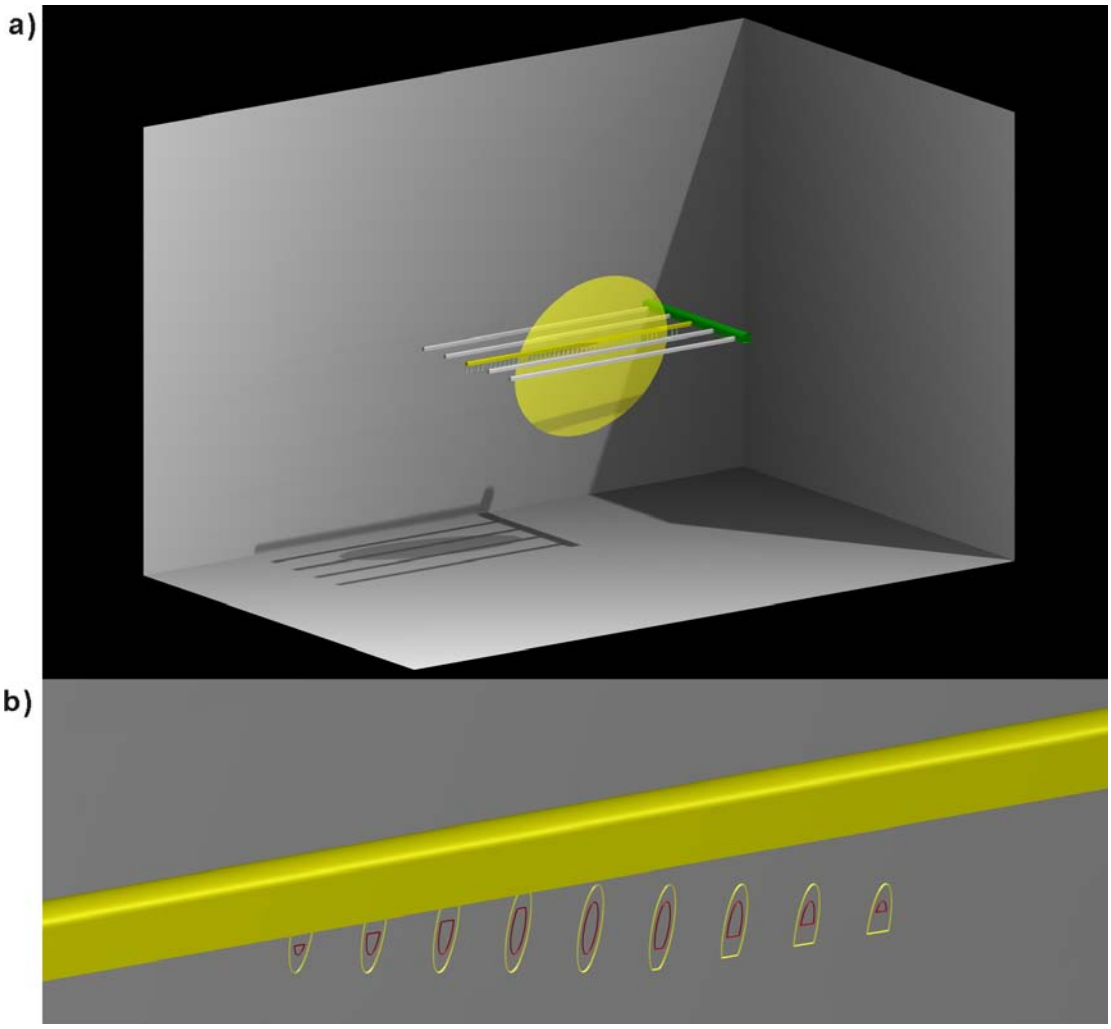

Figure 6-13. *Case showing a fracture striking subparalell to a tunnel (figure “a”), marking 9 positions as critical (figure “b”). In “b”, red lines represent intersection traces with the canister whereas yellow lines represent intersection traces with the deposition hole.*

6.6 If fracture sizes can be measured

The main motif for introducing the FPI criteria, is that it has traditionally been notoriously difficult to measure fracture sizes. When interpreting simulation results, we assume (in the base case) that we have no means whatsoever other than visual inspection (i.e. traditional geological mapping) to detect potentially hazardous structures (cf 6.5). This is not only overly conservative, it is also entirely, and unnecessarily, neglecting the advances in mining engineering. Certainly, we possess, and have made documented use of, an array of tools (such as radar) to aid identifying structures, or parts thereof. The problem has been to *quantify* the extent of which such methods are successful /Cosgrove et al. 2006/.

In this section we hypothesise over the consequences of finding support on the size assessment by some unspecified method assuming either that the sizes of FPI- or both FPI- and EFPC-fractures can be determined with varying probability.

a)

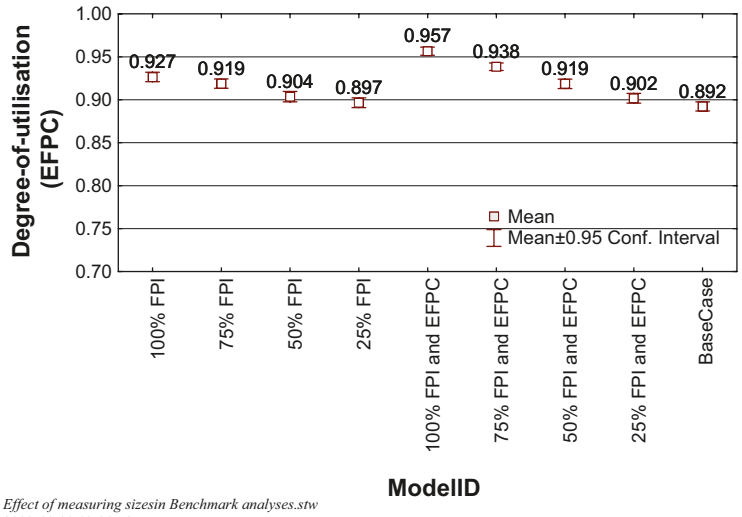

Effect of measuring sizesin Benchmark analyses.stw
2009-11-09 10:01:48

b)

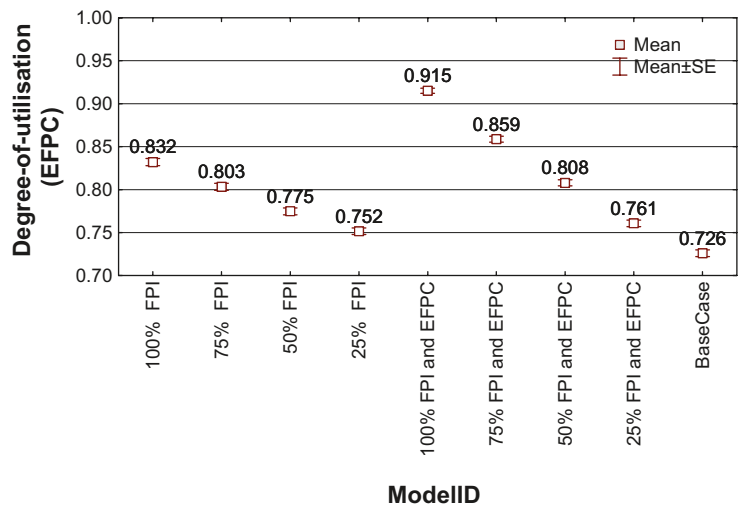

_IfYouCanMeasureFPIfracs_TCM in Benchmark analyses.stw
2009-11-08 18:15:00

Figure 6-14. *The degree-of-utilisation can be improved by measuring fracture size. Here, we show the gain in degree-of-utilisation as a function of the relative amount of fractures that could be successfully measured. Figure"a" shows results using the base case DFN model whereas Figure "b" shows results for the TCM model.*

The results (Figure 6-14) quantify the gain in the degree-of-utilisation that can be expected if the minimum size of a fracture can be measured to some extent. But there is an upper limit for the degree-of-utilisation which should be regarded as a DFN-specific theoretical maximum; That is, even if we somehow could measure the size of all fractures, there will, naturally, be a number of canister positions that need to be rejected due to real intersection with truly large fractures.

Whether or not it is worth pursuing a detailed investigation campaign to measure the fracture sizes, will depend on the level of degree-of-utilisation if no measurement are made. For the base case shown in Figure 6-14a the gain in degree-of-utilisation is maximum of ≈ 6%, assuming both FPI and EFPC fractures can be measured, or maximum of ≈ 4%, assuming only FPI fractures can be measured, which, considering all other factors that contribute to the degree-of-utilisation, is not so dramatic. However, more dense fracture networks would gain more by a measuring campaign. For instance, should Forsmark be best represented by the TCM model (see Section 7 and /Fox et al. 2007/ for details), the gain would amount to almost 20% (Figure 6-14b).

7 Site-specific simulations

In this chapter, we use site-specific DFN models[6],[7] to compute the number of canisters that are intersected by critical fractures (see also Appendix 2). The deformation zone models[8],[9] are used, together with repository layouts /SKB 2009b/, to compute the critical fracture radius for each position, using results from the earthquake simulations of /Fälth et al. 2010/.

7.1 Prerequisites

In this section, we list the modelling prerequisites and assumptions. The site specific prerequisites are given in Table 7-1. The general modelling prerequisites are:

- Only one deposition tunnel is used in each realisation. Knowledge of eventual intersections from neighbouring tunnels is thus ignored.
- Drill and blast tunnel profiles are used as the base case. The exact dimensions used in the simulations are given in the Figure 7-1.
- The tunnel length was set to 330 m, which includes two 15 m empty sections at each tunnel end (see Section 4.4.3).
- The decaying slip option (see Section 6.2) was enabled, using the probabilistic formula (equation 30).
- The minimum fracture radii varies with distance to deformation zones, size of deformation zones and dip of target fracture according to /Fälth et al. 2010/, see Table 7-2. Each canister position in the layout is then tagged with a pair of critical radii, depending on distance to deformation zones.
- Any intersection (a–h, Figure 4-1) of the canister (criterion "b" in Figure 3-1) counts for FPC to be fulfilled.
- The EFPC criterion was set to 5 or more intersections. An FPI was required in the deposition hole to count as a qualified intersection.

[6] /Modelldatabasen 2007/. Model: PFM DFN 2.2.xls. Version 0.6. Approved 2007-11-29, Modeller: A. Fox. Simon ID: GEO_WTAGLLAA. https://service.projectplace.com/pp/pp.cgi/r232241793 (access might be given on request).

[7] /Modelldatabasen 2008/. Model: DFN LAX v2.3 (site).xls. Version 0.5. Approved 2008-08-19, Modeller: A. Fox. Simon ID: GEO_HXXZNQSH. https://service.projectplace.com/pp/pp.cgi/r241528007 (access might be given on request).

[8] / Modelldatabasen 2007/. Model: DZ_PFM_REG_v22.rvs. Version 0.3. Approved 2007-08-31, Modeller: A. Simeonov. Simon ID: GEO_IZTKKYIL. https://service.projectplace.com/pp/pp.cgi/r180716254 (access might be given on request).

[9] /Modelldatabasen 2008/. Model: DZ_LX_REG_v23.rvs. Version 0.1. Approved 2008-05-27, Modeller: P. Curtis. Simon ID: GEO_UNYMTLYA. https://service.projectplace.com/pp/pp.cgi/r272436908 (access might be given on request).

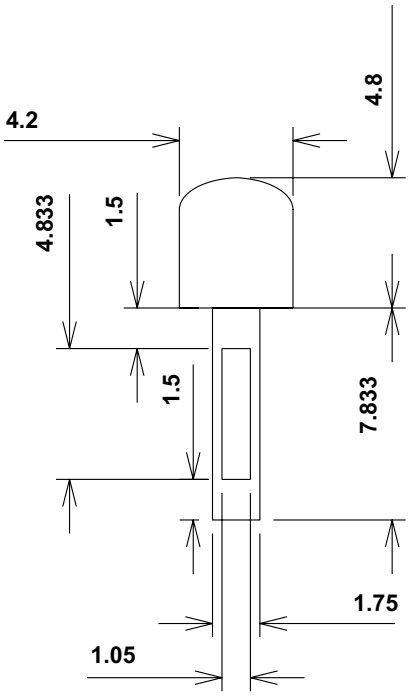

Figure 7-1. Dimensions in metres, of different tunnel parts used in the simulations.

Table 7-1. Site-specific modelling prerequisites.

	Forsmark	Laxemar
Orientation of deposition tunnels	123° /SKB 2009b/	130° /SKB 2009b/
Rock domains (steers distance between positions)[1,2]	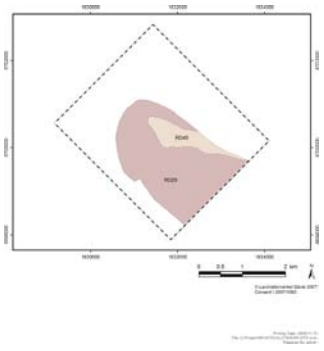	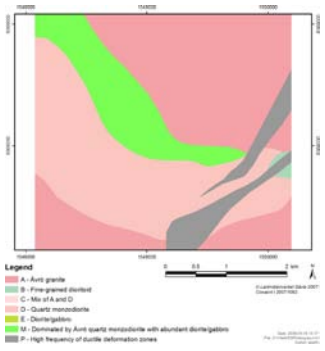
Distance between canister positions	RD 29: 6.0 m RD 45: 6.8 m /SKB 2009b/	RMSD01: 8.1 m RMSM01: 10.5 m RMSA01: 9.0 m /SKB 2009b/
Fracture domain (Steers DFN model)[3,4]	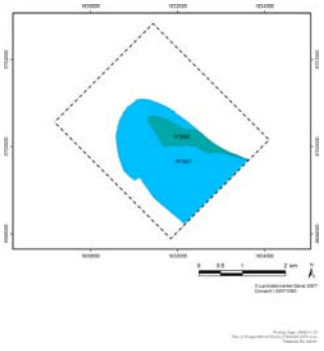	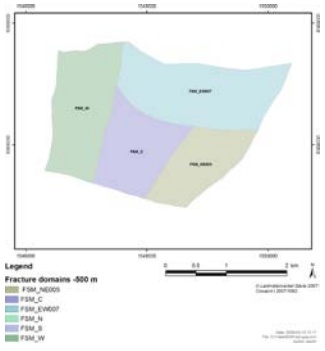

	Forsmark	Laxemar
Deformation zones (Deterministic. Steers layout, critical radii)[5,6]	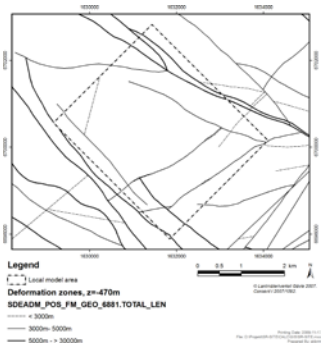	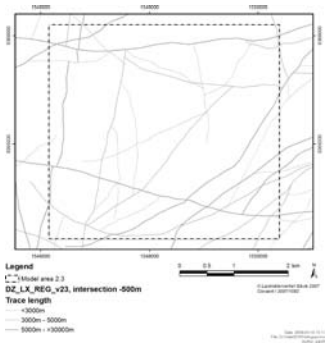
Canister positions	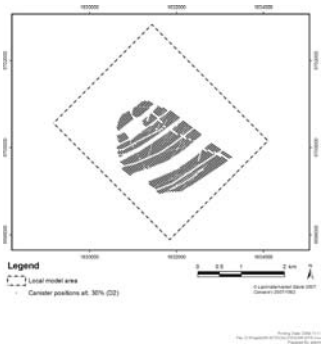	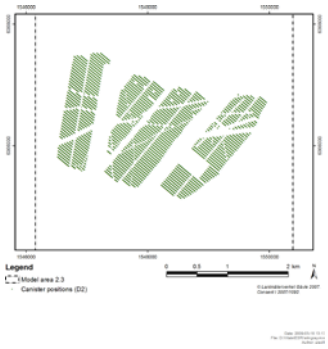

[1] /Modelldatabasen 2007a/. Model: RD_LX_LOC_v23.rvs. Version 0.1. Approved 2007-12-05, Modeller: C.-H. Wahlgren. Simon ID: GEO_XBYFOUEL. https://service.projectplace.com/pp/pp.cgi/r233609993 (access might be given on request).

[2] /Modelldatabasen 2007b/. Model: RD_PFM_Loc_v22.rvs. Version 0.2. Approved 2007-11-29, Modeller: M. Stephens. Simon ID: GEO_ZAIWQGYJ. https://service.projectplace.com/pp/pp.cgi/r180715481 (access might be given on request).

[3] /Modelldatabasen 2007/. Model: FD_PFM_v22.rvs. Version 0.2. Approved 20081022, Modeller: A. Simeonov. Simon ID: GEO_AJIYBKOY. https://service.projectplace.com/pp/pp.cgi/r186999156 (access might be given on request).

[4] /Modelldatabasen 2008/. Model: FD_LX_LOC_V23b.rvs. Version 0.1. Approved 2008-02-10, Modeller: J. Hermanson. Simon ID: GEO_NQLTZVHD. https://service.projectplace.com/pp/pp.cgi/r269498106 (access might be given on request).

[5] /Modelldatabasen 2007/. Model: DZ_PFM_REG_v22.rvs. Version 0.3. Approved 2007-08-31, Modeller: A. Simeonov. Simon ID: GEO_IZTKKYIL. https://service.projectplace.com/pp/pp.cgi/r180716254 (access might be given on request).

[6] /Modelldatabasen 2008/. Model: DZ_LX_REG_v23.rvs. Version 0.1. Approved 2008-05-27, Modeller: P. Curtis. Simon ID: GEO_UNYMTLYA. https://service.projectplace.com/pp/pp.cgi/r272436908 (access might be given on request).

Table 7-2. Correlation between zone trace length, target facture dip, distance from zone and critical target fracture radii (from /Fälth et al. 2010/).

Zone trace length (km)	Target fracture dip (degree)	Distance from zone (m)	Critical target fracture radius (m)
>5	0–55	100–200	62.5
>5	0–55	200–400	125
>5	0–55	400–600	160
>5	0–55	>600	225
>5	55–90	100–200	85
>5	55–90	200–400	170
>5	55–90	400–600	215
>5	55–90	>600	>300
3–5	0–55	100–200	75
3–5	0–55	200–400	150
3–5	0–55	400–600	235
3–5	0–55	>600	>300
3–5	55–90	100–200	100
3–5	55–90	200–400	200
3–5	55–90	400–600	>300
3–5	55–90	>600	>>300

7.2 Method

The main output of the simulations is the fraction of critical positions for different pairs of critical radii. However, in order to obtain the number of critical positions, this fraction must be multiplied by the number of positions within particular rock domains, at particular distances from the deformation zones or fracture domains.

We make use of the analysis tools of /ArcMap 2006/ to compute the location of each canister position in relation to the location of deformation zones, fracture domains and rock domains according to the following scheme:

1) First we extract the zones to include in the analysis. There are two factors to consider /Fälth et al. 2010/:
   a. Only zones exceeding 3 km in trace length (or equivalent area for zones not intersecting the surface) are included in the analyses. This is achieved by inspection of the deformation zone map (traces at repository depth).
   b. Only zones within 600 m from any canister position need to be included. This is achieved by constructing a 600 m buffer around the repository, and by computing the intersections between all zones extracted from "a" with this buffer.
2) Zones are categorised in terms of criticality for different stress regimes /Lund et al. 2009, Fälth et al. 2010/. Only zones categorised as critical are included in the analyses. There are two conceptual cases to consider:
   a. Mixed stress regime
   b. Reverse stress slip regime
3) The critical radii are dependent on the size of the deformation zone. Hence, zones obtained from "2" are categorised into the classes:
   a. 3–5 km trace length (or equivalent)
   b. ≥ 5 km trace length (or equivalent)
4) For each zone obtained from "3", we compute 200 m, 400 m, 600 m and > 600 m buffers. Rather than computing these buffer volumes directly in 3D using RVS /"Rock Visualisation System", Curtis et al. 2007/, we join the property sheets of RVS with the 2D deformation zone traces at repository depth (obtained by using the sectioning tool in RVS), and use the dip of the deformation zones to compute the 2D buffers.
5) Using the intersection tools in /ArcMap 2006/, we compute the intersections between canister positions and fracture domains.
6) Using the output from "5", we compute the intersection with rock domains.
7) Finally, for each zone, we compute the intersection between canister positions from "6" with each buffer from "4".

7.3 Results

7.3.1 Forsmark

At Forsmark, seven deformation zone are sufficiently close to any canister position (≤ 600 m) to impose a possible threat to the canister integrity (Figure 7-2). However, two of these zones (ZFMENE060A and ZFMENE062A) are, according to /Fälth et al. 2010/, due to their orientations stable, regardless of anticipated postglacial stress regime, and might therefore be excluded from analyses.

Following the reasoning of /Fälth et al. 2010/, we classified these deformation zones into two size classes, 3–5 km and ≥ 5 km trace length respectively, and into classes defining their stability under reverse or mixed slip regimes (Figure 7-3).

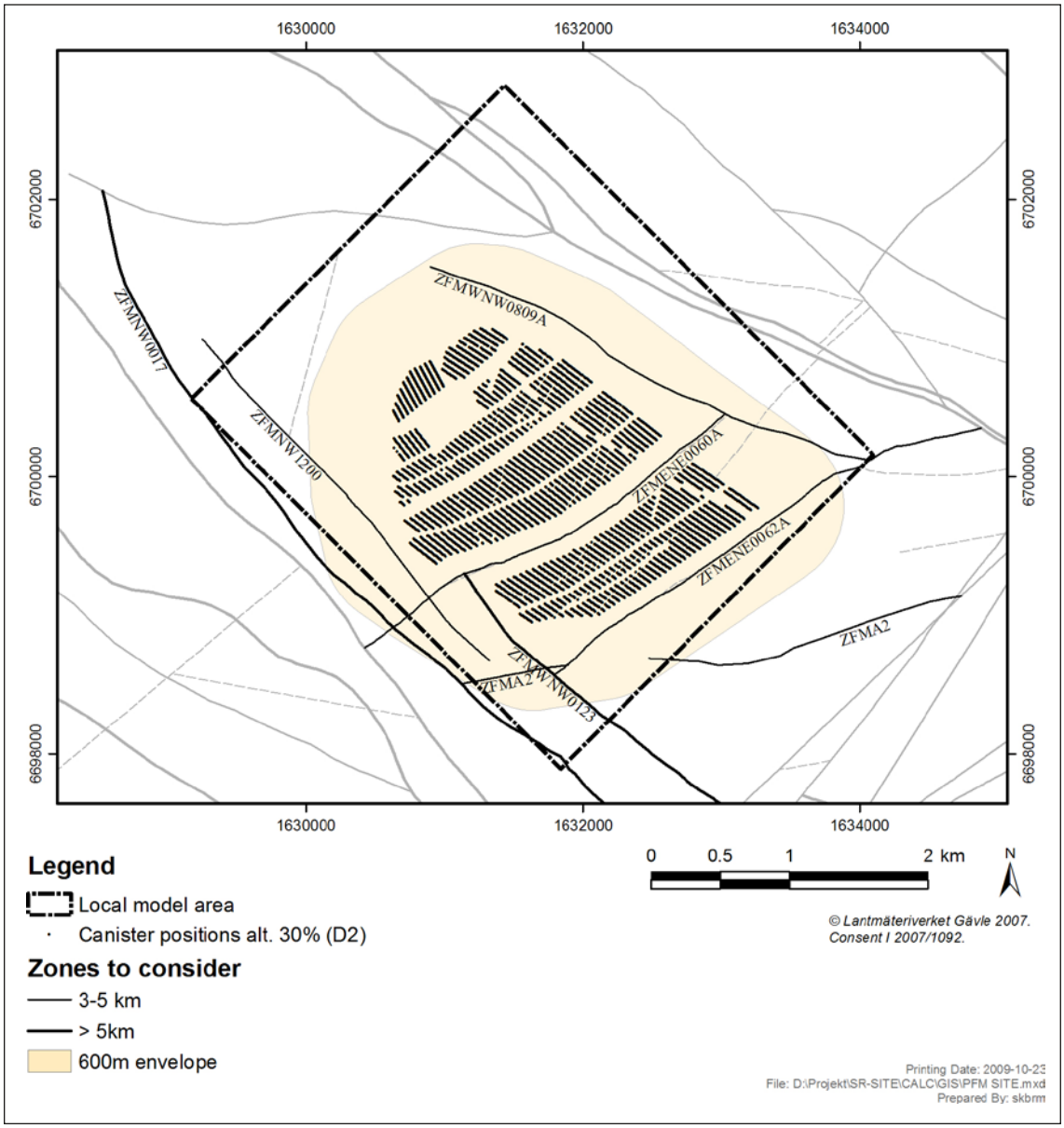

Figure 7-2. *Zones within the 600 m envelope and having traces exceeding 3 km at the Forsmark site.*

For each deformation zone, we constructed buffers, perpendicular to the zones in 3D, at 200, 400 and 600 m from the boundary of the deformation zones, and classified each canister position according to these distances. An example using ZFMWNW0809A is displayed on Figure 7-4. In Table 7-3 we list, using the relations in Table 7-2, the number of canisters that fall into each class, for each fracture domain.

We recall that the rock- and fracture domains at Forsmark have identical geometries at repository depth, which reduces the number of cases to six by combining three alternative DFN models with two canisters spacings.

a)

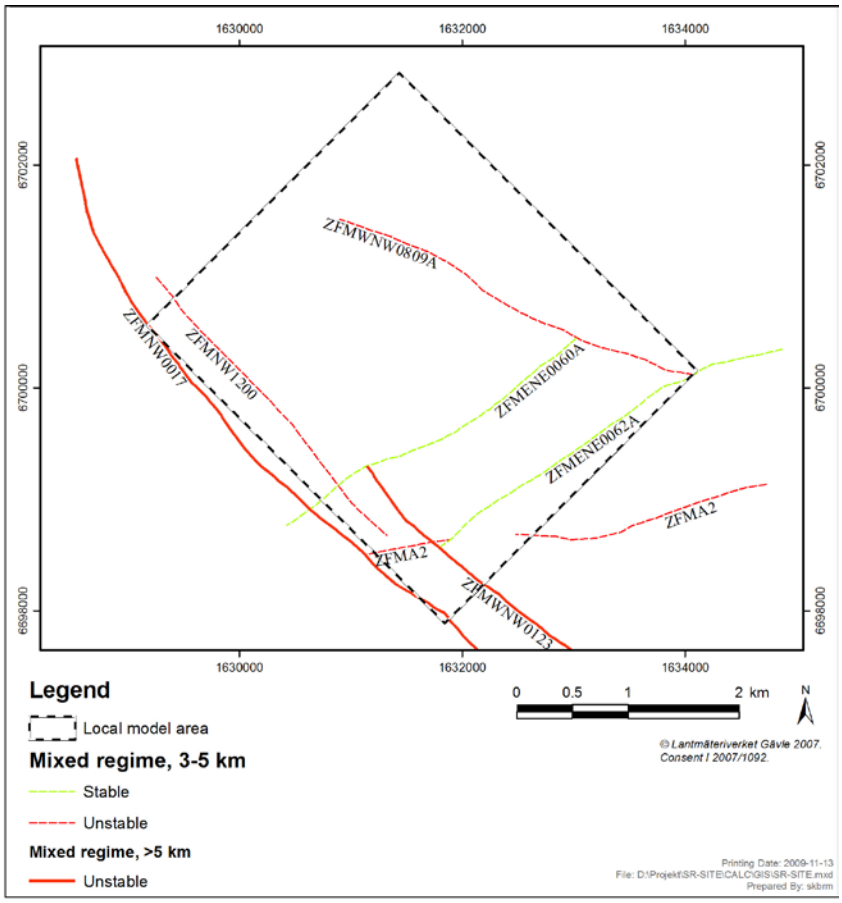

b)

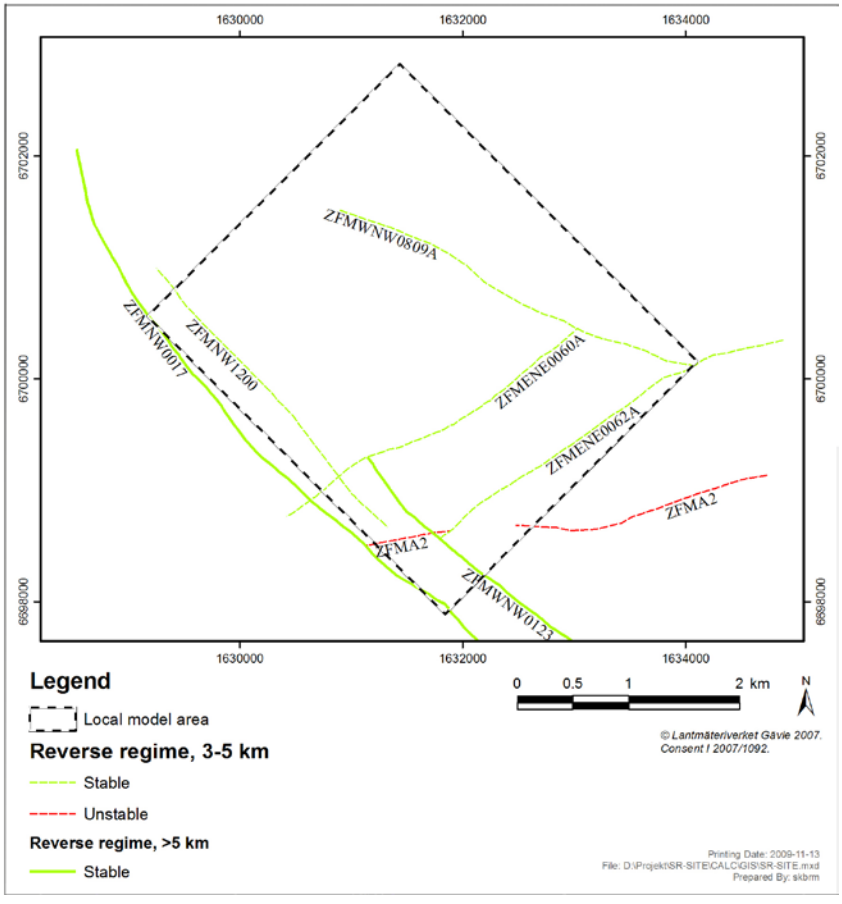

Figure 7-3. *Stability of zones > 3 km in trace length (a= mixed stress regime, b = reverse regime).*

Table 7-3. Number of canisters at various distances from deformation zones, classified according to fracture domain (8,126 canisters).

	rCrit=62.5/85 >5 km, 100–200 m	rCrit=125/170 >5 km, 200–400 m	rCrit=160/215 >5 km, 400–600 m	rCrit=225/>300 >5 km, >600 m	rCrit=75/100 3–5 km, 100–200 m	rCrit=150/200 3–5 km, 200–400 m	rCrit=235/>300 3–5 km, 400–600 m	rCrit=>300/>>300 3–5 km, >600 m
FFM01								
ZFMA2	–	–	–	–	349	1,759	2,288	2,239
ZFMNW0017	0	0	145	6,490	–	–	–	–
ZFMNW1200	–	–	–	–	89	423	836	5,287
ZFMWNW0123	189	729	901	4,816	–	–	–	–
ZFMWNW0809A	–	–	–	–	0	644	355	5,636
FFM06								
ZFMA2	–	–	–	–	0	0	514	977
ZFMNW0017	0	0	0	1,491	–	–	–	–
ZFMNW1200	–		–	–	0	0	0	1,491
ZFMWNW0123	0	0	0	1,491	–	–	–	–
ZFMWNW0809A	–	–	–	–	0	104	650	737

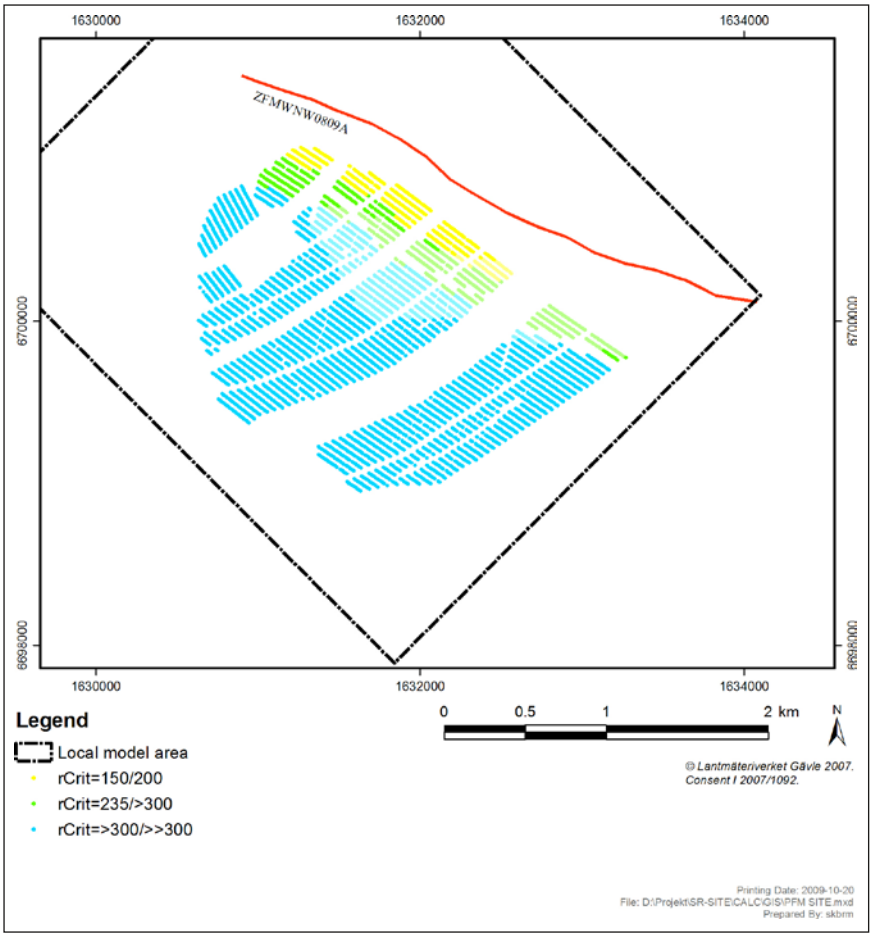

Figure 7-4. *Classification canister position according to critical radius.*

The anticipated number of FPI/100 m varies substantially with DFN model, as shown on Figure 7-5. For comparison, the Äspö HRL has on average 17 mapped FPI/100 m in the TBM drilled part of the facility whereas the Finnish Onkalo facility has 13 on average /Nordbäck et al. 2008/. A comparison of Figure 7-6 with Figure 7-5 reveals the strong inverse coupling between the degree-of-utilisation and the number of FPI/100 m. The degree-of-utilisation varies between about 70% and 90% for the DFN models r_0-fixed and TCM respectively with the model OSM+TFM in between these values.

On Figure 7-7 we display the simulated fraction of critical canisters per repository (i.e. having applied EFPC), using the probabilistic option (see Section 6.3) of target fracture slip, for each DFN model alternative. Combining Figure 7-7 with Table 7-3, which provides the number of canisters at various distances from deformation zones, we computed in Table 7-4, for each deformation zone, the number of critical canister positions (NCrit) by multiplying "Fraction", obtained from the simulations, with the number of canisters (from Table 7-3) in each class. Please note that "NCrit" represents number of canisters, not fractions. That is, the number of canisters is far less than one for all studied zones. This procedure was repeated for the remaining two DFN models, the result of which is provided in Appendix 1.

Table 7-5 and Table 7-6 summarises the number of critical positions using all DFN models assuming mixed- and reverse-slip stress regimes respectively. Please note that the numbers in Table 7-4 refer to 8,126 positions whereas Table 7-5 and Table 7-6 make use of the sums rescaled to reflect a 6,000 canister repository. The range provided in Table 7-5 reflects the fact that, for each model, the number of critical positions will depend on which of the zones that will reactivate seismically. Some deformation zones will affect fewer canisters than others. Essentially, the number of critical positions (e.g. "# Crit. Min" in Table 7-5) is obtained by combining the zone which affects the least number of canisters with the DFN model that yields the lowest intersection probabilities and doing the opposite to obtain "# Crit. Max".

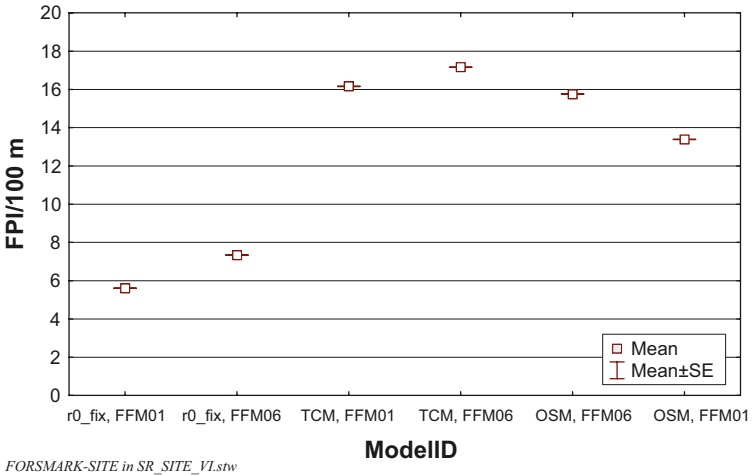

Figure 7-5. *FPI/100 m as a function of DFN model.*

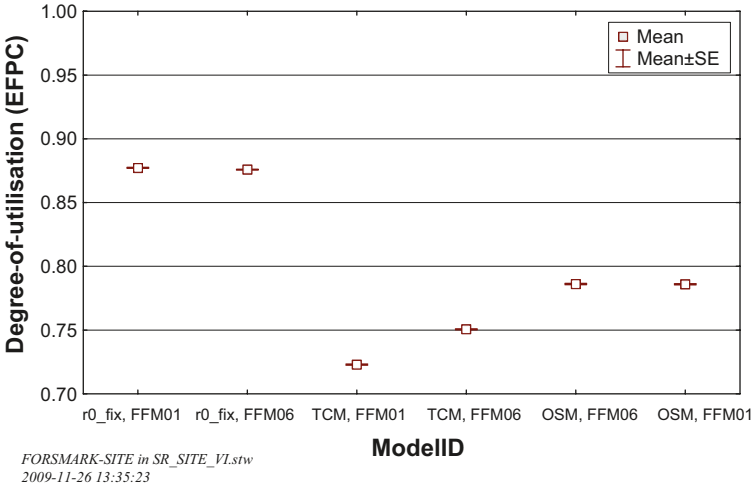

Figure 7-6. *Degree-of-utilisation as a function of DFN model.*

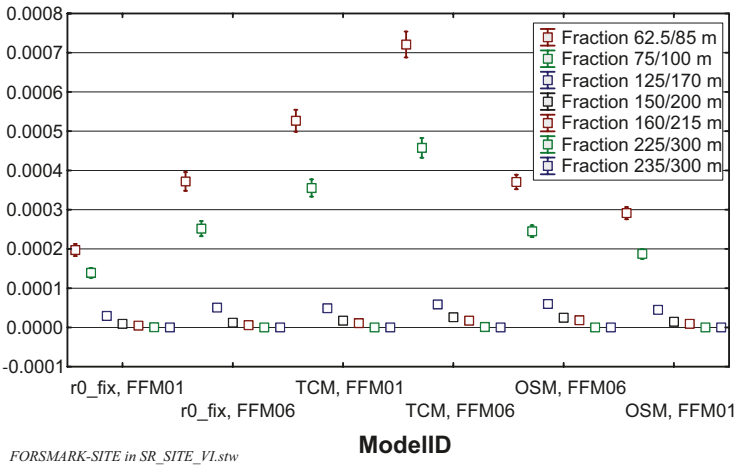

Figure 7-7. *Relative number (fraction) of canister positions that escaped the FPI criteria, classified by rock- (and fracture domain), that are intersected by critical fractures.*

Table 7-4. Number of critical canister positions, using DFN model "r_0-fixed". "Fraction" is the proportion of positions that escaped detection using EFPC. "Ncrit" is the number of canisters obtained by multiplying the fraction with the number of positions influenced by the zones (Table 7-3). Note that the number of positions "Ncrit" refer to a 8,126 canister repository (Table 7-3). In the bottom row, we sum the rows and rescale to a 6,000 canister repository.

Probabilistic	Valid N	Fraction	Minimum	Maximum	Std. Dev.	Ncrit				
r_0-fixed, FFM01						ZFMA2	ZFMNW0017	ZFMNW1200	ZFMWNW0123	ZFMWNW0809A
Fraction 62.5/85 m	50000	2.209E–04	0	0.6667	0.005303	0	0	0	4.175E–02	0
Fraction 75/100 m	50000	1.564E–04	0	0.6667	0.004569	0.054581	0	0.013918888	0	0
Fraction 125/170 m	50000	3.467E–05	0	0.4667	0.002373	0	0	0	0.025275888	0
Fraction 150/200 m	50000	1.183E–05	0	0.0857	0.000698	0.020816	0	0.005005782	0	0.007621096
Fraction 160/215 m	50000	6.520E–06	0	0.0638	0.000533	0	0.0009454	0	0.00587452	0
Fraction 225/300 m	50000	8.880E–07	0	0	0	0	0.00576312	0	0.004276608	0
Fraction 235/300 m	50000	0.000E+00	0	0	0	0	0	0	0	0
r_0-fixed, FFM06										
Fraction 62.5/85 m	50000	3.694E–04	0	0.6667	0.005303	0	0	0	0	0
Fraction 75/100 m	50000	2.557E–04	0	0.6667	0.004569	0	0	0	0	0
Fraction 125/170 m	50000	4.688E–05	0	0.4667	0.002373	0	0	0	0	0
Fraction 150/200 m	50000	1.415E–05	0	0.0857	0.000698	0	0	0	0	0.0014716
Fraction 160/215 m	50000	8.292E–06	0	0.0638	0.000533	0	0	0	0	0
Fraction 225/300 m	50000	0.000E+00	0	0	0	0	0	0	0	0
Fraction 235/300 m	50000	0.000E+00	0	0	0	0	0	0	0	0
					Sum, Rescaled to 6000	**0.0557**	**0.0050**	**0.0140**	**0.0570**	**0.0067**

Table 7-5. Number of critical canister positions for various DFN models, assuming mixed (strike-slip + reverse-slip) stress regime (6,000 canister repository).

Probabilistic slip, strike-slip + reverse (mixed) regime		
DFN Model	**# Crit. Min**	**# Crit. Max**
OSM+TFM	8.3E–04	6.7E–02
r_0-fixed	5.0E–03	5.7E–02
TCM	2.9E–03	1.2E–01

Table 7-6. Number of critical canister positions for various DFN models, assuming reverse-slip stress regime (6,000 canister repository).

Probabilistic slip. reverse regime	
DFN Model	**# Crit.**
OSM+TFM	6.4E–02
r_0-fixed	5.6E–02
TCM	1.2E–01

In Table 7-6 no range could be given simply because there is only one deformation zone, FFMA2 (Figure 7-3b), amenable to slip under reverse stress regime.

7.3.2 Laxemar

At Laxemar, ten deformation zones are within 600 m from any canister position (Figure 7-8). The structure ZSMNS001 display an apparent dextral offset by roughly 170 m along ZSMEW120A which is only about 1,200 m long. It is unlikely that this offset of ZSMNS001 is due to shear slip along ZSMEW120A; the slip/length ratio appears far too high. An alternative explanation to the

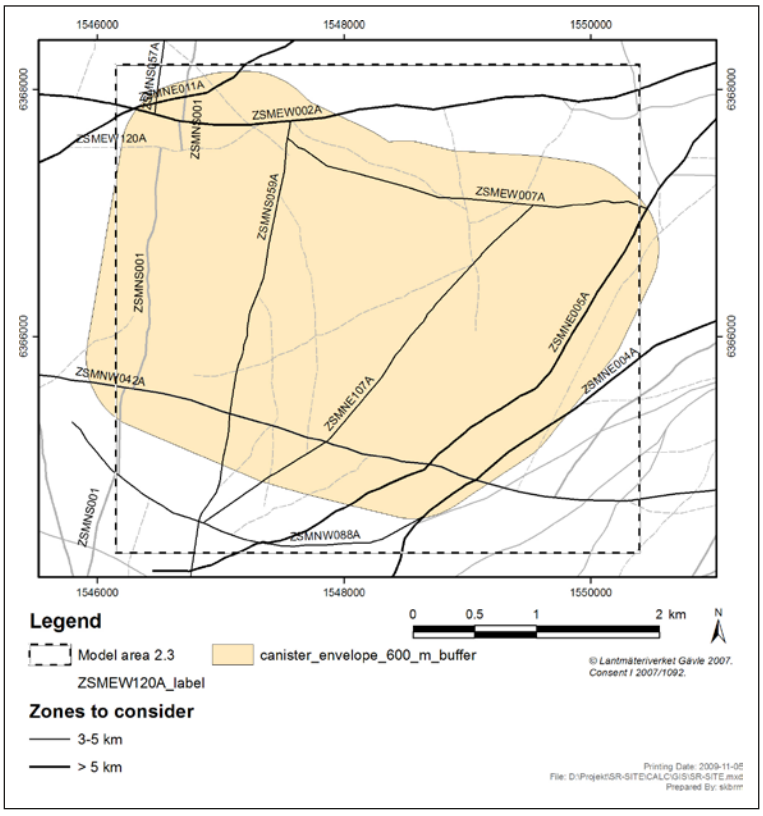

Figure 7-8. Zones within the 600 m envelope and having traces exceeding 3 km at the Laxemar site.

apparent offset is that ZSMEW120A is older than the ZSMNS001 segments and that growth of ZSMNS001 terminated against ZSMEW120A i.e. the apparent segments are judged to be separate structures. As these are < 3 km in trace length, we have excluded the suite of structures ZSMNS001x entirely from analyses.

According to /Lund et al. 2009/ and /Fälth et al. 2010/ the anticipated postglacial stress regime is strike-slip. Using the fault stability margins from /Lund et al. 2009, Fälth et al. 2010/ identified seven of the deformation zones that are anticipated to remain critical under these conditions. These are highlighted on Figure 7-9.

In contrast to Forsmark, the fracture- and rock domains at Laxemar do generally not share the same geometries. The thermal properties of the rock domains differ substantially; Three different canister spacings were defined for Laxemar (Table 7-1). Additionally, the fracture properties of the fracture domains, expressed in terms of DFN models, also differ. It was therefore necessary to identify unique combinations of fracture- and rock domains (Figure 7-10) so that the canister positions could be adequately classified (Figure 7-11). Additionally, we restricted analyses to the main DFN alternative "BMU" (see /La Pointe et al. 2008/, for details on DFN variants for Laxemar) to avoid variant explosion and, consequently, impractically long simulation times.

The number of canisters were counted for each combination of rock domain, fracture domain and buffer distances from deformation zones. In Table 7-7 we only display the counts for the combination FSM_C and RMSA01 for clarity (see Appendix 1 for remaining domain combinations).

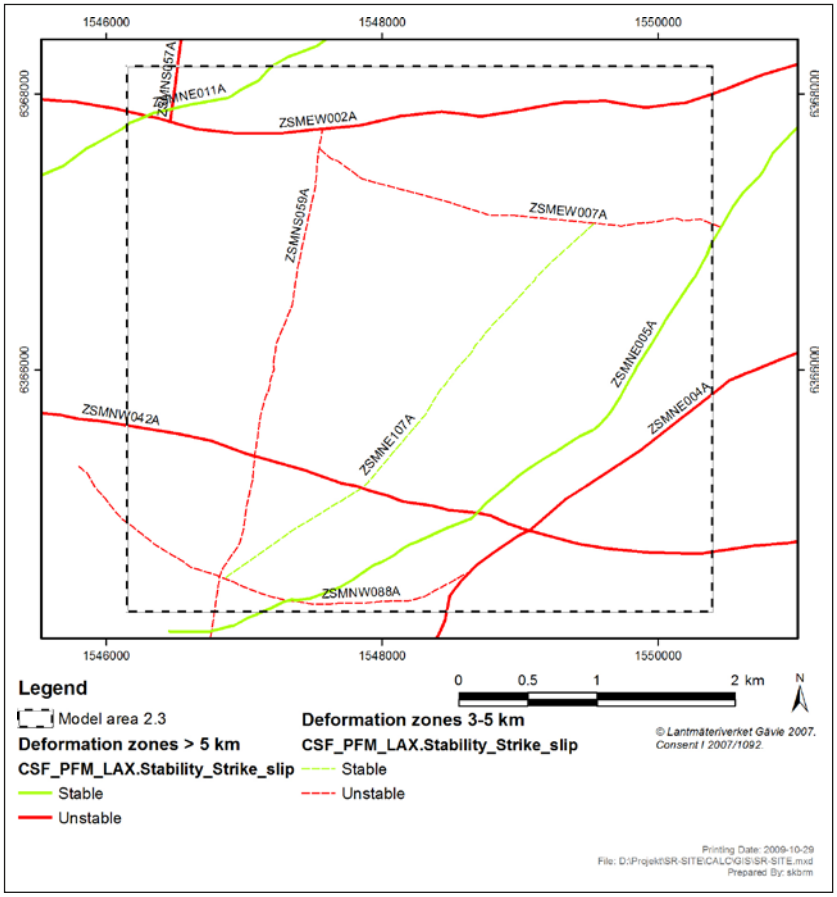

Figure 7-9. *Stability of zones > 3 km in trace length, mixed (strike-slip + reverse-slip) stress regime.*

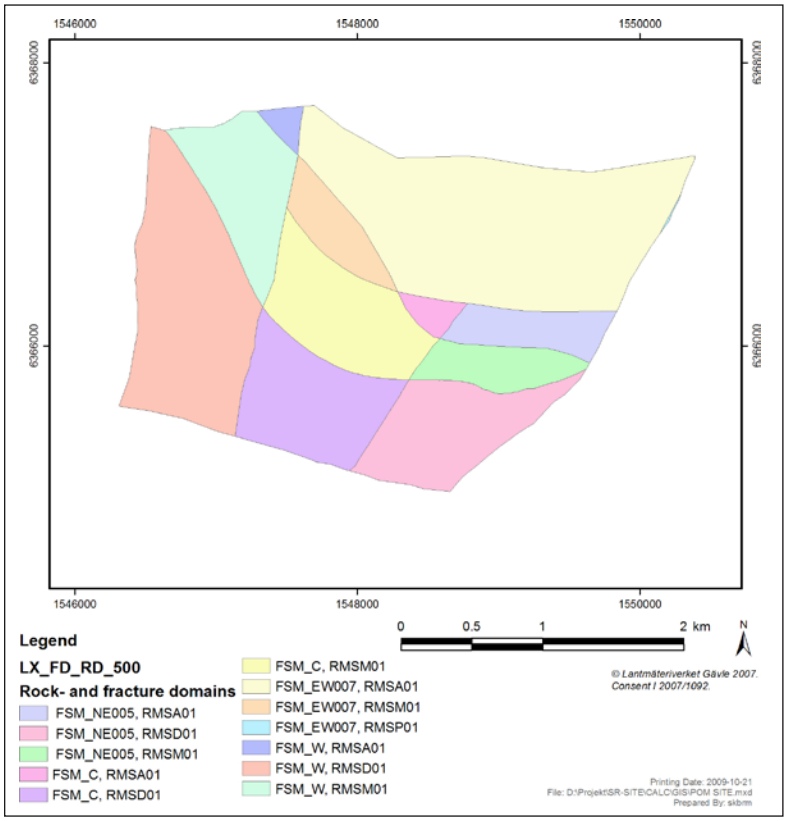

Figure 7-10. *Combination of rock- and fracture domains. Intersection at repository depth (–470 m).*

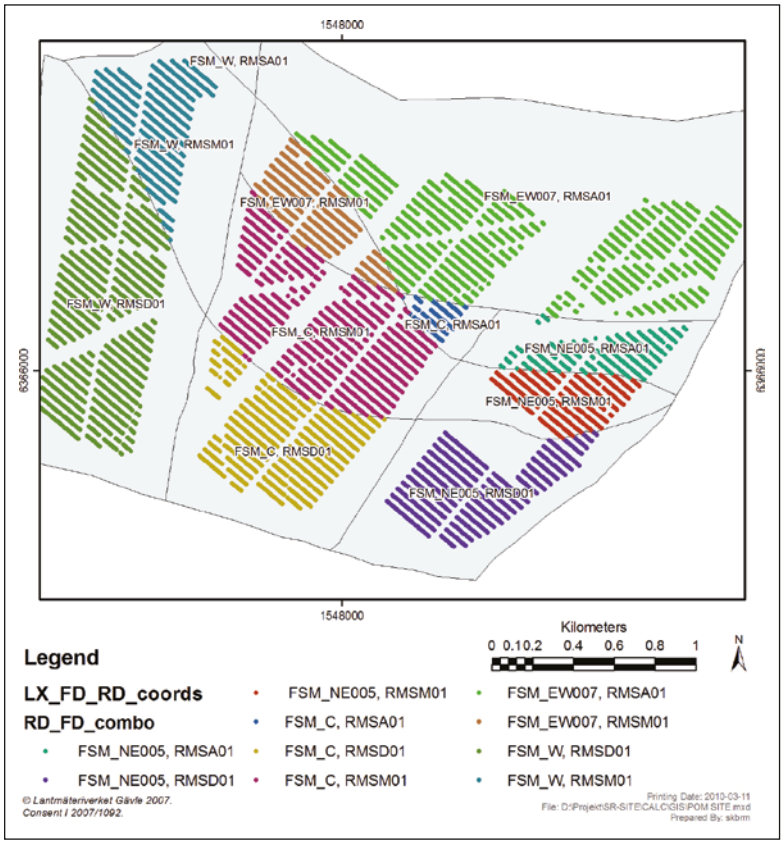

Figure 7-11. *Canister positions coded by rock (RMS)- and fracture (FSM) domain.*

Table 7-7. Number of canisters lying within fracture domain FSM_C and rock domain RMSA01, at various distances from different zones (see Appendix 1 for remaining domain combinations).

	rCrit=62.5/85 >5 km, 100–200 m	rCrit=125/170 >5 km, 200–400 m	rCrit=160/215 >5 km, 400–600 m	rCrit=225/>300 >5 km, >600 m	rCrit=75/100 3–5 km, 100–200 m	rCrit=150/200 3–5 km, 200–400 m	rCrit=235/>300 3–5 km, 400–600 m	rCrit=>300/>>300 3–5 km, >600 m
FSM_C, RMSA01								
ZSMEW002A	0	0	0	98				
ZSMNS057A	0	0	0	98				
ZSMNW042A	0	0	0	98				
ZSMNE004A	0	0	0	98				
ZSMNW088A					0	0	0	98
ZSMNS059A					0	0	0	98
ZSMEW007A					0	0	22	76

The anticipated number of FPI/100 m varies slightly with domain as shown on Figure 7-12. These differences reflect the differences in the DFN models for the different fracture domains FSM_C, FSM_EW007, FSM_NE005 and FSM_W.

The degree-of-utilisation varies between about 84% and 89% (Figure 7-13). The differences are due to differences in DFN models and, more importantly, due to differences in spacing between the different rock domains. The larger the canister distance, the higher the degree-of-utilisation (see Section 6.2).

The number of critical fractures for each combination of rock- and fracture domain is tabulated in Table 7-8 (using fractions from Figure 7-14) and Appendix 1. Depending on which of the deformation zones that was reactivated seismically, the number of critical canisters vary between 0 (FSMNW088A) and 0.05 (ZSMNW042A) canisters per repository (Table 7-9).

Note that we due to time constraint only made full simulation the main DFN alternative, “BMU”. To address the differences in DFN models for Laxemar, we ran a batch of simulations using only fracture domain FSM_C and 8.1 m canister spacing (Table 7-10). We judge the differences between the different DFN models sufficiently small, in the light of the overall uncertainties, that the impact of the DFN model can be disregarded in this context.

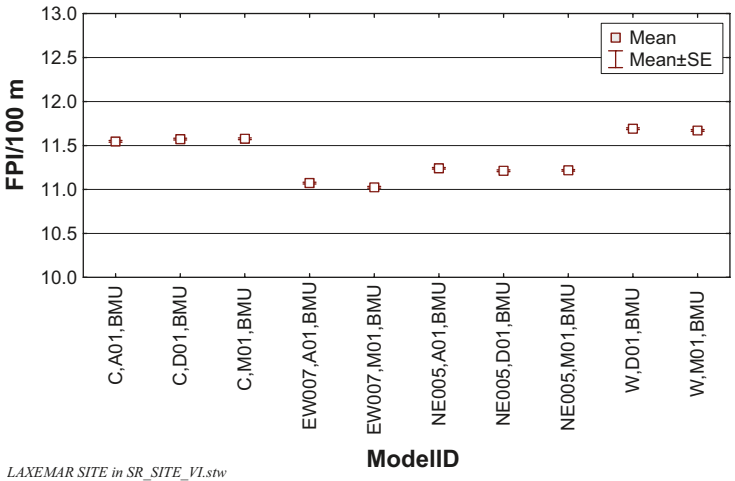

Figure 7-12. *Number of FPI/100 for various fracture domains, Laxemar.*

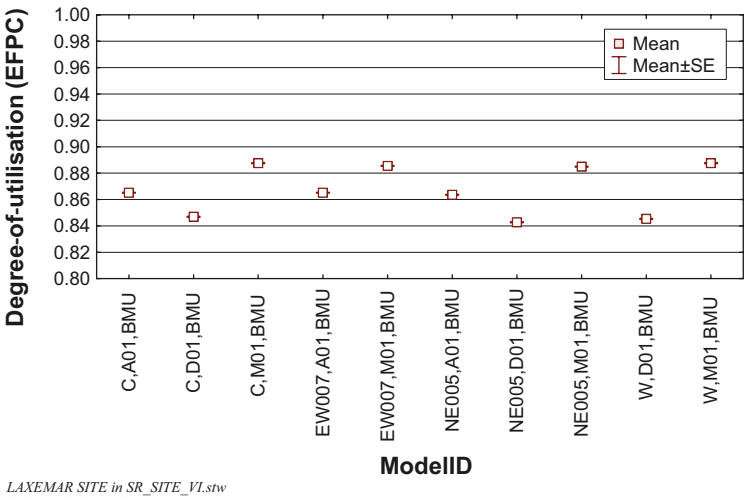

Figure 7-13. *Degree-of-utilisation as a function of fracture domain, Laxemar.*

Table 7-8. Number of critical canister positions, using DFN model "BMU" for a subset of domain combinations. The full table is provided in Appendix 1.

Probabilistic	Valid N	Fraction	Minimum	Maximum	Std. Dev.	Ncrit						
FSM_C, RMSA01						ZSMEW002A	ZSMEW007A	ZSMNE004A	ZSMNS057A	ZSMNS059A	ZSMNW042A	ZSMNW088A
Fraction 62.5/85 m	35000	1.92E–04	0.00E+00	2.81E–01	5.10E–03	0	0	0	0	0	0	0
Fraction 75/100 m	35000	1.14E–04	0.00E+00	1.33E–01	3.22E–03	0	0	0	0	0	0	0
Fraction 125/170 m	35000	3.33E–05	0.00E+00	1.33E–01	1.94E–03	0	0	0	0	0	0	0
Fraction 150/200 m	35000	2.67E–05	0.00E+00	1.33E–01	1.89E–03	0	0	0	0	0	0	0
Fraction 160/215 m	35000	2.67E–05	0.00E+00	1.33E–01	1.89E–03	0	0	0	0	0	0	0
Fraction 225/300 m	35000	2.00E–05	0.00E+00	1.00E–01	1.41E–03	1.96E–03	0	1.96E–03	1.96E–03	0	1.96E–03	0
Fraction 235/300 m	35000	0.00E+00	0.00E+00	0.00E+00	0.00E+00	0	0	0	0	0	0	0
FSM_C, RMSD01												
Fraction 62.5/85 m	35000	1.77E–04	0.00E+00	1.18E–01	3.10E–03	0	0	0	0	0	2.07E–02	0
Fraction 75/100 m	35000	9.74E–05	0.00E+00	8.82E–02	2.16E–03	0	0	0	0	3.61E–03	0	0
Fraction 125/170 m	35000	2.35E–05	0.00E+00	5.41E–02	9.95E–04	0	0	0	0	0	1.01E–02	0
Fraction 150/200 m	35000	1.15E–05	0.00E+00	3.03E–02	5.74E–04	0	0	0	0	2.52E–03	0	0
Fraction 160/215 m	35000	6.06E–06	0.00E+00	3.03E–02	4.29E–04	0	0	0	0	0	2.46E–03	0
Fraction 225/300 m	35000	0.00E+00	0.00E+00	0.00E+00	0.00E+00	0	0	0	0	0	0	0
Fraction 235/300 m	35000	0.00E+00	0.00E+00	0.00E+00	0.00E+00	0	0	0	0	0	0	0

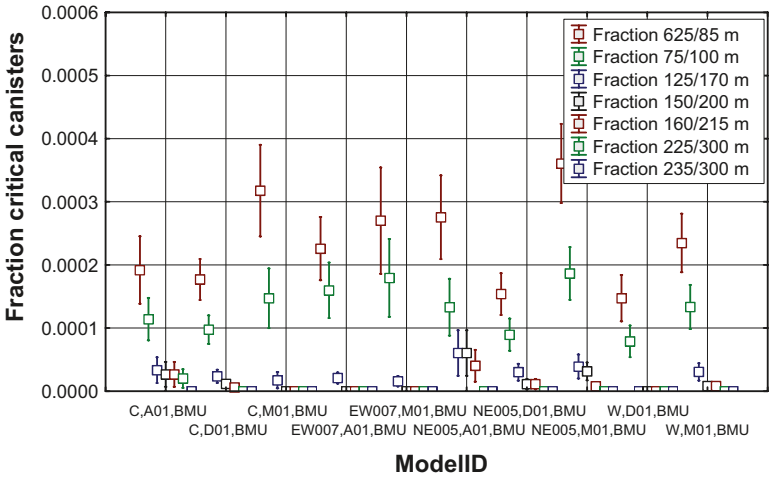

Figure 7-14. *Relative number (fraction) of canister positions that escaped the FPI criteria, classified by rock- and fracture domain, that are intersected by critical fractures.*

Table 7-9. Number of critical canister positions assuming mixed stress regime (6,000 canister repository). Note that only the main DFN model alternative (BMU) was used for this computation.

Probabilistic slip, mixed (strike-slip + reverse) regime		
DFN Model	**# Crit. Min**	**# Crit. Max**
BMU, All domains	0.0000E+00	5.638E–02

Table 7-10. Number of critical canister positions assuming mixed stress regime (6,000 canister repository) at Laxemar. Unlike Table 7-9, only one fracture domain (FSM_C) and one canister spacing (8.1 m) was simulated.

Model	# Crit. Min	# Crit. Max
BMU, C	0.00E+00	2.48E–02
BM, C	0.00E+00	1.68E–02
BMU_alt. C	0.00E+00	1.10E–02
BM_alt. C	0.00E+00	6.78E–03

8 Discussion

8.1 Efficiency

The FPI criteria classifies fractures as critical no matter what their size, as long as a set of conditions, assumptions really, are fulfilled. The usefulness of the of the FPI approach will depend on its ability to detect critical fractures under various conditions. However, this must naturally be balanced against the cost in terms of degree-of-utilisation (Section 8.2). From a long term safety perspective, however, the only relevant aspect is its ability to detect critical fractures.

As defined in Section 3.4, the efficiency of the FPI criteria for detecting critical canister positions can be addressed by comparing it to a blind deposition (i.e. no discrimination criteria). As shown in Table 8-1 and Table 8-2, the efficiency is about 97% to 99% for all DFN cases (both sites). In other words, of all fractures that are critical and intersect canister positions, the FPI criteria were able to detect ≥ 97% for the Laxemar and Forsmark cases respectively.

8.2 Cost of FPI in terms of degree-of-utilisation

In Table 8-3, we list some fracture statistics for a particular simulation (10,000 realisations) of the Forsmark base case. The overwhelmingly dominant intersection type is the FPI intersections, constituting over 99% of the fractures that intersect any part of the repository system. As shown on Figure 8-1, only about 20% of these fractures have truly critical radii (≥ 62.5, see Table 7-2). DFN aspects set aside, this is mainly a function of tunnel cross-sectional area and, to a lesser extent, its shape. The smaller the cross-sectional area, the higher the portion of fractures erroneously classified as critical. There will, naturally, be a limit below which the FPI criteria are rendered useless as proxy for large fractures because the cost in terms of degree-of-utilisation will simply be too large. It is apparent that if some portion of the fracture array could be somehow measured in terms of size, the vast conservativeness inherent in the method will be decreased.

Table 8-1. Efficiency of FPI criteria applied to Forsmark using the influence of deformation zone ZFMA2.

Model	# canisters EFPC	# canisters Blind	Efficiency
OSM+TFM	6.44E–02	3.60E+00	98.2%
r_0-fixed	5.57E–02	2.22E+00	97.5%
TCM	1.21E–01	4.00E+00	97.0%

Table 8-2. Efficiency of FPI criteria applied to Laxemar using the influence of deformation zone ZSMNW042A. “BMU” is the base DFN model for Laxemar whereas “BM”, “BMU_alt” and “BM_alt” constitute alternatives /La Pointe et al. 2008/.

Model	# canisters EFPC	# canisters Blind	Efficiency
BMU	2.48E–02	1.00E+00	97.5%
BM	1.68E–02	1.02E+00	98.4%
BMU_alt	1.10E–02	6.35E–01	98.3%
BM_alt	6.78E–03	5.73E–01	98.8%

Table 8-3. Frequency of different types of intersection, for a 10,000 realisation simulation of the base case. 1= FPI, 2xx = EFPC where xx stands for number of intersected canisters, 300 = initially critical fracture, but canister is not within critical radius, 3xx = critical fracture where xx stands for number of intersected canisters.

Type	Count	Cumulative Count	Percent	Cumulative percent
1	134,558	134,558	99.13725	99.1373
205	88	134,646	0.06484	99.2021
206	62	134,708	0.04568	99.2478
207	49	134,757	0.0361	99.2839
208	52	134,809	0.03831	99.3222
209	32	134,841	0.02358	99.3458
210	28	134,869	0.02063	99.3664
211	15	134,884	0.01105	99.3774
212	20	134,904	0.01474	99.3922
213	19	134,923	0.014	99.4062
214	16	134,939	0.01179	99.418
215	10	134,949	0.00737	99.4253
216	8	134,957	0.00589	99.4312
217	12	134,969	0.00884	99.4401
218	6	134,975	0.00442	99.4445
219	5	134,980	0.00368	99.4482
220	3	134,983	0.00221	99.4504
221	10	134,993	0.00737	99.4577
222	3	134,996	0.00221	99.46
223	3	134,999	0.00221	99.4622
224	3	135,002	0.00221	99.4644
225	2	135,004	0.00147	99.4658
226	2	135,006	0.00147	99.4673
228	2	135,008	0.00147	99.4688
229	1	135,009	0.00074	99.4695
230	1	135,010	0.00074	99.4703
233	1	135,011	0.00074	99.471
236	1	135,012	0.00074	99.4717
249	1	135,013	0.00074	99.4725
300	577	135,590	0.42511	99.8976
301	59	135,649	0.04347	99.9411
302	34	135,683	0.02505	99.9661
303	24	135,707	0.01768	99.9838
304	10	135,717	0.00737	99.9912
305	6	135,723	0.00442	99.9956
306	1	135,724	0.00074	99.9963
307	1	135,725	0.00074	99.9971
308	1	135,726	0.00074	99.9978
310	1	135,727	0.00074	99.9985
311	2	135,729	0.00147	100

In Section 6.6 we explored the consequences of being able to measure the size of some, or all, potentially critical fractures.

A back-of-the-envelope calculation assuming blind deposition (no discrimination criteria) Hedin's epsilon /Hedin 2008/ and using the r_0-fixed DFN alternative for FFM01, indicates that about 386 deposition holes are intersected by fractures exceeding 62.5 m (applies to gently dipping fractures) and 85 m (applies to steep fractures) in radius. This would, conservatively assuming that the full 6 m spacing is rejected, require an additional 2.3 km of deposition tunnel. This corresponds to a degree-of-utilisation of roughly 94%. If all truly large fractures could somehow be detected and

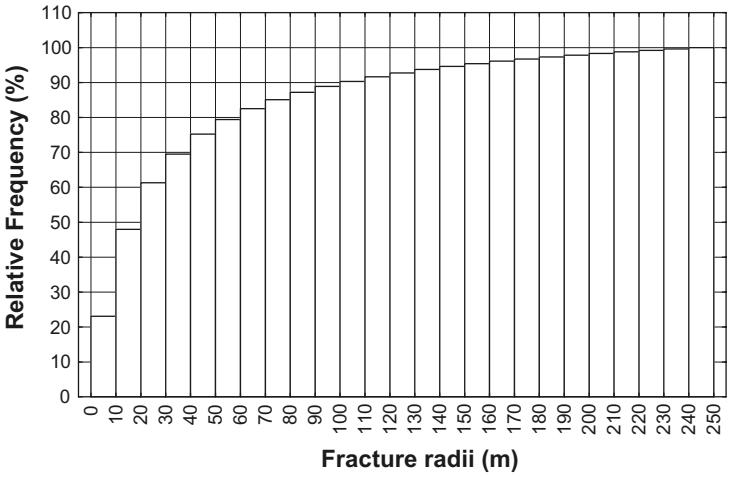

Include condition: 'Intersection type'= 'FPI'
2009-11-06 10:23:26

Figure 8-1. *Size distribution of FPI fractures.*

avoided, the degree-of-utilisation would be slightly better, about 96% (Figure 6-14a). The simulated degree-of-utilisation is 89% so the "price" of minimising the seismic hazard using the FPI criteria would be that related to the construction of a larger (about 7% larger) repository.

The difference, however, will be larger for more dense networks. Using the densest DFN model for FFM01 in the actual size range, the "TCM" model, 726 positions are affected which, following the reasoning above and again assuming the full 6 m spacing is wasted, corresponds to a degree-of-utilisation of about 88%. If all truly discriminating fractures could be detected, the degree-of-utilisation is slightly higher, about 91.5%.The simulated degree-of-utilisation using FPI criteria is about 73% (Figure 6-14b) and the "cost" is therefore that involved in the construction of a larger (about 15% larger) repository. Thus, the denser the network, the more conservative the FPI criteria in the sense that more small fractures are erroneously classified as critical compared to less dense networks.

Though the cost of using FPI to identify structures critical to long term safety is indeed substantial, in terms of economy, time, environmental impact, etc, nevertheless, because of its high efficiency (see Section 8.1), the FPI criteria essentially eradicates the seismic risk.

8.3 A tale of tails

The powerlaw fracture radius distribution, however elegant and simple to integrate, is quite deceitful in the sense that it is very difficult to predict the outcome of the simulations and hence to have a feeling for whether the simulations are somewhat correct or not. The construction of benchmarks were quite time consuming but, in retrospect, well worth the efforts because many flaws in the logic were detected in the codes thanks to these benchmarks. However, there are no analytical solutions (yet) to solve for the fraction of critical positions remaining after the application of the FPI criteria and therefore nothing else to compare the results with. The only way to check that the codes behaved as expected was to plot subsamples of realisations in 3D and examine the simulation outcome by visual inspection. This could be done for a selected number of realisations but obviously not for all.

The introduction of decaying slip towards fracture tips and, later, a probabilistic variant of the decaying slip function had the consequence that intersection between a canister and a critical fracture became a very rare event indeed. For the statistic "fraction 62.5/85 m", to stabilise, over 400 full repositories (containing 6,000 canisters each) needed to be simulated, producing a total of about 600 potentially critical canister positions. On average, about 100 realisations (≈ 5,000 canisters) needed to be run to obtain a single critical canister and it was considered far to time consuming to manually check each realisation for eventual flaws.

As discussed briefly in Section 5.8, the number of necessary realisations will depend on the desired statistic. For instance, the number of FPI/100 m and the degree-of-utilisation stabilises at roughly 1,500 realisations, as seen on Figure 8-2a and Figure 8-2b respectively. The mean fraction critical positions intersected by fractures of radii 62.5/85 m (Figure 8-3a), appears to start stabilising at roughly 20,000–25,000 realisations whereas the class of 125/170 m radii (Figure 8-3b), even rarer events, appears to start stabilising at roughly 30,000–35,000 realisations.

a)

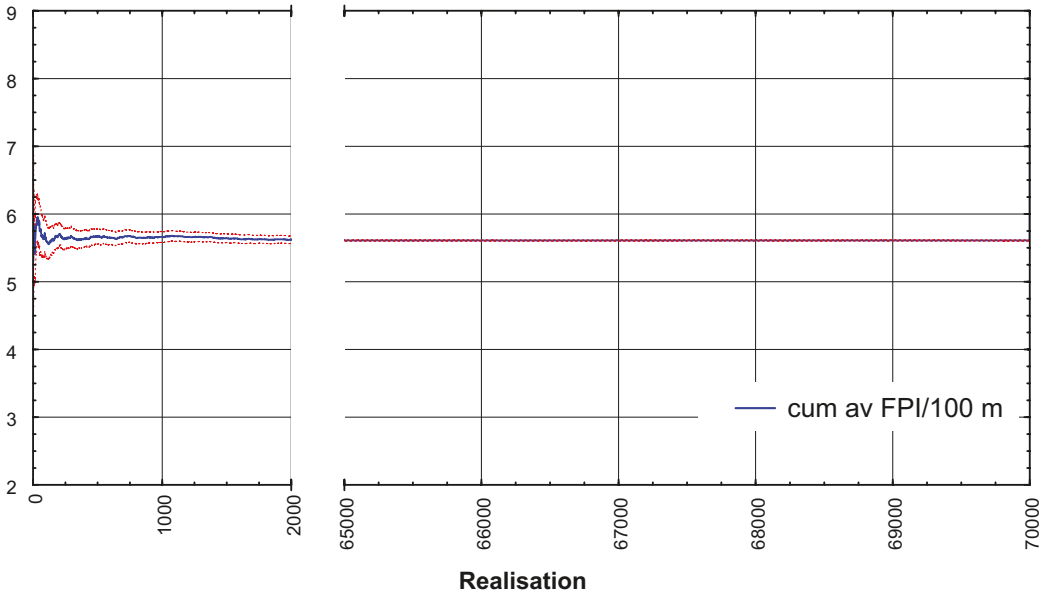

Cumulative averages Forsmark in SR_SITE_VI.stw
2009-11-24 13:25:39
Include condition: ModelID = 'r0_fix, FFM01'

b)

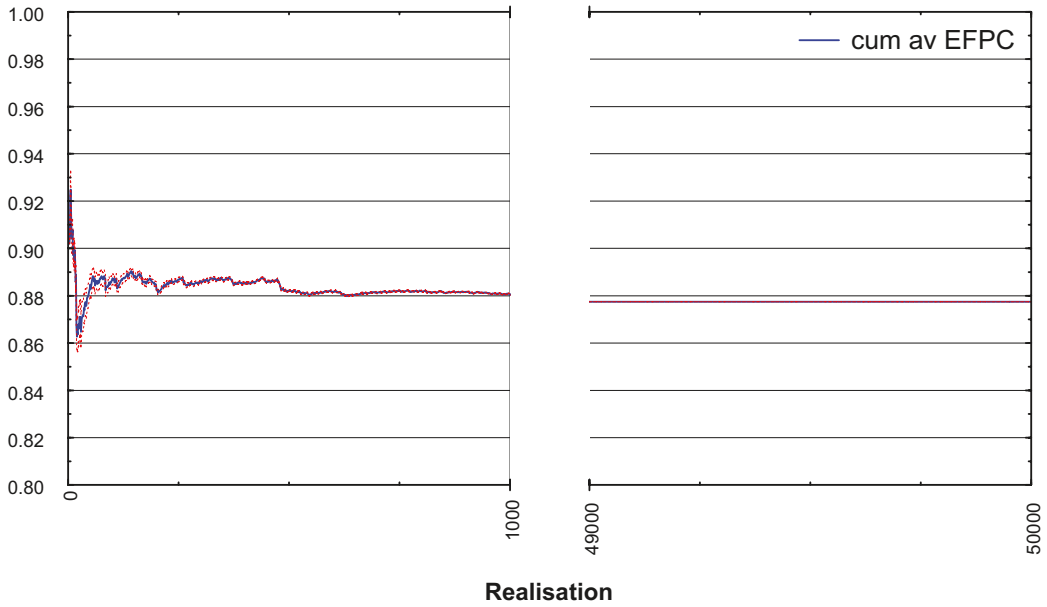

Cumulative averages Forsmark in SR_SITE_VI.stw
2010-03-11 21:25:26
Include condition: ModelID = 'r0_fix, FFM01'

Figure 8-2. *a) Number of FPI/100 m for DFN model "r_0-fixed, FFM01". b) Degree-of-utilisation (EFPC). Dashed lines represent the confidence band at $\alpha = 0.05$.*

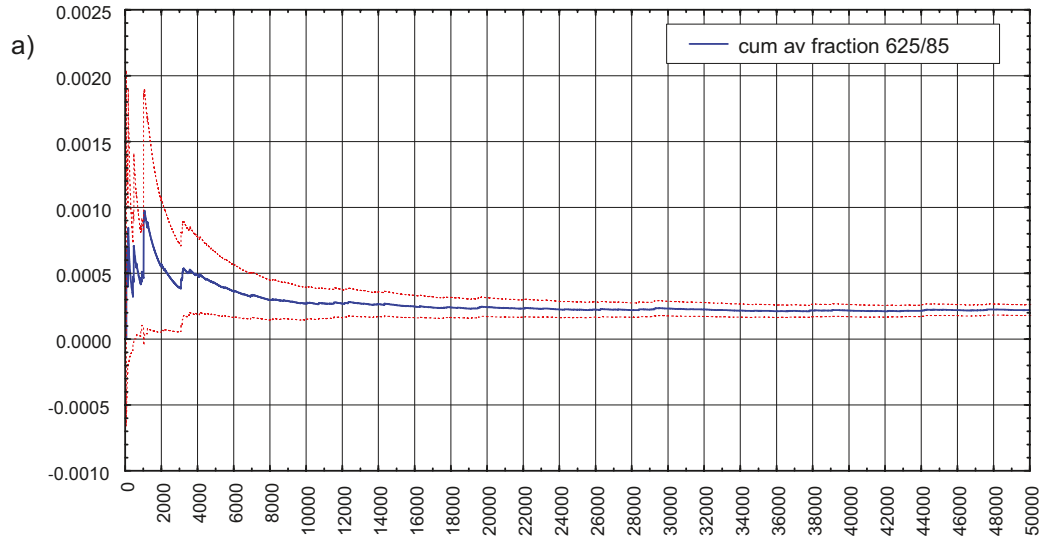

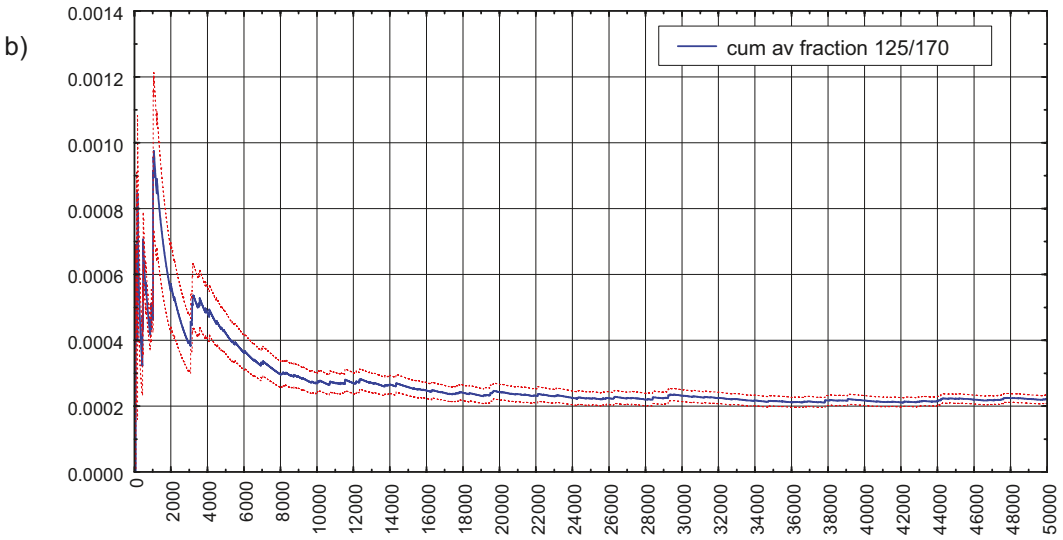

Figure 8-3. *Fraction critical positions for the fracture radii of 62.5/85 m (a) and 125/170 m (b), using DFN model "r_0-fixed, FFM01". Dashed lines represent the confidence band at α = 0.05.*

The number of necessary realisations requires weeks of CPU-time on fairly powerful workstations *for each DFN model*. In retrospect, it would have been wise to develop parallelised codes to avoid these long simulation times. Additionally, the codes are hampered by numerous options included to facilitate a multitude of test cases and benchmarks. Large portions of the codes are repeated by copy/paste of codelets, to save development time but this generated a major source of error. A lot of time was spent searching for subtle differences in seemingly identical lines of code that produced simulation errors detected by benchmarks, gut-feeling or mere chance. Thus, had more time been invested in code-design, there would have been fewer errors, less time spend on debugging with a much faster code as a result. The lesson learnt is simple: However exciting the problem is at hand, the less engaging (i.e. boring) procedures of code architecture are quite worth the effort and should take precedence before fast (and often erroneous) acquisition of results. Also, the number of necessary realisations cannot readily be estimated from proxy statistics, but need to be evaluated for the desired statistic, which is far too often neglected (the author included) in monte-carlo simulations.

9 Conclusions and recommendations

In this report, we demonstrated that the FPI criteria are indeed efficient in identifying discriminating fractures should they be employed in a repository. We have shown that the number of critical positions, i.e. positions that escaped detection by the FPI criteria, can be computed by simulation and that the consequence of using FPI criteria, the degree-of-utilisation, is acceptable. We can therefore recommend the FPI criteria as a proxy for large fractures in the absence of more direct identification methods or as a complement thereof.

To address the effect of using FPI criteria on a site yet to be explored, we employed stochastic simulations of fracture-canister intersections. Though such simulations could be setup to mimic procedures anticipated in a real repository, simulation times were very long because a range of DFN models were brought through the simulations and because the occurrence of critical positions is a rare event. Therefore, efforts should be invested in discriminating between various proposed DFN models, before forwarding the full DFN spectrum to simulations such as those presented here. If no preferred model can be readily presented, as the "BMU" model was forwarded for Laxemar, then all proposed DFN models for each site need to be forwarded to encompass the full uncertainty space. Though the efficiency of the criteria will only to a minor extent be controlled by the DFN model, the uncertainty in the estimation of degree-of-utilisation might be very large and difficult to handle in other instances.

If the FPI criteria are used as here proposed, very few canisters will, on average, be subject to the detrimental effects of earthquakes. At Forsmark, on average 8.3E–04 to 1.2E–01 (Table 7-5) canisters are critical (0–5.64E–02 canisters at Laxemar (Table 7-9) depending on which deformation zone is assumed to reactivate and taking the full DFN uncertainty space into consideration. However, this assumes that:

- with probability = 1, there will be an earthquake ≥ M6 located at the site,
- it will take place on one of the zones located closest (≤ 600 m) to the canisters,
- it will accommodate the largest slip, stress drop and slip velocity possible, given its dimensions.

Additionally, we make no use of information that can be obtained from other tunnels. We find it unlikely that such information would pass unnoticed during excavation and subsequent modelling of the underground facility. Making use of observations in neighbouring tunnels has the potential of reducing the number of critical canisters by half.

Similarly, we find it entirely unrealistic to assume that critical fractures can be identified only with the FPI criteria. Most certainly, a subset of the critical fractures are also hydraulically active, display previous shear displacements or have large apertures/thicknesses to ease identification of critical fractures even if only small portions are exposed.

Altogether, therefore, the results presented here should be regarded as conservative.

10 References

SKB's (Svensk Kärnbränslehantering AB) publications can be found at www.skb.se/publications. References to SKB's unpublished documents are listed separately at the end of the reference list. Unpublished documents will be submitted upon request to document@skb.se.

ArcMap, 2006. Version: 9.2 (build 1420). ESRI. www.esri.com.

Ayjara D F A, 2007. http://planetmath.org/encyclopedia/QuarticFormula.html.

Börgesson L, Johannesson L-E, Hernelind J, 2003. Earthquake induced rock shear through a deposition hole. Effect on the canister and the buffer. SKB TR-04-02, Svensk Kärnbränslehantering AB.

Cosgrove, J, Stanfors R, Röshoff K, 2006. Geological characteristics of deformation zones and a strategy for their detection in a repository. SKB R-06-39, Svensk Kärnbränslehantering AB.

Curtis P, Elfström M, Maarkström I, 2007. Rock Visualization System. Technical description (RVS version 4.0). SKB R-07-44, Svensk Kärnbränslehantering AB.

Darcel C, Davy P, Bour O, De Dreuzy J R, 2006. Discrete fracture network for the Forsmark site. SKB R-06-79, Svensk Kärnbränslehantering AB.

Davis J C, 1986. Statistics and Data Analysis in Geology, John Wiley & Sons, New York. Volume.

Dershowitz W, 1985. Rock Joint System. Ph.D.-Thesis, MIT. Cambridge, Mass.

Devroye L, 1986. Non-Uniform Random Variate Generation, Springer-Verlag, New York. Volume.

Eshelby J, 1957. The determination of the elastic field of an elliptical inclusion and related problems. Proc. Roy. Soc., London. Volume: A241, Pages: 376–396.

Evans M, Hastings N, Peacock B, 2000. Statistical distributions, third edition, John Wiley & Sons Inc. Volume.

Fox A, La Pointe P, Hermanson J, Öhman J, 2007. Statistical geological discrete fracture network model. Forsmark modelling stage 2.2. SKB R-07-46, Svensk Kärnbränslehantering AB.

Fälth B, Hökmark H, 2006. Seismically induced slip on rock fractures. Results from dynamic discrete fracture modeling. SKB R-06-48, Svensk Kärnbränslehantering AB.

Fälth B, Hökmark H, Munier R, 2007. Seismically Induced Shear Displacements in Repository Host Rock Fractures. 9th Canadian conference on Earthquake Engineering. Ottawa, Canada.

Fälth B, Hökmark H, Munier R, 2008. Seismically induced slip on rock fractures – expanded study with particular account of large earthquakes. 42nd U.S. Rock Mechanics Symposium. San Fransisco 2008.

Fälth B, Hökmark H, Munier R, 2010. Effects of large earthquakes on a KBS-3 repository. Evaluation of modelling results and their implications for layout and design. SKB TR-08-11. Svensk Kärnbränslehantering AB.

Hedin A, 2005. An analytic method for estimating the probability of canister/fracture intersections in a KBS-3 repository. SKB R-05-29, Svensk Kärnbränslehantering AB.

Hedin A, 2008. Semi-Analytic Stereological Analysis of Waste Package/Fracture Intersections in a Granitic Rock Nuclear Waste Repository. In: Mathematical Geosciences, doi: 10.1007/s11004-008-9175-3.

Hedin A, 2011. Stereological method for reducing probability of earthquake-induced damage in a nuclear waste repository. In: Mathematical Geosciences, doi: 10.1007/s11004-010-9303-8.

Hermanson, Forssberg J O, Fox A, La Pointe P, 2005. Statistical model of fractures and deformation zones. Preliminary site description, Laxemar subarea, version 1.2. SKB R-05-45, Svensk Kärnbränslehantering AB.

Kim Y-S, Sanderson D J, 2005. The relationship between displacement and length of faults; a review. Earth-Science Reviews 68(3-4): pp 317–334.

La Pointe P, Fox A, Hermanson J, Öhman J, 2008. Geological discrete fracture network model for the Laxemar site. Site Descriptive Modelling SDM-Site Laxemar. SKB R-08-55, Svensk Kärnbränslehantering AB.

Lund B, Schmidt P, Hieronymus C, 2009. Stress evolution and fault stability during the Weichselian glacial cycle. SKB TR-09-15, Svensk Kärnbränslehantering AB.

Ma K-F, Brodsky E E, Mori J, Ji C, Song T-R A, Kanamori H, 2003. Evidence for fault lubrication during the 1999 Chi-Chi, Taiwan, eathquake (Mw7.6). In: Geophysical Research Letters, vol 30(5).

MatLab, 2008. Version: 7.7.0.471 (R2008b). The MathWorks Inc. 3 Apple Hill Drive, Natick, MA 01760-2098, USA. http:\\www.matlab.com.

Munier R, 2004. Statistical analysis of fracture data, adapted for modelling Discrete Fracture Networks-Version 2. SKB R-04-66, Svensk Kärnbränslehantering AB.

Munier R, 2006. Using observations in deposition tunnels to avoid intersections with critical fractures in deposition holes. SKB R-06-54, Svensk Kärnbränslehantering AB.

Munier R, 2007. Demonstrating the efficiency of the EFPC criterion by means of Sensitivity analyses. SKB R-06-115, Svensk Kärnbränslehantering AB.

Munier R, Hökmark H, 2004. Respect distances. Rationale and means of computation. SKB R-04-17, Svensk Kärnbränslehantering AB.

Muraoka H, Kamata H, 1983. Displacement distribution along minor fault traces. Journal of Structural Geology 5(5): pp 483–495.

Nordbäck N, Engström J, Kemppainen K, 2008. Outcome of the geological mapping of the ONKALO underground research facility access tunnel, chainage 0-990. Posiva Working Report 2008-84, Posiva Oy.

Schneider P, Eberly D, 2003. Geometric tools for computer graphics, Morgan Kaufmann Publishers, San Fransisco, USA. Volume. ISBN: 1-55860-594-0.

SKB 2004. Deep repository. Underground design premises. Edition D1/1. SKB R-04-60, Svensk Kärnbränslehantering AB.

SKB 2006. Geosphere process report for the safety assessment SR-Can. SKB TR-06-19, Svensk Kärnbränslehantering AB.

SKB 2008. Site description of Forsmark at completion of the site investigation phase. SDM-Site Forsmark. SKB TR-08-05, Svensk Kärnbränslehantering AB.

SKB 2009a. Site description of Laxemar at completion of the site investigation phase. SDM-Site Laxemar. SKB TR-09-01, Svensk Kärnbränslehantering AB.

SKB 2009b. Final repository facility. Underground design premises/D2. SKB R-07-33, Svensk Kärnbränslehantering AB.

SKB, 2009c. Design premises for a KBS-3V repository based on results from the safety assessment SR-Can and some subsequent analyses. TR-09-22, Svensk Kärnbränslehantering AB.

Statistica, 2009. Version: 9.0.231.4. Statsoft Inc. 2300 East 14:th st. Tulsa OK, 74104, USA http:\\www.statsoft.com

StereoStat, 2007. Version: 1.5. RockWare Inc. 2221 East St. #1. http:\\www.stereostat.com

Subversion, 2009. Version: 1.6.1. Tigris.org. http://subversion.tigris.org/.

Sundberg J, Back P-E, Ländell M, Sundberg A, 2009. Modelling of temperature in deep boreholes and evaluation of geothermal heat flow at Forsmark and Laxemar. SKB TR-09-14, Svensk Kärnbränslehantering AB.

TortoiseSVN, 2009. Version: 1.6.1, Build 16129. http://tortoisesvn.net.

Tukey J W, 1977. Exploratory data analysis, Addison-Wesley, Reading, MA, USA. Volume.

Walsh J J, Watterson J, 1989. Displacement gradients on fault surfaces. Journal of Structural Geology 11(3): pp 307–316.

Wang X 2005. Stereological interpretation of rock fracture traces on borehole walls and other cylindrical surfaces. PhD-Thesis, Virginia Polytechnic Institute and State University. Blacksburg, Virginia

Unpublished documents

SKBdoc id	Title	Issuer, year
1093682	On the collision test between a cylinder and a disc	SKB, 2008

Appendix 1

Number of canister positions at various distances from deformation zones classified according to rock- and fracture domain

Table A1-1. Number of canisters at various distances from deformation zones at Forsmark, classified according to fracture domain (a total of 8,126 canister positions).

Forsmark	rCrit=62.5/85 >5 km, 100–200 m	rCrit=125/170 >5 km, 200–400 m	rCrit=160/215 >5 km, 400–600 m	rCrit=225/>300 >5 km, >600 m	rCrit=75/100 3–5 km, 100–200 m	rCrit=150/200 3–5 km, 200–400 m	rCrit=235/>300 3–5 km, 400–600 m	rCrit=>300/>>300 3–5 km, >600 m
FFM01								
ZFMA2	–	–	–	–	349	1,759	2,288	2,239
ZFMNW0017	0	0	145	6,490	–	–	–	–
ZFMNW1200	–	–	–	–	89	423	836	5,287
ZFMWNW0123	189	729	901	4,816	–	–	–	–
ZFMWNW0809A	–	–	–	–	0	644	355	5,636
FFM06								
ZFMA2	–	–	–	–	0	0	514	977
ZFMNW0017	0	0	0	1,491	–	–	–	–
ZFMNW1200	–	–	–	–	0	0	0	1,491
ZFMWNW0123	0	0	0	1,491	–	–	–	–
ZFMWNW0809A	–	–	–	–	0	104	650	737

Table A1-2. Number of canisters at various distances from deformation zones at Laxemar, classified according to fracture domain (a total of 8,040 canister positions).

Laxemar	rCrit=62.5/85 >5 km, 100–200 m	rCrit=125/170 >5 km, 200–400 m	rCrit=160/215 >5 km, 400–600 m	rCrit=225/>300 >5 km, >600 m	rCrit=75/100 3–5 km, 100–200 m	rCrit=150/200 3–5 km, 200–400 m	rCrit=235/>300 3–5 km, 400–600 m	rCrit=>300/>>300 3–5 km, >600 m
FSM_C, RMSA01								
ZSMEW002A	0	0	0	98				
ZSMNS057A	0	0	0	98				
ZSMNW042A	0	0	0	98				
ZSMNE004A	0	0	0	98				
ZSMNW088A					0	0	0	98
ZSMNS059A					0	0	0	98
ZSMEW007A					0	0	22	76
FSM_C, RMSD01								
ZSMEW002A	0	0	0	1,000				
ZSMNS057A	0	0	0	1,000				
ZSMNW042A	117	428	406	49				
ZSMNE004A	0	0	0	1,000				
ZSMNW088A					0	0	0	1,000
ZSMNS059A					37	220	297	446
ZSMEW007A					0	0	0	1,000
FSM_C, RMSM01								
ZSMEW002A	0	0	0	1,103				
ZSMNS057A	0	0	0	1,103				
ZSMNW042A	0	0	49	1,054				
ZSMNE004A	0	0	0	1,103				
ZSMNW088A					0	0	0	1,103
ZSMNS059A					84	244	156	619
ZSMEW007A					0	0	162	941

Laxemar	rCrit=62.5/85 >5 km, 100–200 m	rCrit=125/170 >5 km, 200–400 m	rCrit=160/215 >5 km, 400–600 m	rCrit=225/>300 >5 km, >600 m	rCrit=75/100 3–5 km, 100–200 m	rCrit=150/200 3–5 km, 200–400 m	rCrit=235/>300 3–5 km, 400–600 m	rCrit=>300/>>300 3–5 km, >600 m
FSM_EW007, RMSA01								
ZSMEW002A	0	0	20	1,586				
ZSMNS057A	0	0	0	1,606				
ZSMNW042A	0	0	0	1,606				
ZSMNE004A	0	0	0	1,606				
ZSMNW088A					0	0	0	1,606
ZSMNS059A					0	21	74	1,511
ZSMEW007A					156	918	532	0
FSM_EW007, RMSM01								
ZSMEW002A	0	0	7	411				
ZSMNS057A	0	0	0	418				
ZSMNW042A	0	0	0	418				
ZSMNE004A	0	0	0	418				
ZSMNW088A					0	0	0	418
ZSMNS059A					14	164	151	89
ZSMEW007A					5	198	215	0
FSM_NE005, RMSA01								
ZSMEW002A	0	0	0	338				
ZSMNS057A	0	0	0	338				
ZSMNW042A	0	0	0	338				
ZSMNE004A	0	0	0	338				
ZSMNW088A					0	0	0	338
ZSMNS059A					0	0	0	338
ZSMEW007A					0	0	14	324
FSM_NE005, RMSD01								
ZSMEW002A	0	0	0	825				
ZSMNS057A	0	0	0	825				
ZSMNW042A	70	406	303	46				

Laxemar	rCrit=62.5/85 >5 km, 100–200 m	rCrit=125/170 >5 km, 200–400 m	rCrit=160/215 >5 km, 400–600 m	rCrit=225/>300 >5 km, >600 m	rCrit=75/100 3–5 km, 100–200 m	rCrit=150/200 3–5 km, 200–400 m	rCrit=235/>300 3–5 km, 400–600 m	rCrit=>300/>>300 3–5 km, >600 m
ZSMNE004A	0	0	290	535				
ZSMNW088A					0	0	2	823
ZSMNS059A					0	0	0	825
ZSMEW007A					0	0	0	825
FSM_NE005, RMSM01								
ZSMEW002A	0	0	0	348				
ZSMNS057A	0	0	0	348				
ZSMNW042A	0	0	0	348				
ZSMNE004A	0	0	7	341				
ZSMNW088A					0	0	0	348
ZSMNS059A					0	0	0	348
ZSMEW007A					0	0	0	348
FSM_W, RMSD01								
ZSMEW002A	0	4	102	1,631				
ZSMNS057A	0	0	5	1,732				
ZSMNW042A	95	331	273	1,038				
ZSMNE004A	0	0	0	1,737				
ZSMNW088A					0	0	0	1,737
ZSMNS059A					94	604	662	377
ZSMEW007A					0	0	68	1,669
FSM_W, RMSM01								
ZSMEW002A	16	256	175	120				
ZSMNS057A	0	0	53	514				
ZSMNW042A	0	0	0	567				
ZSMNE004A	0	0	0	567				
ZSMNW088A					0	0	0	567
ZSMNS059A					14	314	168	71
ZSMEW007A					12	189	336	30

Appendix 2

Number of critical positions for various DFN models and rock domains

Table A2-1. Number of critical canister positions at Forsmark, using DFN model "r_0-fixed".

Probabilistic	Valid N	Fraction	Minimum	Maximum	Std. Dev.	Ncrit				
r_0-fixed, FFM01						ZFMA2	ZFMNW0017	ZFMNW1200	ZFMWNW0123	ZFMWNW0809A
Fraction 62.5/85 m	50000	2.209E–04	0	0.6667	0.005303	0	0	0	4.175E–02	0
Fraction 75/100 m	50000	1.564E–04	0	0.6667	0.004569	0.054581	0	0.013918888	0	0
Fraction 125/170 m	50000	3.467E–05	0	0.4667	0.002373	0	0	0	0.025275888	0
Fraction 150/200 m	50000	1.183E–05	0	0.0857	0.000698	0.020816	0	0.005005782	0	0.007621096
Fraction 160/215 m	50000	6.520E–06	0	0.0638	0.000533	0	0.0009454	0	0.00587452	0
Fraction 225/300 m	50000	8.880E–07	0	0	0	0	0.00576312	0	0.004276608	0
Fraction 235/300 m	50000	0.000E+00	0	0	0	0	0	0	0	0
r_0-fixed, FFM06										
Fraction 62.5/85 m	50000	3.694E–04	0	0.6667	0.005303	0	0	0	0	0
Fraction 75/100 m	50000	2.557E–04	0	0.6667	0.004569	0	0	0	0	0
Fraction 125/170 m	50000	4.688E–05	0	0.4667	0.002373	0	0	0	0	0
Fraction 150/200 m	50000	1.415E–05	0	0.0857	0.000698	0	0	0	0	0.0014716
Fraction 160/215 m	50000	8.292E–06	0	0.0638	0.000533	0	0	0	0	0
Fraction 225/300 m	50000	0.000E+00	0	0	0	0	0	0	0	0
Fraction 235/300 m	50000	0.000E+00	0	0	0	0	0	0	0	0
					Sum, Rescaled to 6000	**0.0557**	**0.0050**	**0.0140**	**0.0570**	**0.0067**

Table A2-2. Number of critical canister positions at Forsmark, using DFN model "OSM+TFM".

Probabilistic	Valid N	Fraction	Minimum	Maximum	Std. Dev.	Ncrit				
OSM+TFM, FFM01						ZFMA2	ZFMNW0017	ZFMNW1200	ZFMWNW0123	ZFMWNW0809A
Fraction 62.5/85 m	50000	2.808E–04	0	0.6667	0.005303	0	0	0	0.05307309	0
Fraction 75/100 m	50000	1.747E–04	0	0.6667	0.004569	0.060982	0	0.015551326	0	0
Fraction 125/170 m	50000	4.296E–05	0	0.4667	0.002373	0	0	0	0.031319298	0
Fraction 150/200 m	50000	1.488E–05	0	0.0857	0.000698	0.02617	0	0.006293394	0	0.009581432
Fraction 160/215 m	50000	7.728E–06	0	0.0638	0.000533	0	0.00112056	0	0.006962928	0
Fraction 225/300 m	50000	0.000E+00	0	0	0	0	0	0	0	0
Fraction 235/300 m	50000	0.000E+00	0	0	0	0	0	0	0	0
OSM+TFM, FFM06										
Fraction 62.5/85 m	50000	3.576E–04	0	0.6667	0.005303	0	0	0	0	0
Fraction 75/100 m	50000	2.358E–04	0	0.6667	0.004569	0	0	0	0	0
Fraction 125/170 m	50000	5.393E–05	0	0.4667	0.002373	0	0	0	0	0
Fraction 150/200 m	50000	2.162E–05	0	0.0857	0.000698	0	0	0	0	0.002248688
Fraction 160/215 m	50000	1.561E–05	0	0.0638	0.000533	0	0	0	0	0
Fraction 225/300 m	50000	0.000E+00	0	0	0	0	0	0	0	0
Fraction 235/300 m	50000	0.000E+00	0	0	0	0	0	0	0	0
					Sum, Rescaled to 6000	**0.0644**	**0.0008**	**0.0161**	**0.0675**	**0.0087**

Table A2-3. Number of critical canister positions at Forsmark, using DFN model "TCM".

Probabilistic	Valid N	Fraction	Minimum	Maximum	Std. Dev.	Ncrit				
TCM, FFM01						ZFMA2	ZFMNW0017	ZFMNW1200	ZFMWNW0123	ZFMWNW0809A
Fraction 62.5/85 m	50000	5.577E–04	0	0.6667	0.005303	0	0	0	0.105412482	0
Fraction 75/100 m	50000	3.713E–04	0	0.6667	0.004569	0.129582	0	0.033045344	0	0
Fraction 125/170 m	50000	5.015E–05	0	0.4667	0.002373	0	0	0	0.036562266	0
Fraction 150/200 m	50000	1.949E–05	0	0.0857	0.000698	0.034279	0	0.008243424	0	0.012550272
Fraction 160/215 m	50000	1.208E–05	0	0.0638	0.000533	0	0.00175102	0	0.010880476	0
Fraction 225/300 m	50000	0.000E+00	0	0	0	0	0	0	0	0
Fraction 235/300 m	50000	0.000E+00	0	0	0	0	0	0	0	0
TCM, FFM06										
Fraction 62.5/85 m	50000	7.500E–04	0	0.6667	0.005303	0	0	0	0	0
Fraction 75/100 m	50000	4.686E–04	0	0.6667	0.004569	0	0	0	0	0
Fraction 125/170 m	50000	5.177E–05	0	0.4667	0.002373	0	0	0	0	0
Fraction 150/200 m	50000	2.322E–05	0	0.0857	0.000698	0	0	0	0	0.00241488
Fraction 160/215 m	50000	1.491E–05	0	0.0638	0.000533	0	0	0	0	0
Fraction 225/300 m	50000	1.428E–06	0	0	0	0	0.002129148	0	0.002129148	0
Fraction 235/300 m	50000	0.000E+00	0	0	0	0	0	0	0	0
					Sum, Rescaled to 6000	**0.1210**	**0.0029**	**0.0305**	**0.1144**	**0.0110**

Table A2-4. Number of critical canister positions at Laxemar, using DFN model "BMU".

Probabilistic	Valid N	Fraction	Minimum	Maximum	Std. Dev.	Ncrit						
						ZSMEW002A	ZSMEW007A	ZSMNE004A	ZSMNS057A	ZSMNS059A	ZSMNW042A	ZSMNW088A
FSM_C, RMSA01												
Fraction 62.5/85 m	35000	1.92E–04	0.00E+00	2.81E–01	5.10E–03	0	0	0	0	0	0	0
Fraction 75/100 m	35000	1.14E–04	0.00E+00	1.33E–01	3.22E–03	0	0	0	0	0	0	0
Fraction 125/170 m	35000	3.33E–05	0.00E+00	1.33E–01	1.94E–03	0	0	0	0	0	0	0
Fraction 150/200 m	35000	2.67E–05	0.00E+00	1.33E–01	1.89E–03	0	0	0	0	0	0	0
Fraction 160/215 m	35000	2.67E–05	0.00E+00	1.33E–01	1.89E–03	0	0	0	0	0	0	0
Fraction 225/300 m	35000	2.00E–05	0.00E+00	1.00E–01	1.41E–03	1.96E–03	0	1.96E–03	1.96E–03	0	1.96E–03	0
Fraction 235/300 m	35000	0.00E+00	0.00E+00	0.00E+00	0.00E+00	0	0	0	0	0	0	0
FSM_C, RMSD01												
Fraction 62.5/85 m	35000	1.77E–04	0.00E+00	1.18E–01	3.10E–03	0	0	0	0	0	2.07E–02	0
Fraction 75/100 m	35000	9.74E–05	0.00E+00	8.82E–02	2.16E–03	0	0	0	0	3.61E–03	0	0
Fraction 125/170 m	35000	2.35E–05	0.00E+00	5.41E–02	9.95E–04	0	0	0	0	0	1.01E–02	0
Fraction 150/200 m	35000	1.15E–05	0.00E+00	3.03E–02	5.74E–04	0	0	0	0	2.52E–03	0	0
Fraction 160/215 m	35000	6.06E–06	0.00E+00	3.03E–02	4.29E–04	0	0	0	0	0	2.46E–03	0
Fraction 225/300 m	35000	0.00E+00	0.00E+00	0.00E+00	0.00E+00	0	0	0	0	0	0	0
Fraction 235/300 m	35000	0.00E+00	0.00E+00	0.00E+00	0.00E+00	0	0	0	0	0	0	0
FSM_C, RMSM01												
Fraction 62.5/85 m	35000	3.18E–04	0.00E+00	4.00E–01	6.93E–03	0	0	0	0	0	0	0
Fraction 75/100 m	35000	1.47E–04	0.00E+00	2.67E–01	4.51E–03	0	0	0	0	1.24E–02	0	0
Fraction 125/170 m	35000	1.74E–05	0.00E+00	8.70E–02	1.23E–03	0	0	0	0	0	0	0
Fraction 150/200 m	35000	0.00E+00	0.00E+00	0.00E+00	0.00E+00	0	0	0	0	0	0	0
Fraction 160/215 m	35000	0.00E+00	0.00E+00	0.00E+00	0.00E+00	0	0	0	0	0	0	0
Fraction 225/300 m	35000	0.00E+00	0.00E+00	0.00E+00	0.00E+00	0	0	0	0	0	0	0
Fraction 235/300 m	35000	0.00E+00	0.00E+00	0.00E+00	0.00E+00	0	0	0	0	0	0	0
FSM_EW007, RMSA01												
Fraction 62.5/85 m	35000	2.26E–04	0.00E+00	2.38E–01	4.78E–03	0	0	0	0	0	0	0
Fraction 75/100 m	35000	1.60E–04	0.00E+00	2.38E–01	4.20E–03	0	2.49E–02	0	0	0	0	0
Fraction 125/170 m	35000	2.08E–05	0.00E+00	3.70E–02	8.48E–04	0	0	0	0	0	0	0
Fraction 150/200 m	35000	0.00E+00	0.00E+00	0.00E+00	0.00E+00	0	0	0	0	0	0	0
Fraction 160/215 m	35000	0.00E+00	0.00E+00	0.00E+00	0.00E+00	0	0	0	0	0	0	0
Fraction 225/300 m	35000	0.00E+00	0.00E+00	0.00E+00	0.00E+00	0	0	0	0	0	0	0
Fraction 235/300 m	35000	0.00E+00	0.00E+00	0.00E+00	0.00E+00	0	0	0	0	0	0	0
FSM_EW007, RMSM01												
Fraction 62.5/85 m	35000	2.70E–04	0.00E+00	5.00E–01	8.05E–03	0	0	0	0	0	0	0
Fraction 75/100 m	35000	1.79E–04	0.00E+00	3.50E–01	5.90E–03	0	8.97E–04	0	0	2.51E–03	0	0
Fraction 125/170 m	35000	1.58E–05	0.00E+00	4.35E–02	7.96E–04	0	0	0	0	0	0	0
Fraction 150/200 m	35000	0.00E+00	0.00E+00	0.00E+00	0.00E+00	0	0	0	0	0	0	0

Fraction 160/215 m	35000	0.00E+00	0.00E+00	0.00E+00	0.00E+00	0	0	0	0	0	0	0
Fraction 225/300 m	35000	0.00E+00	0.00E+00	0.00E+00	0.00E+00	0	0	0	0	0	0	0
Fraction 235/300 m	35000	0.00E+00	0.00E+00	0.00E+00	0.00E+00	0	0	0	0	0	0	0
FSM_NE005, RMSA01												
Fraction 62.5/85 m	35000	2.76E–04	0.00E+00	2.61E–01	6.33E–03	0	0	0	0	0	0	0
Fraction 75/100 m	35000	1.33E–04	0.00E+00	2.33E–01	4.30E–03	0	0	0	0	0	0	0
Fraction 125/170 m	35000	6.05E–05	0.00E+00	2.33E–01	3.44E–03	0	0	0	0	0	0	0
Fraction 150/200 m	35000	6.05E–05	0.00E+00	2.33E–01	3.44E–03	0	0	0	0	0	0	0
Fraction 160/215 m	35000	4.02E–05	0.00E+00	1.67E–01	2.41E–03	0	0	0	0	0	0	0
Fraction 225/300 m	35000	0.00E+00	0.00E+00	0.00E+00	0.00E+00	0	0	0	0	0	0	0
Fraction 235/300 m	35000	0.00E+00	0.00E+00	0.00E+00	0.00E+00	0	0	0	0	0	0	0
FSM_NE005, RMSD01												
Fraction 62.5/85 m	35000	1.54E–04	0.00E+00	9.68E–02	3.16E–03	0	0	0	0	0	1.08E–02	0
Fraction 75/100 m	35000	8.95E–05	0.00E+00	9.68E–02	2.44E–03	0	0	0	0	0	0	0
Fraction 125/170 m	35000	3.01E–05	0.00E+00	6.25E–02	1.27E–03	0	0	0	0	0	1.22E–02	0
Fraction 150/200 m	35000	1.11E–05	0.00E+00	5.56E–02	7.86E–04	0	0	0	0	0	0	0
Fraction 160/215 m	35000	1.11E–05	0.00E+00	5.56E–02	7.86E–04	0	0	3.22E–03	0	0	3.37E–03	0
Fraction 225/300 m	35000	0.00E+00	0.00E+00	0.00E+00	0.00E+00	0	0	0	0	0	0	0
Fraction 235/300 m	35000	0.00E+00	0.00E+00	0.00E+00	0.00E+00	0	0	0	0	0	0	0
FSM_NE005, RMSM01												
Fraction 62.5/85 m	35000	3.61E–04	0.00E+00	1.54E–01	5.99E–03	0	0	0	0	0	0	0
Fraction 75/100 m	35000	1.86E–04	0.00E+00	1.54E–01	3.99E–03	0	0	0	0	0	0	0
Fraction 125/170 m	35000	3.91E–05	0.00E+00	1.15E–01	1.82E–03	0	0	0	0	0	0	0
Fraction 150/200 m	35000	3.14E–05	0.00E+00	7.69E–02	1.35E–03	0	0	0	0	0	0	0
Fraction 160/215 m	35000	8.00E–06	0.00E+00	4.00E–02	5.66E–04	0	0	5.60E–05	0	0	0	0
Fraction 225/300 m	35000	0.00E+00	0.00E+00	0.00E+00	0.00E+00	0	0	0	0	0	0	0
Fraction 235/300 m	35000	0.00E+00	0.00E+00	0.00E+00	0.00E+00	0	0	0	0	0	0	0
FSM_W, RMSD01												
Fraction 62.5/85 m	35000	1.47E–04	0.00E+00	1.47E–01	3.51E–03	0	0	0	0	0	1.40E–02	0
Fraction 75/100 m	35000	7.89E–05	0.00E+00	9.68E–02	2.40E–03	0	0	0	0	7.42E–03	0	0
Fraction 125/170 m	35000	0.00E+00	0.00E+00	0.00E+00	0.00E+00	0	0	0	0	0	0	0
Fraction 150/200 m	35000	0.00E+00	0.00E+00	0.00E+00	0.00E+00	0	0	0	0	0	0	0
Fraction 160/215 m	35000	0.00E+00	0.00E+00	0.00E+00	0.00E+00	0	0	0	0	0	0	0
Fraction 225/300 m	35000	0.00E+00	0.00E+00	0.00E+00	0.00E+00	0	0	0	0	0	0	0
Fraction 235/300 m	35000	0.00E+00	0.00E+00	0.00E+00	0.00E+00	0	0	0	0	0	0	0
FSM_W, RMSM01												
Fraction 62.5/85 m	35000	2.35E–04	0.00E+00	1.85E–01	4.43E–03	3.76E–03	0	0	0	0	0	0
Fraction 75/100 m	35000	1.33E–04	0.00E+00	1.48E–01	3.33E–03	0	1.60E–03	0	0	1.87E–03	0	0
Fraction 125/170 m	35000	3.06E–05	0.00E+00	7.41E–02	1.31E–03	7.82E–03	0	0	0	0	0	0
Fraction 150/200 m	35000	8.33E–06	0.00E+00	4.17E–02	5.89E–04	0	1.58E–03	0	0	2.62E–03	0	0
Fraction 160/215 m	35000	8.33E–06	0.00E+00	4.17E–02	5.89E–04	1.46E–03	0	0	4.42E–04	0	0	0
Fraction 225/300 m	35000	0.00E+00	0.00E+00	0.00E+00	0.00E+00	0	0	0	0	0	0	0
Fraction 235/300 m	35000	0.00E+00	0.00E+00	0.00E+00	0.00E+00	0	0	0	0	0	0	0
				Sum, Rescaled to 6000		**1.12E–02**	**2.16E–02**	**3.91E–03**	**1.79E–03**	**2.46E–02**	**5.64E–02**	**0**

Appendix 3

DFN models

In this appendix, we replicate the DFN models from the model database /Modelldatabasen 2007, 2008/ for the readers convenience. Note, however, that the models can be subject to revisions and should always be downloaded from the model database rather than being replicated from the tables below unless, of course, the intention is to replicate the results herein.

A3.1. Forsmark DFN models

Fracture Domain FFM01, r_0-fixed Alternative

Set	Type	Trend	Plunge	Kappa	r_0 (m)	k_r	Global P_{32}	rmax (m)
NE	Global	314.90	1.30	20.94	0.039	2.718	1.733	564.200
NS	Global	270.10	5.30	21.34	0.039	2.745	1.292	564.200
NW	Global	230.10	4.60	15.70	0.039	2.607	0.948	564.200
SH	Global	0.80	87.30	17.42	0.039	2.579	0.624	564.200
ENE	Local	157.50	3.10	34.11	0.039	2.972	0.256	564.200
EW	Local	0.40	11.90	13.89	0.039	2.930	0.169	564.200
NNE	Local	293.80	0.00	21.79	0.039	3.000	0.658	564.200
SH2	Local	164.00	52.60	35.43	0.039	2.610	0.081	564.200
SH3	Local	337.90	52.90	17.08	0.039	2.610	0.067	564.200

Fracture Domain FFM01, TCM Alternative ('kr-fixed')

Set	Type	Trend	Plunge	Kappa	r_0 (m)	k_r	Global P_{32}	rmax (m)
NE	Global	314.9	1.3	20.943	0.659171	3.02	1.733229012	564.2
NS	Global	270.1	5.3	21.33938	0.059256	2.78	1.292080834	564.2
NW	Global	230.1	4.6	15.70056	0.59368	2.85	0.947802313	564.2
SH	Global	0.8	87.3	17.4185	0.816285	2.85	0.623883816	564.2
ENE	Local	157.5	3.1	34.11	0.32488	3.25	0.256333102	564.2
EW	Local	0.4	11.9	13.89333	0.17	3.1	0.168594082	564.2
NNE	Local	293.8	0	21.79	0.0385	3	0.658245158	564.2
SH2	Local	164	52.6	35.43	0.0385	2.61	0.08168411	564.2
SH3	Local	337.9	52.9	17.075	0.0385	2.61	0.066908499	564.2

Fracture Domain FFM01, OSM + TFM Alternative

Component	Set	Type	Trend	Plunge	Kappa	r_0 (m)	k_r	Global P_{32}	rmax (m)
OSM	NE	Global	314.9	1.3	20.943	0.0385	2.64	1.709425143	28
OSM	NS	Global	270.1	5.3	21.33938	0.0385	2.9	1.289614635	28
OSM	NW	Global	230.1	4.6	15.70056	0.0385	2.44	0.898302275	28
OSM	SH	Global	0.8	87.3	17.4185	0.0385	2.61	0.615018629	28
OSM	ENE	Local	157.5	3.1	34.11	0.0385	2.2	0.187727553	28
OSM	EW	Local	0.4	11.9	13.89333	0.0385	3.06	0.168460531	28
OSM	NNE	Local	293.8	0	21.79	0.0385	3	0.657340071	28
OSM	SH2	Local	164	52.6	35.43	0.0385	2.61	0.080216867	28
OSM	SH3	Local	337.9	52.6	17.075	0.0385	2.61	0.065706661	28
TFM	NE	Global	315.3	1.8	27.02333	28	3	0.028510638	564.2
TFM	NS	Global	92.7	1.2	30.685	28	2.2	0.000338626	564.2
TFM	NW	Global	47.6	4.4	19.672	28	2.06	0.000255553	564.2
TFM	SH	Global	347.4	85.6	23.24625	28	2.83	0.028611802	564.2
TFM	ENE	Global	157.9	4	53.18143	28	3.14	0.08706543	564.2
TFM	EW	Global	186.3	4.3	34.2325	28	2.85	0.001383161	564.2

Fracture Domain FFM06, r_0-fixed Alternative

Set	Type	Trend	Plunge	Kappa	r_0 (m)	k_r	Global P_{32}	rmax (m)
NE	Global	125.70	10.10	45.05	0.039	2.785	3.299	564.200
NS	Global	91.00	4.10	19.49	0.039	2.780	2.150	564.200
NW	Global	34.10	0.80	16.13	0.039	2.662	1.608	564.200
SH	Global	84.30	71.30	10.78	0.039	2.582	0.640	564.200
ENE	Local	155.40	8.30	20.83	0.039	2.865	0.194	564.200
SH2	Local	0.00	47.50	12.71	0.039	2.610	0.429	564.200

Fracture Domain FFM06, TCM Alternative ('kr-fixed')

Set	Type	Trend	Plunge	Kappa	r_0 (m)	k_r	Global P_{32}	rmax (m)
NE	Global	125.7	10.1	45.05	0.350908	3.02	3.298729012	564.2
NS	Global	91	4.1	19.48667	0.0385	2.78	2.150388557	564.2
NW	Global	34.1	0.8	16.13	0.319266	2.85	1.607802313	564.2
SH	Global	84.3	71.3	10.77667	0.792852	2.85	0.639583816	564.2
ENE	Local	155.4	8.3	20.83	0.74	3.25	0.194005885	564.2
SH2	Local	0	47.5	12.71	0.0385	2.61	0.429411556	564.2

Fracture Domain FFM06, OSM + TFM Alternative

Component	Set	Type	Trend	Plunge	Kappa	r_0 (m)	k_r	Global P_{32}	rmax (m)
OSM	NE	Global	125.7	10.1	45.05	0.0385	2.64	3.251854064	28
OSM	NS	Global	91	4.1	19.48667	0.0385	2.9	2.145881617	28
OSM	NW	Global	34.1	0.8	16.13	0.0385	2.44	1.52189537	28
OSM	SH	Global	84.3	71.3	10.77667	0.0385	2.61	0.630457605	28
OSM	ENE	Local	155.4	8.3	20.83	0.0385	2.2	0.142109985	28
OSM	SH2	Local	0	47.5	12.71	0.0385	2.61	0.422914502	28
TFM	NE	Global	315.3	1.8	27.02333	28	3	0.028510638	564.2
TFM	NS	Global	92.7	1.2	30.685	28	2.2	0.000338626	564.2
TFM	NW	Global	47.6	4.4	19.672	28	2.06	0.000255553	564.2
TFM	SH	Global	347.4	85.6	23.24625	28	2.83	0.028611802	564.2
TFM	ENE	Global	157.9	4	53.18143	28	3.14	0.08706543	564.2
TFM	EW	Global	186.3	4.3	34.2325	28	2.85	0.001383161	564.2

A3.2. Laxemar DFN models

FSM_C_euclidian_BMU

Set ID	Trend	Plunge	Kappa	r_0 (m)	k_r	Global P_{32}	rmax (m)
SH	354.11	82.67	7.59	0.33	3.31	2.66	564.19
ENE	344.27	1.98	10.20	0.37	3.00	1.72	564.19
WNW	21.31	4.27	8.24	0.08	2.80	2.53	564.19
N-S	270.76	0.70	8.33	0.59	3.26	2.33	564.19

FSM_W_euclidian_BMU

Set ID	Trend	Plunge	Kappa	r_0 (m)	k_r	Global P_{32}	rmax (m)
SH	295.8400	84.7900	7.2200	0.2773	3.3100	3.3980	564.1896
ENE	157.0200	0.8700	10.2300	0.4009	3.0000	1.6029	564.1896
WNW	205.6000	1.6000	6.6400	0.1132	2.8000	1.9667	564.1896
N-S	269.7700	5.4100	7.9000	0.4160	3.2600	3.5962	564.1896

FSM_NE005_euclidian_BMU

Set ID	Trend	Plunge	Kappa	r_0 (m)	k_r	Global P_{32}	rmax (m)
SH	61.9100	81.1300	6.6000	0.2928	3.3100	3.1651	564.1896
ENE	337.7100	0.6400	8.5900	0.4017	3.0000	1.5996	564.1896
WNW	29.1400	7.5800	6.4700	0.0898	2.8000	2.3678	564.1896
N-S	88.5400	2.4000	8.1000	0.3609	3.2600	4.3012	564.1896

FSM_N_euclidian_BMU

Set ID	Trend	Plunge	Kappa	r_0 (m)	k_r	Global P_{32}	rmax (m)
SH	268.3100	82.5900	9.9500	0.2194	3.3100	4.6198	564.1896
ENE	341.9900	5.9500	11.5500	0.4649	3.0000	1.3818	564.1896
WNW	24.2200	2.8600	7.9900	0.0772	2.8000	2.6730	564.1896
N-S	266.6200	5.0200	6.8900	0.5328	3.2600	2.6331	564.1896

FSM_EW007_euclidian_BMU

Set ID	Trend	Plunge	Kappa	r_0 (m)	k_r	Global P_{32}	rmax (m)
SH	86.7100	85.9500	7.0500	0.2270	3.3100	4.4165	564.1896
ENE	163.3400	1.5300	9.3800	0.3243	3.0000	1.9819	564.1896
WNW	23.2800	3.2900	8.4000	0.0698	2.8000	2.8954	564.1896
N-S	87.7500	2.2500	6.2500	0.4854	3.2600	2.9613	564.1896

FSM_S_euclidian_BMU

Set ID	Trend	Plunge	Kappa	r_0 (m)	k_r	Global P_{32}	rmax (m)
SH	282.6900	82.4100	5.8000	0.2349	3.3100	4.2232	564.1896
ENE	335.7900	1.2800	9.5000	0.1500	3.0000	4.2841	564.1896
WNW	27.4700	5.9200	5.5200	0.0322	2.8000	5.3876	564.1896
N-S	266.7400	4.2000	6.6000	0.2741	3.2600	6.0857	564.1896